Fiber Tracking and Fiber Tract Segmentation Using Diffusion Tensor Imaging

by

Chuyang Ye

A dissertation submitted to The Johns Hopkins University in conformity with the requirements for the degree of Doctor of Philosophy.

Baltimore, Maryland

December, 2014

Abstract

Diffusion tensor imaging (DTI) has become a popular tool for noninvasively investigating fiber tract structures. Fiber tracking and tract segmentation are two major tasks in DTI studies. However, fiber crossing is a well known issue in DTI because DTI cannot model crossing fiber orientations (FOs). Therefore, fiber tracking and tract segmentation methods that are able to address crossing fibers are needed. In this thesis, three contributions are made to the development of such fiber tracking and tract segmentation algorithms. First, a fiber tracking method guided by volumetric tract segmentation is presented. Tract segmentation contains anatomical information which can reduce the errors caused by crossing fibers and noise. The FO estimation problem is formulated in a Bayesian framework and the resulting objective function is solved with calculus of variations. The proposed method is able to reduce false positive fibers and generate fibers that correspond to known anatomy. It is also applied to a brain connectome study to show its potential scientific application. Second, we present an algorithm for resolving crossing fibers in situations where limited diffusion gradient directions are achievable. In particular, the algorithm is focused on interdig-

itated tongue muscles. It incorporates prior knowledge on likely FOs to account for the insufficient information due to limited diffusion gradient directions. Using maximum a posteriori estimation, FOs can be estimated by solving a weighted ℓ_1-norm regularized least squares minimization. The method is shown to reduce the effect of noise and resolve crossing fibers with limited DTI. The distributions of the computed FOs in both the controls and the patients were also compared, suggesting a potential clinical use for this methodology. Third, a white matter tract segmentation method is proposed. The method focuses on the cerebellar peduncles, which are major white matter tracts in the cerebellum. The method uses volumetric segmentation concepts based on extracted DTI features. The crossing and noncrossing portions of the peduncles are modeled as separate objects. They are initially classified using a random forest classifier together with the DTI features, and then refined by a multi-object geometric deformable model. The method is shown to achieve better segmentation results than two atlas-based methods. In the study on spinocerebellar ataxia type 6 (SCA6), the proposed method is shown to reveal anatomical changes in the patients, which demonstrates the benefit of the method for scientific purposes.

Primary Reader: Jerry L. Prince

Secondary Reader: Trac D. Tran

Third Reader: John Goutsias

Acknowledgments

I would like to first express my gratitude to my advisor Dr. Jerry L. Prince for his support and guidance during my graduate study. I have learned so many things from Dr. Prince, especially on how research should be conducted. His advice on my research has been priceless.

I would like to thank Dr. Pierre-Louis Bazin, who helped me start my research in the field of diffusion MRI. I would also like to thank Dr. Sarah Ying, Dr. Maureen Stone, and Dr. Emi Murano. They are knowledgeable in the anatomy and have provided valuable feedbacks and suggestions.

I would like to thank Dr. Trac D. Tran and Dr. John Goutsias for reading my thesis. And I am also grateful that I have learned signal and image processing fundamentals from your inspiring courses.

I am lucky to have so many brilliant lab members in IACL. Their researches are exciting and have broaden my horizons. I have also received all kinds of help from these kind colleagues. Without them, my PhD study could have taken a much longer time.

ACKNOWLEDGMENTS

Finally, I must thank my friends and family for their help during my PhD study. There were difficult times, but their love and support helped me get through these difficulties.

Contents

CONTENTS

List of Tables

List of Figures

Chapter 1

Introduction

Diffusion tensor imaging (DTI) has become a popular tool for noninvasively investigating the fiber structures of white matter tracts and muscles by imaging the diffusion anisotropy in fibers [1, 2]. It provides contrast that is not available in conventional structural magnetic resonance imaging (MRI) such as T1-weighted and T2-weighted MRI, and is thus a unique imaging modality for scientific studies.

DTI models diffusion by a symmetric 3×3 diffusion tensor at each voxel. By acquiring a set of diffusion weighted images (DWIs) with noncollinear diffusion gradient directions, the diffusion tensor can be calculated. The diffusion tensor has six degrees of freedom. Thus, at least six noncollinear gradient directions are required for tensor estimation.

Using the diffusion information encoded in DTI, fibers can be reconstructed as 3D streamlines (see Figure 1.1(a)). This process is called *fiber tracking* or *tractogra-*

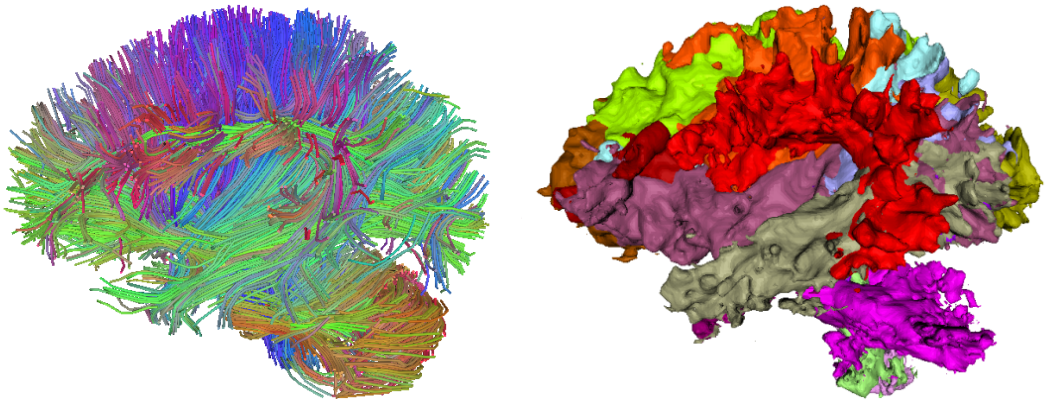

(a) 3D streamlines representing fibers (b) Segmented fiber tracts

Figure 1.1: Fiber tracking and tract segmentation: (a) 3D streamlines representing fibers and (b) segmented fiber tracts.

phy [3, 4]. These fiber streamlines provide a representation of fibers and reveal their anatomical structure. Fiber tracking can be applied to study human brain connectome [5–7] or diseases [8–10], and it is an important tool for analyzing DTI. Therefore, one of the major tasks in DTI is the development of fiber tracking algorithms that reconstruct fibers with high quality. A common strategy of fiber tracking is to start a streamline from a seeding voxel and propagate the streamline using the fiber orientations (FOs) calculated with diffusion information [3, 4]. For example, a basic FO estimate is to use the primary eigenvector (PEV) of the diffusion tensor. With some termination criteria, the end of the streamline is also determined.

Another popular research topic in DTI is the segmentation of fiber tracts that correspond to anatomy (see Figure 1.1(b)). Segmented tracts can be used to study specific diseases, where anatomical changes associated with these diseases can be evaluated [11–13]. The tract segmentation can be achieved by clustering the reconstructed

fibers, which is usually based on the similarities between fibers [14]. An alternative approach to segmenting fiber tracts is *volumetric tract segmentation*, where voxels are labeled using diffusion features [15–19]. Volumetric tract segmentation does not require a fiber tracking step, which avoids the variability caused by the choice of fiber tracking methods. In volumetric tract segmentation, very similar to conventional image segmentation problems using structural MRI, homogeneous regions can be identified using the image features [16, 20]. Classical segmentation frameworks, such as Markov random field (MRF) [21] and level-set methods [22], have been used for the purpose of tract segmentation.

In DTI, a major issue is the error caused by crossing fibers, because the DTI model cannot represent crossing FOs [23]. Therefore, this issue must be considered in fiber tracking and fiber tract segmentation. For example, in both fiber tracking and tract segmentation, the FOs cannot be extracted from the diffusion tensor [23]. In addition, for tract segmentation crossing regions have unique properties compared to noncrossing regions [15, 18]. Therefore, fiber tracking and tract segmentation algorithms that are able to cope with crossing fibers are needed and proposed. For example, in fiber tracking, previous works have used the aid of anatomical information to reduce tracking errors [24, 25]; fiber tracking methods based on multi-tensor models have also been developed to resolve crossing fibers [26, 27]. To solve the problem of segmenting crossing tracts, researchers have attempted to explicitly model the crossing regions and combine the noncrossing and crossing regions as the final

result [15].

However, there remain challenges in fiber tracking and tract segmentation. 1) Although anatomical information has been incorporated to reduce false fiber streamlines, the incorporation of anatomical knowledge has been mostly based on initial fiber tracking, which can bias the result and is not truly "anatomical" in the sense that the information is not from an anatomical atlas [24]. 2) Although methods that model crossing FOs, such as multi-tensor models, have been proposed, they require a sufficient number of diffusion gradient directions (around 30) [27]. But in situations where such a number is not achievable, successful resolution of crossing fibers is very challenging. For example, the *in vivo* tongue DTI acquisition takes only 2–3 minutes (around 12 gradient directions) due to involuntary swallowing, and there is insufficient information for multi-tensor models to resolve crossing tongue muscle fibers [28]. 3) In tract segmentation, although crossing regions can be modeled and segmented as separate objects, the localization of some crossing regions can be difficult due to their small sizes. This can lead to poor initialization, which affects the segmentation quality [18].

This dissertation focuses on the design of fiber tracking and tract segmentation algorithms that address the challenges introduced above. The contributions in this thesis are summarized as follows:

- **A fiber tracking method guided by volumetric tract segmentation**: We propose a Bayesian method for estimating FOs from DTI data, where anatomi-

cal tract information is incorporated to avoid tracking errors caused by crossing fibers and image noise. A first step segments and labels the white matter tracts volumetrically, including explicit representations of the crossing regions. A second step estimates the FOs using the diffusion information and the anatomical knowledge from segmented white matter tracts. A single FO is estimated in the noncrossing regions while two FOs are estimated in the crossing regions. A third step carries out streamlining tractography that uses information from both the segmented tracts and the estimated FOs. Experiments performed on a digital crossing phantom, a physical phantom, and brain DTI of 18 healthy subjects show that the proposed method is able to use the anatomical information to produce FOs with better accuracy and to reduce anatomically incorrect fiber streamlines. Results on tract connectivity to cortical areas also demonstrate the potential application of the proposed method to scientific studies.

- **Distinguishing interdigitated tongue muscles with limited DTI**: We address the challenge of distinguishing interdigitated tongue muscles from limited DTI by using a multi-tensor model with a fixed tensor basis and incorporating prior directional knowledge. The prior directional knowledge provides information on likely FOs at each voxel, and is computed with anatomical knowledge of tongue muscles. The FOs are estimated within a maximum a posteriori (MAP) framework, and the resulting objective function is solved using a noise-aware weighted ℓ_1-norm minimization algorithm. Experiments were performed on a

digital crossing phantom and *in vivo* tongue diffusion data including three control subjects and three patients with glossectomies. On the digital phantom, effects of parameters, noise, and prior direction accuracy were studied, and parameter settings for real data were determined. The results on the *in vivo* data demonstrate that the proposed method is able to resolve interdigitated tongue muscles with limited gradient directions. The distributions of the computed FOs in both the controls and the patients were also compared, suggesting a potential clinical use for this imaging and image analysis methodology.

- **Volumetric segmentation of the cerebellar peduncles**: An automatic method for segmenting white matter tracts is proposed. In particular, we focus on the structure of the cerebellar peduncles, which are major white matter tracts in the cerebellum, and of which the crossing regions are small. The method uses volumetric segmentation concepts based on extracted DTI features. The crossing and noncrossing portions of the peduncles are modeled as separate objects, and are initially classified using a random forest classifier (RFC) together with the DTI features. To obtain geometrically correct results, a multi-object geometric deformable model (MGDM) is used to refine the random forest classification result. The method was evaluated using a leave-one-out cross-validation on five control subjects and four patients with spinocerebellar ataxia type 6 (SCA6). It was then used to evaluate group differences in the peduncles in a population of 32 controls and 11 SCA6 patients, where anatomical changes with

respect to SCA6 were observed.

Parts of the thesis have been published previously. The fiber tracking method guided by volumetric tract segmentation was partly described in [29]. The algorithm of distinguishing interdigitated tongue muscles was presented in a preliminary form in [28]. A preliminary version of the cerebellar peduncle segmentation algorithm was described in [18].

The remainder of the thesis is organized as follows. Chapter 2 introduces background knowledge on DTI, fiber tracking, and tract segmentation, and gives examples of fiber tracts. Chapter 3 provides the FO estimation and fiber tracking algorithm with the guidance of volumetric tract segmentation. In Chapter 4, the method of distinguishing interdigitated tongue muscles with limited DTI is presented. Chapter 5 describes the proposed method for segmenting the cerebellar peduncles with the RFC and MGDM using the DTI features. Chapter 6 summarizes the thesis and discusses the future research directions.

Chapter 2

Background

In this chapter, an overview of diffusion tensor imaging (DTI) is provided and anatomical knowledge of selected fiber tracts is introduced. First, basic DTI principles are reviewed. Then, fiber tracking and tract segmentation based on DTI are described. Finally, the anatomical knowledge of tracts is introduced by the examples of the cerebellar peduncles and tongue muscles.

2.1 DTI Overview

DTI provides a noninvasive tool for the reconstruction of fiber tracts by capturing the anisotropy of water diffusion in tissue [1, 2]. Water diffusion is modeled by a diffusion tensor at each voxel. The diffusion tensor is a 3×3 symmetric positive

definite matrix:

$$\mathbf{D} = \begin{pmatrix} D_{xx} & D_{xy} & D_{xz} \\ D_{xy} & D_{yy} & D_{yz} \\ D_{xz} & D_{yz} & D_{zz} \end{pmatrix}, \tag{2.1}$$

which has six independent components. It can be estimated from diffusion weighted images (DWIs) acquired with at least six noncollinear gradient directions. Assuming water diffusion follows a Gaussian distribution, the relationship between the diffusion weighted signal and the diffusion tensor can be modeled as [30]

$$S_k = S_0 e^{-b\boldsymbol{g}_k^T \mathbf{D} \boldsymbol{g}_k} + n_k. \tag{2.2}$$

Here, S_k is the diffusion signal in the k-th gradient direction, S_0 is the baseline signal without diffusion weighting, b is a constant called b-value, which is determined by the imaging sequence, $\boldsymbol{g}_k = (g_{k,1}, g_{k,2}, g_{k,3})^T$ is the k-th gradient direction, and n_k is a noise term. In practice, usually around 30 gradient directions are used to increase the signal-to-noise ratio (SNR) [31].

To calculate the diffusion tensor, one can divide S_0 and then take the logarithm on both sides of Eq. (2.2), which leads to a linear regression model

$$\boldsymbol{y} = \mathbf{B}\boldsymbol{d} + \boldsymbol{\epsilon}, \tag{2.3}$$

where

$$\mathbf{B} = \begin{pmatrix} -bg_{1,1}^2 & -bg_{1,2}^2 & -bg_{1,3}^2 & -2bg_{1,1}g_{1,2} & -2bg_{1,1}g_{1,3} & -2bg_{1,2}g_{1,3} \\ -bg_{2,1}^2 & -bg_{2,2}^2 & -bg_{2,3}^2 & -2bg_{2,1}g_{2,2} & -2bg_{2,1}g_{2,3} & -2bg_{2,2}g_{2,3} \\ \vdots & \vdots & \vdots & \vdots & \vdots & \vdots \\ -bg_{K,1}^2 & -bg_{K,2}^2 & -bg_{K,3}^2 & -2bg_{K,1}g_{K,2} & -2bg_{K,1}g_{K,3} & -2bg_{K,2}g_{K,3} \end{pmatrix}, \quad (2.4)$$

$$\boldsymbol{y} = \begin{pmatrix} ln\left(\frac{S_1}{S_0}\right) & ln\left(\frac{S_2}{S_0}\right) & \dots & ln\left(\frac{S_K}{S_0}\right) \end{pmatrix}^T, \quad (2.5)$$

$$\boldsymbol{d} = \begin{pmatrix} D_{xx} & D_{yy} & D_{zz} & D_{xy} & D_{xz} & D_{yz} \end{pmatrix}^T. \quad (2.6)$$

Here $\boldsymbol{\epsilon}$ represents noise and K is the total number of gradient directions. Using a linear least squares fitting, an estimate of the tensor can be obtained as

$$\hat{\boldsymbol{d}} = (\mathbf{B}^T\mathbf{B})^{-1}\mathbf{B}^T\boldsymbol{y}. \quad (2.7)$$

Some variations have also been proposed for improving the tensor estimation, such as weighted linear least squares fitting and nonlinear least squares fitting [32, 33].

From the diffusion tensor, rotation-invariant scalar quantities can be calculated to describe the diffusion properties. For example, mean diffusivity (MD) and fractional anisotropy (FA) can computed from the eigenvalues ($\lambda_1 \geq \lambda_2 \geq \lambda_3 \geq 0$) of the

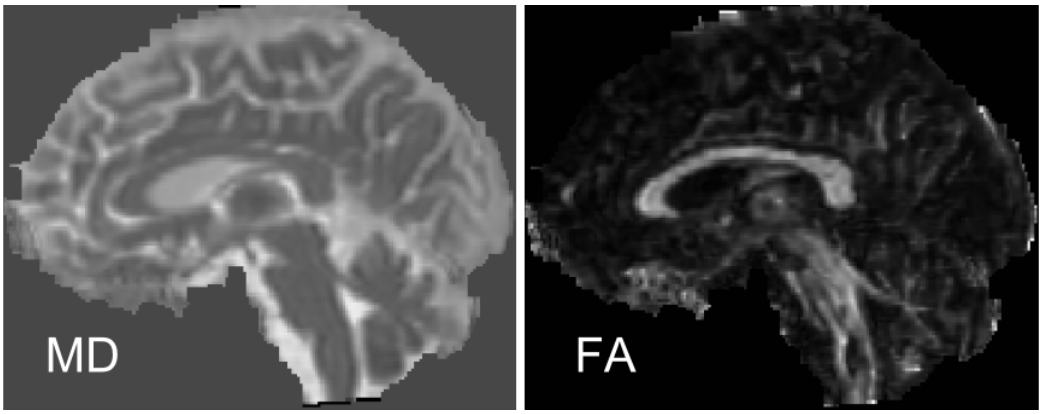

Figure 2.1: An example of MD and FA maps.

tensor [34]:

$$MD = \bar{\lambda} = \frac{\lambda_1 + \lambda_2 + \lambda_3}{3} \tag{2.8}$$

$$FA = \sqrt{\frac{3}{2}} \frac{\sqrt{(\lambda_1 - \bar{\lambda})^2 + (\lambda_2 - \bar{\lambda})^2 + (\lambda_3 - \bar{\lambda})^2}}{\sqrt{\lambda_1^2 + \lambda_2^2 + \lambda_3^2}}. \tag{2.9}$$

An example of MD and FA maps is shown in Figure 2.1. MD measures the amount of water diffusion [35]. FA measures the degree of anisotropy and has been used to reflect fiber tract integrity [36].

Directional information can also be obtained from the tensor. For example, in fiber tracts where only one dominant fiber orientation (FO) is available, the primary eigenvector (PEV) provides an estimate of the FO [3]. The FO can be visualized using a color map, where the intensity is coded by FA and the x, y, and z components of the PEV are assigned to the red, green, and blue channels, respectively [37]. An example

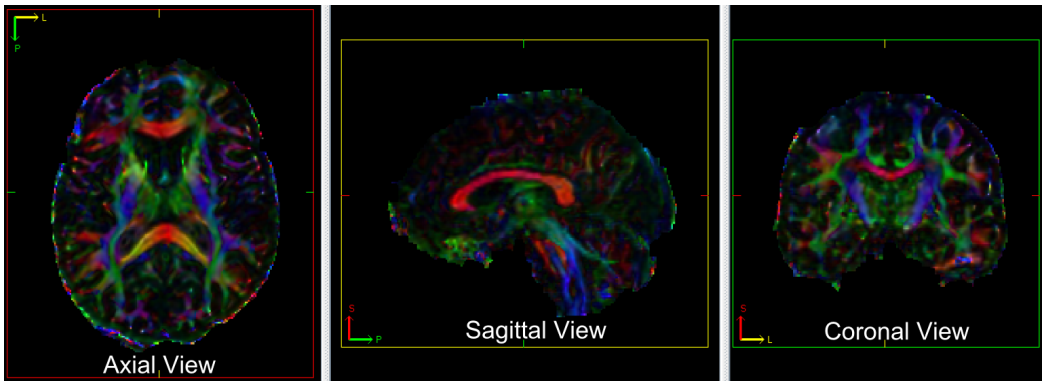

Figure 2.2: An example of the standard DTI color map display.

of the color map is shown in Figure 2.2.

DTI has been widely used for scientific studies. It has been used to study structures such as the white matter tracts [3], the cardiac muscles [38], the skeletal muscles [39], and the tongue muscles [40]. It has been applied to the studies on various types of diseases such as multiple sclerosis [8, 41], Parkinson's disease [9, 42], autism [43], Huntington's disease [10, 44], Alzheimer's disease [45, 46], mild traumatic brain injury [47], schizophrenia [48–50], and cerebellar ataxia [51]. It has also been performed to investigate the human brain connectome, which gives a structural description of the human brain network [5, 7, 52]. In these studies, fiber tracking and fiber tract segmentation are two common techniques that aid the analysis of DTI.

2.2 Fiber Tracking

Fiber tracking is used in many DTI studies. It is the process of reconstructing 3D curves that represent fiber tracts. An example of fiber tracking in the brain overlaid

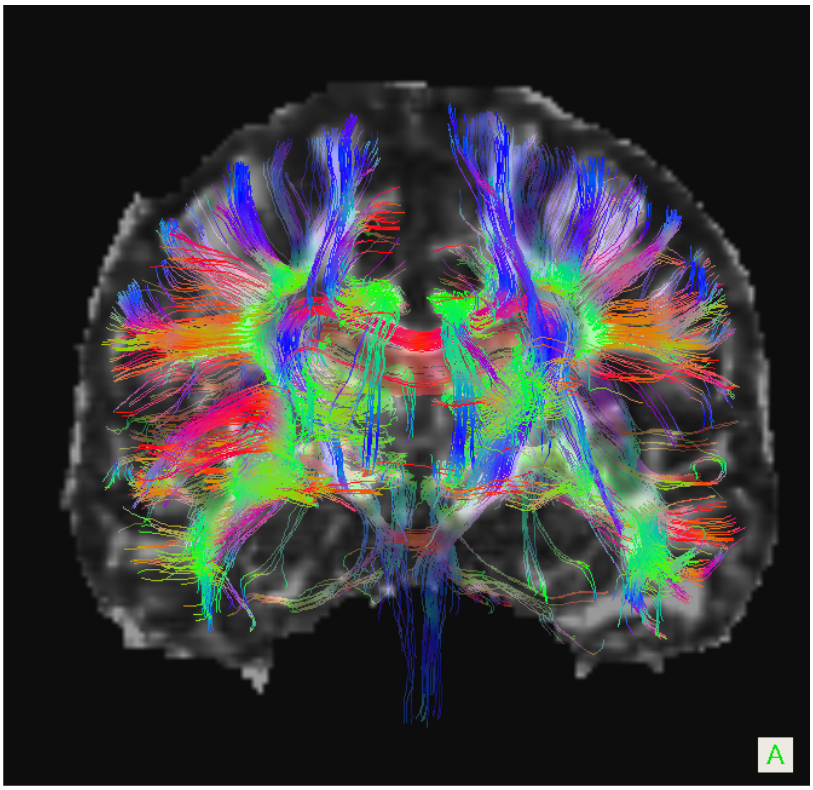

Figure 2.3: An example of fiber tracking in the brain overlaid on the FA map using DTI. The fibers are color-coded with the standard DTI scheme (red: left-right; green: front-back; and blue: up-down).

on the FA map is shown in Figure 2.3, where each segment of the fiber is color-coded with the standard DTI scheme (red: left-right; green: front-back; and blue: up-down).

Many of the fiber tracking methods on DTI use a streamlining technique based on FOs computed from DTI measurements. Figure 2.4 gives a graphical illustration of a simple streamlining strategy. Seed points can be placed in the centers of the voxels. Starting from seed points, the fibers are propagated according to the FOs, until a new FO can be used. Criteria for starting and terminating fibers are also needed. For example, FA can provide such information. Since FA is high in fiber

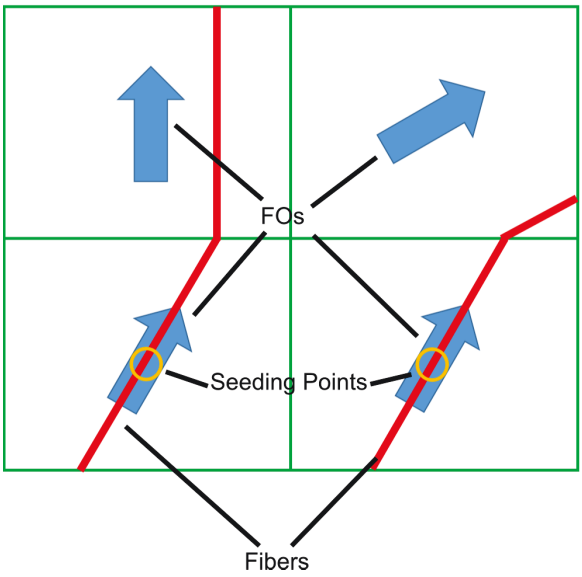

Figure 2.4: An example of streamlining fiber tracking strategy.

tracts and drops in regions with isotropic diffusion, a threshold of FA can be used so that fibers are initiated in voxels with high FA values and terminated when they arrive at voxels with low FA values [3]. Another commonly used termination criterion is the turning angle between successive FOs: because fibers are assumed to propagate smoothly, when the turning angle is larger than a threshold, the fiber streamline is terminated [3].

The estimation of FOs from DTI is the key element in fiber tracking and it is explored by a number of researchers [3, 4, 26, 27, 53–59]. Different approaches to FO estimation been been developed. The FOs can be solely computed with the local tensor independently at each voxel using its PEV [3, 54]. The estimation of FOs can also incorporate neighborhood information, where the current FO estimation can be guided by the state of its neighbors [4, 53].

A major drawback of the tensor model is that it cannot represent crossing fibers [23]. Therefore, efforts have been to address this issue. One solution is the development of more advanced diffusion imaging techniques, which acquire more comprehensive diffusion information, such as high angular resolution diffusion imaging (HARDI) [60] and diffusion spectrum imaging (DSI) [61]. One practical issue with these modalities is that they usually require a great number of gradient directions, which can be more than 100, and take a long acquisition time. This makes these modalities less practical in clinical practice.

Previous works have also explored resolving crossing fibers with DTI acquisitions by using two-tensor or multi-tensor models [26, 27, 55, 56, 58, 59]. In these works, the diffusion weighted signals are modeled as a mixture of attenuated signals from two or more tensors:

$$S_k = S_0 \sum_{i=1}^{N} f_i e^{-b\boldsymbol{g}_k^T \mathbf{D}_i \boldsymbol{g}_k} + n_k. \tag{2.10}$$

Here N is the number of tensors used in the model and f_i is the mixture fraction for $\mathbf{D}_i$. Each tensor can represent an FO given by its PEV. As in the tensor model, the FOs can be determined using the local tensors only [27, 58] or by incorporating neighborhood information [56, 58, 59].

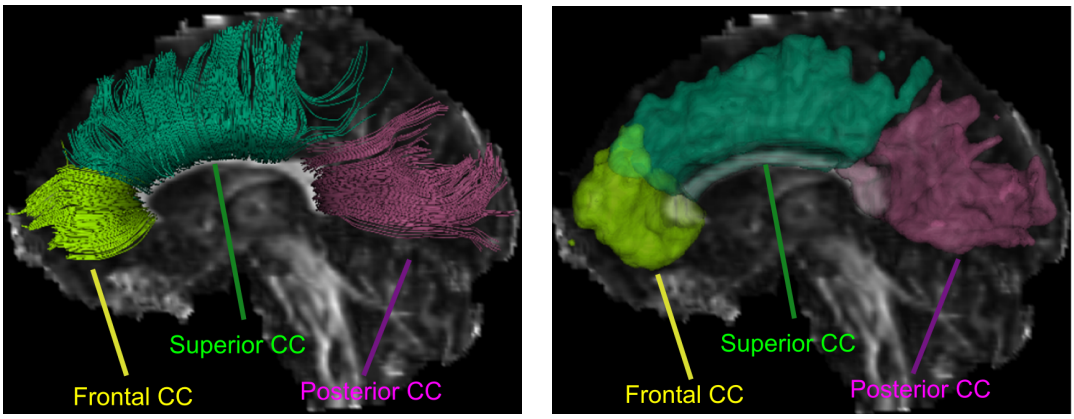

(a) Clustered Fiber Tracts (b) Volumetric Tract Segmentation

Figure 2.5: An example of (a) clustered fiber tracts and (b) volumetric tract segmentation overlaid on the FA map: frontal/posterior/superior corpus callosum.

2.3 Fiber Tract Segmentation

It is often useful to analyze tract-specific statistics for scientific studies. Therefore, the ability to segment specific tracts is necessary. Manual delineations of the fiber tracts, which are usually based on refining regions of interest (ROIs), have been used for a number of studies [62–66]. However, manual delineations can be subjective and time-consuming. Therefore, various automatic tract segmentation algorithms have been designed for objective and more efficient data analysis. Many of them cluster the fiber tracking results to acquire bundled fiber tracts [6, 14, 67–74]. An example of clustered fiber tracts is shown in Figure 2.5(a). These methods assign each fiber a label according to the properties of individual fibers and/or the relationship between fibers. For example, in [14], pairwise distances between fibers are calculated and used in a spectral clustering algorithm for fiber clustering.

An alternative approach to fiber tract segmentation is volumetric tract segmentation, which does not require the process of fiber tracking [15, 16, 75]. Compared with segmentation by fiber clustering, volumetric tract segmentation avoids the need of intermediate fiber tracking steps, and thus is not affected by the variability introduced by the choice of the fiber tracking method. In this thesis, we will focus on volumetric tract segmentation. An example of volumetric tract segmentation is displayed in Figure 2.5(b). Based on the assumption that image features, such as diffusion properties, exhibit homogeneity in voxels belonging to the same fiber tract, volumetric segmentation directly labels the voxels using their associated features. Segmentation frameworks, such as Markov random field (MRF) and level-set methods, have been used for this purpose, where speed functions or energy functions are determined based on the DTI properties [15, 16, 20, 76].

As in fiber tracking, crossing tracts can also cause problems in tract segmentation. In crossing regions, the PEV is no longer a valid estimate of an FO, and diffusion features are in general different than those in the noncrossing regions of the corresponding tracts. Therefore, directly segmenting the complete tract as one single object is difficult. A solution to the issue is given in the DOTS algorithm [15], where the crossing and noncrossing regions are modeled as separate objects. After segmentation, the noncrossing and crossing regions are combined to form the complete tract.

2.4 Examples of Fiber Tracts

For the development of fiber tracking and tract segmentation algorithms, it is always helpful to use *a priori* anatomical knowledge about fiber tracts. Different types of tracts can have different properties, which influence the designs of the methods. Common fiber tracts studied in DTI include white matter tracts and muscle fiber tracts. White matter tracts consist of bundles of axons which convey messages between gray matter areas. Muscles produce motion and force, and muscle fiber tracts can be classified into different types such as skeletal muscle, cardiac muscle, and smooth muscle. Two types of fiber tracts with which this thesis is concerned are introduced: the cerebellar peduncles and the tongue muscles.

2.4.1 Cerebellar Peduncles

The cerebellar peduncles are major white matter tracts that communicate information between the cerebellum and other brain regions, including the cerebral cortex and the spinal cord [77]. They play an important role in motor and non-motor control [78] and are known to be affected by various neurological diseases, including spinocerebellar ataxia [51, 79], schizophrenia [80], and multiple system atrophy [81]. Among the scientific studies on the cerebellar peduncles, a large number of them have been performed using DTI data [82–88].

The cerebellar peduncles comprise the superior cerebellar peduncles (SCPs), the

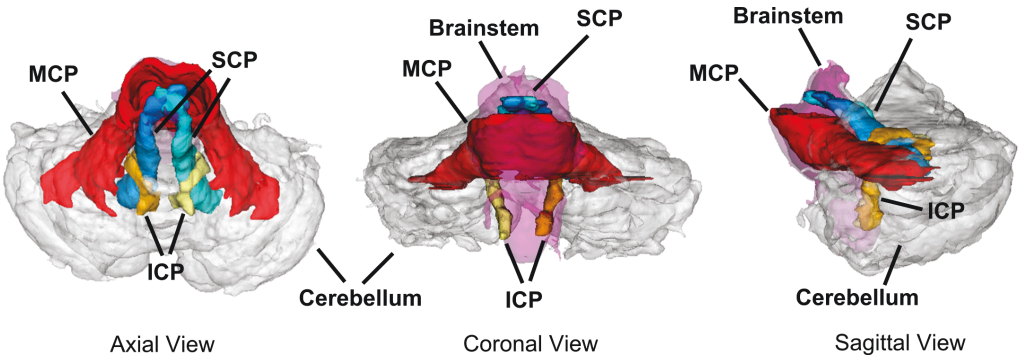

Figure 2.6: A manually drawn schematic of the cerebellar peduncles. Blue: left SCP; green: right SCP; red: MCP; orange: left ICP; yellow: right ICP. Shown together with the cerebellum (gray) and the brainstem (purple).

middle cerebellar peduncle (MCP), and the inferior cerebellar peduncles (ICPs). An illustration of the structures of the peduncles is shown in Figure 2.6, together with the cerebellum and the brainstem. The SCPs are the major efferent pathways that convey the output information from the cerebellum to the midbrain. The SCPs originate primarily from the dentate nuclei and then continue upward toward the brainstem, where the left and right SCPs cross each other in a region known as the decussation of the SCP (dSCP). The fibers then head toward the red nuclei on the opposite side, where some fibers terminate but most continue through to the thalamus [89]. The MCP is the largest afferent system of the cerebellum and acts as the afferent pathway from the pons to the cerebellum. It wraps around the pons and ends in the cerebellar cortex [89, 90]. The ICPs contain both afferent and efferent signals and connect the medulla to the cerebellum [90].

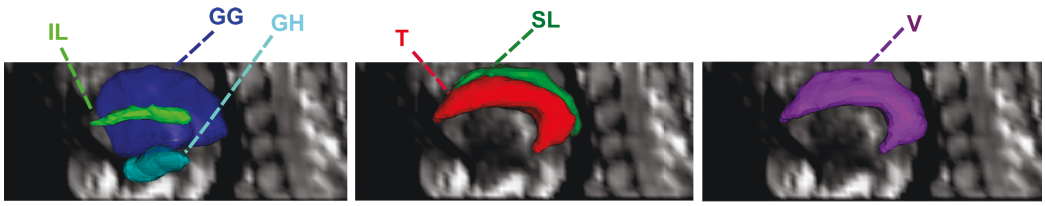

(a) Sagittal View

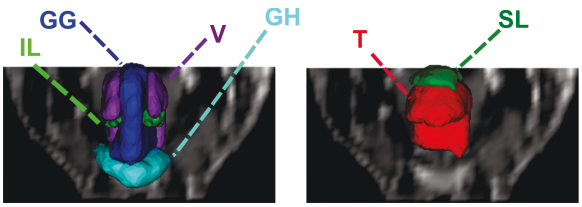

(b) Coronal View

Figure 2.7: The tongue muscles in the (a) sagittal view and (b) coronal view. Note that muscles shown together are not overlapping.

2.4.2 Tongue Muscles

The tongue is a critical organ for a variety of functions including swallowing, respiration, and speech. The tongue muscles play an important role in changing the shape and position of the tongue. They have been studied using DTI [91–94]. The tongue muscles contains intrinsic and extrinsic muscles, which differ in their origins [95]. For the intrinsic muscles, both of their origins and terminations are within the tongue, while extrinsic muscles start from external organs and are inserted into the tongue [96]. For example, the inferior longitudinal (IL) muscles, the superior longitudinal (SL) muscles, the transverse (T) muscles, and the vertical (V) muscles are intrinsic muscles, and the genioglossus (GG) and geniohyoid (GH) muscles are extrinsic muscles [97, 98]. An example of volumetric representation of part of the tongue muscles is shown in Figure 2.7.

Table 2.1: A summary of interdigitated tongue muscles. Note: "n" and "x" stand for noncrossing and crossing, respectively.

	GG	GH	IL	SL	T	V
GG		n	n	x	x	n
GH	n		n	n	n	n
IL	n	n		n	n	n
SL	x	n	n		n	x
T	x	n	n	n		x
V	n	n	n	x	x	

It should be noted that tongue muscles can interdigitate. For example, T interdigitates with GG near the mid-sagittal planes and with V on lateral parts of the tongue. GG and V intersect with SL near the top and back surface of the tongue. A summary of the interdigitation of the muscles in Figure 2.7 is listed in Table 2.1.

2.5 Summary

This chapter introduced the background knowledge on DTI, fiber tracking, and tract segmentation. In particular, crossing fibers are a major issue in DTI which must be addressed. The anatomical knowledge of the cerebellar peduncles and tongue muscles were also introduced. In the chapters to follow, the proposed fiber tracking and tract segmentation methods that can resolve crossing fibers will be presented. Results of these methods will be demonstrated on (but not limited to) the fiber tracts discussed in this chapter.

Chapter 3

Fiber Tracking Guided by Volumetric Tract Segmentation

3.1 Motivation

In the streamlining fiber tracking process, errors can be caused by crossing fibers and image noise [24]. Anatomical knowledge of tracts has been explored to overcome such errors and aid fiber tracking. Cheng et al. [24] obtain anatomical information from an initial fiber tracking, where the center line of a fiber bundle is calculated. Then the final fiber tracking is guided by the center line. Aranda et al. [99] use a "flocking" model to incorporate the interactions between neighbor fiber streamlines. By examining the collective behavior of the pathways belonging to the same group, the fiber orientation (FO) is modified accordingly. However, as the anatom-

ical information also comes from tractography, no real prior anatomical knowledge is incorporated in [24] and [99]. Kleinnijenhuis et al. [25] use an additional image modality, high field gradient echo magnetic resonance imaging, to provide anatomical information. In these images, contrast can be observed between fiber bundles due to susceptibility differences. Structure tensors are computed in the images and used to inform the FOs for fiber tracking. Yet, the method is limited to the diffusion tensor imaging (DTI) data sets where high field gradient echo images have also been acquired. Furthermore, all of these methods are based on local cues about possible FOs; they do not use knowledge of the positions of tracts and their likely regions of overlap.

Another source of anatomical information, which has not received much attention, is volumetric tract segmentation. It contains tract information such as shape and location, and can be used to inform fiber tracking. Volumetric tract segmentation labels each voxel with a tract class and does not necessarily require the process of fiber tracking [15–17, 19]. For example, Bazin et al. [15] proposed the DOTS algorithm, which is an atlas-based Markov random field algorithm designed to label the voxels on DTI. The DOTS tract atlas provides diffusion and spatial prior anatomical information, which is used together with the connectivity between neighbor voxels to segment the fiber tracts. In addition, the method is able to identify crossing tracts by explicitly modeling the crossing regions as separate labels. A complete tract can be obtained by combining the noncrossing and crossing portions after segmentation. Awate et al. [16]

proposed a fuzzy-segmentation method that models the tensors in Riemannian spaces and solves the segmentation problem with a Markov random field. In [19], volumetric distributions of the fiber tract pathways are obtained within a Bayesian framework using a Markov chain Monte Carlo (MCMC) algorithm, where volumetric tract segmentation can be obtained. In [17], a level set framework is used to label the fiber tracts volumetrically on high angular resolution diffusion imaging (HARDI), where speeds are determined by the principal diffusion directions and spherical harmonic coefficients.

In this work, we explore the incorporation of anatomical knowledge into FO estimation by using guidance from volumetric segmentation of fiber tracts. We use the DOTS algorithm [15] to provide the volumetric segmentation because 1) it is based on DTI data, 2) it provides anatomical tract information, and 3) it is able to identify crossing tracts. We use the maximum a posteriori (MAP) estimation technique to estimate the FOs. The anatomical information from the volumetric tract segmentation is modeled in the prior distribution together with the spatial smoothness of the FOs. The diffusion information is encoded in the likelihood term. Calculus of variations is applied to the resulting objective function to yield Euler-Lagrange equations, which are solved iteratively to estimate the FOs. Using the estimated FOs, a streamlining fiber tracking strategy is also presented.

3.2 Theory and Algorithm

In this section, we first describe the DOTS algorithm for volumetric tract segmentation. Then we describe our MAP framework and algorithm for FO estimation using the results of tract segmentation. Finally, we describe a streamlining fiber tracking strategy using the estimated FOs and tract segmentation.

3.2.1 DOTS Algorithm

DOTS is an atlas-based volumetric tract segmentation algorithm using a Markov random field (MRF) framework [15]. It is available at `http://www.nitrc.org/projects/dots/`. The atlas of the white matter tracts is built according to [90]. The energy function specifying the MRF is given by

$$E(l) = \sum_{x} \left(V_1(x, l(x)) + \sum_{y \in N_x} V_2(x, y, l(x), l(y)) \right). \tag{3.1}$$

Here, V_1 is a unary energy term at x with the label of $l(x)$, and V_2 is a pairwise energy term that models the interaction between the voxel at x labeled as $l(x)$ and the voxels in its neighborhood N_x at location y with the label of $l(y)$. The unary term combines the diffusion information in the data with the atlas to model the likelihood of label $l(x)$ at location x. The pairwise term uses the connection information from DTI to encode the interaction between neighbor voxels. Each voxel is assigned a label after the energy function is optimized. Details about the specification of V_1 and V_2 and

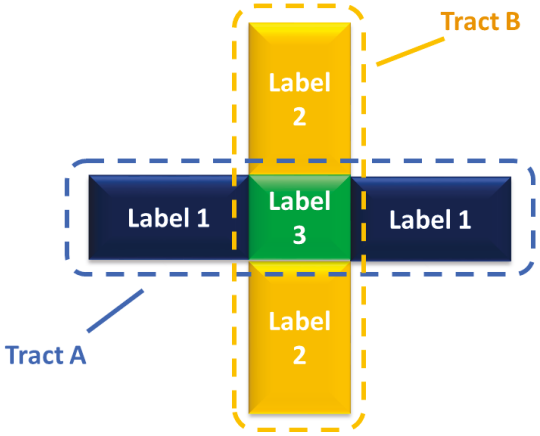

Figure 3.1: A graphical illustration showing the DOTS strategy for segmenting crossing tracts.

the optimization of $E(l)$ are found in [15].

Note that the DOTS algorithm is able to resolve crossing tracts by explicitly modeling the crossing region of each pair of crossing tracts as a separate label. The schematic in Figure 3.1 provides a graphical illustration of the DOTS strategy for processing crossing tracts. After the MRF assigns a label to each voxel, the noncrossing and crossing regions of a tract are combined to create a representation of the complete tract. For example, in Figure 3.1 Tract A consists of Label 1 and Label 3 while Tract B consists of Label 2 and Label 3.

3.2.2 MAP Estimation of FOs

Consider a region in the brain that is segmented as tract $\mathcal{L} = \mathcal{L}_{\mathrm{n}} \cup \mathcal{L}_{\mathrm{c}}$ by DOTS, where $\mathcal{L}_{\mathrm{n}}$ and $\mathcal{L}_{\mathrm{c}}$ are the noncrossing and crossing regions, respectively. We seek to estimate the FOs (unit vectors) in the whole tract with guidance from both the

volumetric tract segmentation and diffusion information. For this purpose, three core assumptions are made: 1) fibers propagate smoothly inside a tract; 2) fibers propagate along the tract surface, i.e., orthogonal to surface normals, except at tract ends; and 3) in noncrossing tract regions, the FOs generally agree with the primary eigenvectors (PEVs) of the diffusion tensors. As described next, we use an MAP estimation strategy that incorporates these three assumptions.

Given the diffusion tensors and the tract segmentation, the PEVs $\boldsymbol{v}$ of the tensors and the surface normals $\boldsymbol{g}$ of the whole tract $\mathcal{L}$ can be calculated. Note that to account for possible inaccuracy and roughness of tract segmentation, we first apply a morphological restoration and then a Gaussian smoothing to the whole tract segmentation $\mathcal{L}$. Thus, the tract surface normal is calculated as

$$\boldsymbol{g} = \frac{\nabla G_\sigma(\Phi_\bullet(\Phi_\circ(\mathcal{L})))}{|\nabla G_\sigma(\Phi_\bullet(\Phi_\circ(\mathcal{L})))|}, \tag{3.2}$$

where $\Phi_\circ(\cdot)$ and $\Phi_\bullet(\cdot)$ are morphological opening and closing, respectively, and $G_\sigma(\cdot)$ is Gaussian smoothing. In this work, the radius of the structural element is 1 mm, and the standard deviation of the Gaussian kernel is 0.35 mm. The estimate of the FO $\boldsymbol{f}$ can then be formulated as

$$\hat{\boldsymbol{f}} = \arg\max_{|\boldsymbol{f}|=1} P(\boldsymbol{f}|\boldsymbol{v};\boldsymbol{g}), \tag{3.3}$$

where the constraint of $|\boldsymbol{f}| = 1$ ensures that the FOs are estimated as unit vectors.

We can expand $P(\boldsymbol{f}|\boldsymbol{v};\boldsymbol{g})$ as follows

$$P(\boldsymbol{f}|\boldsymbol{v};\boldsymbol{g}) = \frac{P(\boldsymbol{f};\boldsymbol{g})P(\boldsymbol{v}|\boldsymbol{f})}{\int P(\boldsymbol{f};\boldsymbol{g})P(\boldsymbol{v}|\boldsymbol{f})\mathrm{d}\boldsymbol{f}} = \frac{1}{Z}P(\boldsymbol{f};\boldsymbol{g})P(\boldsymbol{v}|\boldsymbol{f}) \propto P(\boldsymbol{f};\boldsymbol{g})P(\boldsymbol{v}|\boldsymbol{f}), \quad (3.4)$$

where $Z = \int P(\boldsymbol{f};\boldsymbol{g})P(\boldsymbol{v}|\boldsymbol{f})\mathrm{d}\boldsymbol{f}$ is a constant. Here, $P(\boldsymbol{f};\boldsymbol{g})$ is the prior distribution of the FO, where $\boldsymbol{g}$ is a parameter, and $P(\boldsymbol{v}|\boldsymbol{f})$ is the likelihood term. We specify each of these terms in the following sections.

3.2.2.1 Prior Distribution

The prior distribution contains information about smoothness and tract segmentation. It can be modeled as

$$P(\boldsymbol{f};\boldsymbol{g}) = P_1(\boldsymbol{f})P_2(\boldsymbol{f};\boldsymbol{g}), \quad (3.5)$$

where $P_1(\boldsymbol{f})$ ensures smoothness and $P_2(\boldsymbol{f};\boldsymbol{g})$ enforces a tract constraint. First, $P_1(\boldsymbol{f})$ is modeled using the gradients of $\boldsymbol{f}$ to preserve smoothness:

$$P_1(\boldsymbol{f}) \propto e^{-\alpha \sum\limits_{x\in\mathcal{L}} |\nabla \boldsymbol{f}(x)|^2}, \quad (3.6)$$

where α is a constant to be specified by the user. Given this term, when the FOs are smoother, the sum of squared gradient magnitudes are smaller, and this corresponds to a higher value of the prior density. Second, to encourage the fibers to propagate

in a direction orthogonal to the tract surface normals, $P_2(\boldsymbol{f};\boldsymbol{g})$ is modeled using the inner product between $\boldsymbol{f}$ and $\boldsymbol{g}$:

$$P_2(\boldsymbol{f};\boldsymbol{g}) \propto e^{-\sum_{x\in\mathcal{L}} \mu(x)|\boldsymbol{g}(x)\cdot\boldsymbol{f}(x)|^2}. \tag{3.7}$$

Thus, higher prior probability is given when the FO is closer to being orthogonal to the tract surface normal. The function $\mu(x)$ is used to discriminate between the *sides* of tracts and the *ends* of tracts. Since tract ends are usually in noncrossing regions and the PEVs at tract ends are close to being parallel to the tract surface normals, $\mu(x)$ is specified as:

$$\mu(x) = \begin{cases} 0, & \text{if} \quad |\boldsymbol{g}(x)\cdot\boldsymbol{v}(x)| > t \quad \text{and} \quad x \in \mathcal{L}_{\text{n}} \\ \mu_0, & \text{otherwise} \end{cases}, \tag{3.8}$$

where t is a threshold ($t = 0.5$ in this work) and μ_0 controls the influence of tract segmentation when the surface normal constraint is used. Note that $\boldsymbol{g}(x)$ and $\boldsymbol{v}(x)$ are unit vectors. In practice, this criterion gives a good identification of the tract ends. Therefore, the complete joint prior density is modeled as:

$$P(\boldsymbol{f};\boldsymbol{g}) \propto e^{-\sum_{x\in\mathcal{L}} (\alpha|\nabla\boldsymbol{f}(x)|^2 + \mu(x)|\boldsymbol{g}(x)\cdot\boldsymbol{f}(x)|^2)}, \tag{3.9}$$

where α and $\mu(x)$ together decide the relative weightings of the constraints of smoothness and tract segmentation.

3.2.2.2 Likelihood

Suppose the likelihood $P(\boldsymbol{v}|\boldsymbol{f})$ is independent between voxels. Then we have

$$P(\boldsymbol{v}|\boldsymbol{f}) = \prod_{x \in \mathcal{L}} p(\boldsymbol{v}(x)|\boldsymbol{f}(x)), \tag{3.10}$$

where $p(\boldsymbol{v}(x)|\boldsymbol{f}(x))$ is the local likelihood term at each voxel x. The local likelihood term is modeled differently in different regions. In crossing regions, we model the FO and the PEV as independent variables because the PEV is no longer a valid estimate of the FO. Thus, the likelihood term is a uniform distribution in each direction. In noncrossing regions, the PEV provides an estimate of the FO, and the likelihood term is modeled as a Gaussian distribution. Therefore, the local likelihood term in the complete tract is modeled as:

$$p(\boldsymbol{v}(x)|\boldsymbol{f}(x)) = \begin{cases} \text{constant}, \ x \in \mathcal{L}_{\text{c}} \\ \\ \frac{1}{Z_l} e^{-\lambda_0 |\boldsymbol{v}(x) - \boldsymbol{f}(x)|^2}, \ x \in \mathcal{L}_{\text{n}} \end{cases}, \tag{3.11}$$

where Z_l is a normalization constant and λ_0 is a constant that controls the influence of data fidelity in noncrossing regions.

3.2.2.3 Objective Function and Optimization

Now that the prior density and likelihood terms have been specified, and using the assumption of voxel independence, we can write the FO estimate as

$$\begin{aligned}\hat{\boldsymbol{f}} &= \underset{|\boldsymbol{f}(x)|=1}{\arg\max}\, P(\boldsymbol{f};\boldsymbol{g}) \prod_{x\in\mathcal{L}} p(\boldsymbol{v}(x)|\boldsymbol{f}(x)) \\ &= \underset{|\boldsymbol{f}(x)|=1}{\arg\max} \left\{ \prod_{x\in\mathcal{L}_{\mathrm{n}}} e^{-(\alpha|\nabla \boldsymbol{f}(x)|^2+\mu(x)|\boldsymbol{g}(x)\cdot\boldsymbol{f}(x)|^2)} e^{-\lambda_0|\boldsymbol{v}(x)-\boldsymbol{f}(x)|^2} \right\} \times \\ &\quad \left\{ \prod_{x\in\mathcal{L}_{\mathrm{c}}} e^{-(\alpha|\nabla \boldsymbol{f}(x)|^2+\mu(x)|\boldsymbol{g}(x)\cdot\boldsymbol{f}(x)|^2)} \right\}. \end{aligned} \tag{3.12}$$

By taking the logarithm and combining noncrossing and crossing regions, we have

$$\begin{aligned}\hat{\boldsymbol{f}} &= \underset{|\boldsymbol{f}(x)|=1}{\arg\min} \sum_{x\in\mathcal{L}} (\alpha|\nabla \boldsymbol{f}(x)|^2 + \mu(x)|\boldsymbol{g}(x)\cdot\boldsymbol{f}(x)|^2 + \\ &\qquad \lambda(x)|\boldsymbol{v}(x)-\boldsymbol{f}(x)|^2), \end{aligned} \tag{3.13}$$

where

$$\lambda(x) = \begin{cases} \lambda_0, & x\in\mathcal{L}_{\mathrm{n}} \\ 0, & x\in\mathcal{L}_{\mathrm{c}} \end{cases}. \tag{3.14}$$

To solve the minimization problem, we write the objective function in Eq. (3.13)

in continuous form and relax the constraint of $|\boldsymbol{f}(x)| = 1$:

$$E(\boldsymbol{f}) = \int \alpha|\nabla \boldsymbol{f}(x)|^2 + \mu(x)|\boldsymbol{g}(x) \cdot \boldsymbol{f}(x)|^2 + \lambda(x)|\boldsymbol{v}(x) - \boldsymbol{f}(x)|^2 \mathrm{d}x. \tag{3.15}$$

For convenience, hereafter we drop the location x in the equations. Suppose $\boldsymbol{f} = (f_x, f_y, f_z)$, $\boldsymbol{v} = (v_x, v_y, v_z)$, and $\boldsymbol{g} = (g_x, g_y, g_z)$; then the Euler-Lagrange equations for Eq. (3.15) can be obtained using calculus of variations [100]:

$$\begin{aligned}
\alpha\nabla^2 f_x &= \mu g_x(f_x g_x + f_y g_y + f_z g_z) + \lambda(f_x - v_x), \\
\alpha\nabla^2 f_y &= \mu g_y(f_x g_x + f_y g_y + f_z g_z) + \lambda(f_y - v_y), \\
\alpha\nabla^2 f_z &= \mu g_z(f_x g_x + f_y g_y + f_z g_z) + \lambda(f_z - v_z).
\end{aligned} \tag{3.16}$$

Using the numerical strategy in [101], the following iterations can be applied to estimate $\boldsymbol{f}$ (see Appendix 3.A for a derivation). At the k-th iteration,

$$\begin{aligned}
f_x^{k+1} &= \overline{f_x^k} - \frac{\mu g_x(g_x\overline{f_x^k} + g_y\overline{f_y^k} + g_z\overline{f_z^k})}{\alpha + \lambda + \mu(g_x^2 + g_y^2 + g_z^2)} + \\
&\quad \frac{\lambda[(\alpha+\lambda)(v_x - \overline{f_x^k}) + \mu(g_y^2 + g_z^2)(v_x - \overline{f_x^k}) - \mu g_x g_y(v_y - \overline{f_y^k}) - \mu g_x g_z(v_z - \overline{f_z^k})]}{(\alpha+\lambda)(\alpha + \lambda + \mu(g_x^2 + g_y^2 + g_z^2))}, \\
f_y^{k+1} &= \overline{f_y^k} - \frac{\mu g_y(g_x\overline{f_x^k} + g_y\overline{f_y^k} + g_z\overline{f_z^k})}{\alpha + \lambda + \mu(g_x^2 + g_y^2 + g_z^2)} + \\
&\quad \frac{\lambda[(\alpha+\lambda)(v_y - \overline{f_y^k}) - \mu g_x g_y(v_x - \overline{f_x^k}) + \mu(g_x^2 + g_z^2)(v_y - \overline{f_y^k}) - \mu g_y g_z(v_z - \overline{f_z^k})]}{(\alpha+\lambda)(\alpha + \lambda + \mu(g_x^2 + g_y^2 + g_z^2))}, \\
f_z^{k+1} &= \overline{f_z^k} - \frac{\mu g_z(g_x\overline{f_x^k} + g_y\overline{f_y^k} + g_z\overline{f_z^k})}{\alpha + \lambda + \mu(g_x^2 + g_y^2 + g_z^2)} + \\
&\quad \frac{\lambda[(\alpha+\lambda)(v_z - \overline{f_z^k}) - \mu g_x g_z(v_x - \overline{f_x^k}) - \mu g_y g_z(v_y - \overline{f_y^k}) + \mu(g_x^2 + g_y^2)(v_z - \overline{f_z^k})]}{(\alpha+\lambda)(\alpha + \lambda + \mu(g_x^2 + g_y^2 + g_z^2))},
\end{aligned} \tag{3.17}$$

where $\overline{f_x^k}$, $\overline{f_y^k}$, and $\overline{f_z^k}$ are the local averages of f_x^k, f_y^k, and f_z^k, respectively.

Eq. (3.17) gives an iterative algorithm for the estimation of the FOs throughout a given tract $\mathcal{L}$. The initial values for $\boldsymbol{f}$ are provided by the PEVs in the noncrossing regions and zero vectors in the crossing regions. After each iteration k, we project nonzero $\boldsymbol{f}^{k+1}$ onto the unit sphere by normalization: $\boldsymbol{f}^{k+1} := \frac{\boldsymbol{f}^{k+1}}{|\boldsymbol{f}^{k+1}|}$. The iterative update terminates when the average difference between normalized $\boldsymbol{f}^{k+1}$ and $\boldsymbol{f}^k$ is below a threshold or the maximal number of iterations is reached. Assuming the update terminates at the K-th iteration, we have the normalized vectors $\boldsymbol{f}^{K+1}$ as the final estimated FOs.

3.2.3 Fiber Tracking Using the Estimated FOs

Given estimated FOs in each tract, streamlining fiber tracking can be performed. Here we use a strategy that is similar to the FACT algorithm [3]. Each FO is used to propagate the fiber streamlines in the current voxel until they reach the next voxel. For a streamline seeded in a tract, the FOs of the corresponding tract are used for propagation inside the tract, and outside the tract the PEVs are used.

A start fractional anisotropy (FA) threshold is used to initialize fiber tracking: only voxels with FA larger than the start threshold can be used as seeding voxels. A stop FA threshold is used to terminate fiber tracking: in noncrossing regions, when a streamline reaches a voxel with FA below the stop FA threshold, fiber tracking is terminated; in crossing regions, the stop FA threshold is not used. A turning

angle threshold is also employed for terminating the fiber tracking: when the angle between the FOs in the current step and the previous step is larger than the turning angle threshold, fiber tracking is terminated. In this work, both the start and stop FA thresholds are 0.2 and the angle threshold is 40°, which are typical values in deterministic streamlining fiber tracking algorithms [102, 103].

3.3 Experiments

The proposed method was first performed on a 3D digital crossing phantom, then on the Fiber Cup phantom [104, 105], and finally on brain DTI data from 18 healthy subjects. In all three experiments, the proposed method was compared with two FO estimation methods on DTI: the BEDPOSTX algorithm [26] as implemented in the FSL software [106] (`http://fsl.fmrib.ox.ac.uk/fsl/fslwiki/`) and the CFARI algorithm [27] as implemented in the JIST software [107] (`http://www.nitrc.org/plugins/mwiki/index.php/jist:CFARI`). BEDPOSTX uses a two-tensor model to resolve crossing fibers [26] and CFARI uses a multi-tensor model with a fixed tensor basis to estimate crossing FOs [27].

3.3.1 Digital Crossing Phantom

A 3D digital crossing phantom simulating two tracts crossing at 90° was generated for a proof-of-concept experiment (see Figure 3.2). One $b0$ image (the image without

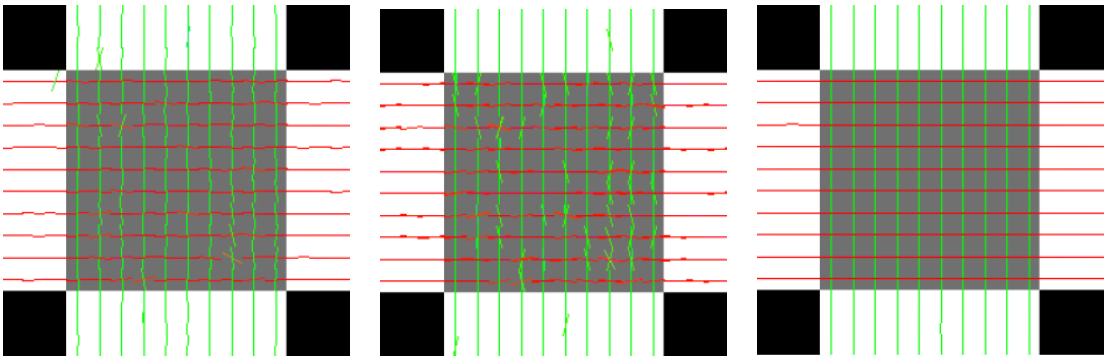

(a) BEDPOSTX (b) CFARI (c) Proposed

Figure 3.2: An example of estimated FOs in the crossing phantom test overlaid on the FA map.

diffusion weighting) and 30 diffusion gradient directions with b-values of 700 s/mm^2 were used. The $b0$ image has intensity $S_0 = 1$. Rician noise ($\sigma = 0.05$) was added to the diffusion weighted images (DWIs). We used the labels of the two tracts as the segmentation. An example of the FOs estimated by the proposed method ($\alpha = 3$, $\lambda_0 = 1$, and $\mu_0 = 50$) is shown in Figure 3.2(c), where it can be seen that the crossing FOs are correctly estimated. The proposed method was also compared with BEDPOSTX and CFARI in Figures 3.2(a) and 3.2(b), respectively. In both non-crossing and crossing regions, BEDPOSTX and CFARI produce more noisy results. In addition, in noncrossing regions, BEDPOSTX sometimes creates unreal crossing patterns.

To quantitatively evaluate the results, we use the following error measure at each

Table 3.1: The mean errors of the estimated FOs in Figure 3.2 (with standard deviations in parentheses)

	BEDPOSTX	CFARI	Proposed
Crossing Region	5.749° (5.523°)	5.210° (3.292°)	0.126° (0.067°)
Noncrossing Region	2.609° (3.406°)	1.001° (1.927°)	0.979° (0.567°)

voxel:

$$e_{\mathrm{FO}} = \max\left(\frac{1}{N_1}\sum_{i=1}^{N_1}\min_j \arccos(\boldsymbol{v}_i\cdot\boldsymbol{u}_j), \frac{1}{N_2}\sum_{j=1}^{N_2}\min_i \arccos(\boldsymbol{v}_i\cdot\boldsymbol{u}_j)\right)\cdot\frac{180^\circ}{\pi}. \quad (3.18)$$

Here, N_1 is the number of estimated FOs $\boldsymbol{v}_i$, and N_2 is the number of ground truth FOs $\boldsymbol{u}_j$. N_2 can be 1 or 2, depending on whether crossing fibers exists at the location. The first term in the max function measures how far away the estimated directions are from the ground truth, and the second term in the max function measures how accurate the true directions are estimated. Both terms are expected to be small when a good estimate is achieved; therefore, a max operation is used as the error measure. Table 3.1 lists the means and standard deviations of FO estimation errors in Figure 3.2 for noncrossing and crossing regions separately. The proposed method estimates the FOs more accurately than BEDPOSTX and CFARI.

Next, we studied the effects of the parameters in the proposed method. Since there are only two degrees of freedom in choosing the parameters, we fixed $\lambda_0 = 1$, and tested different combinations of α and μ_0. The errors are shown in Figure 3.3. It can be seen that with the true tract labels, the error is reduced when the information of the tract segmentation is used, which is represented by the cases where $\mu_0 \neq 0$. We can also observe that the errors are reduced with increasing α.

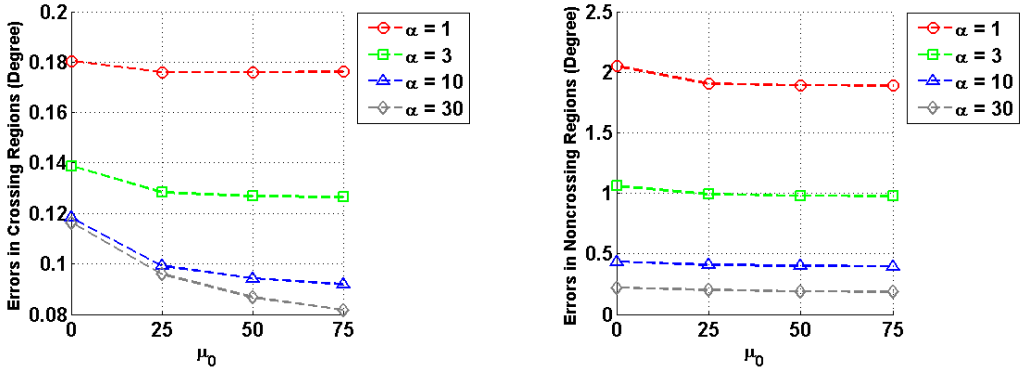

(a) Crossing Regions (b) Noncrossing Regions

Figure 3.3: The errors of estimated FOs using the proposed method with different parameter settings in (a) crossing regions and (b) noncrossing regions.

3.3.2 Fiber Cup Phantom

The proposed method was also run on the Fiber Cup phantom [104,105] and compared with BEDPOSTX and CFARI. For this experiment, we selected the acquisition with 3 mm isotropic resolution and the b-value of 650 s/mm^2, which most resembles standard DTI protocols. The acquisition has two repeated scans, and each of them has one $b0$ image and 64 gradient directions.

The 3D tract segmentation required for the proposed method was manually delineated on the phantom. We defined five tracts, which can be seen overlaid on a $b0$ axial image in Figure 3.4. Then, the proposed FO estimation was carried out with $\alpha = 3$, $\lambda_0 = 1$, and $\mu_0 = 50$. We highlight two crossing regions and compare the proposed FO estimation results with BEDPOSTX and CFARI in Figure 3.4. It can be seen that the proposed method is able to resolve crossing FOs with the manually defined tracts, while the other two methods often fail to recover the crossing FOs.

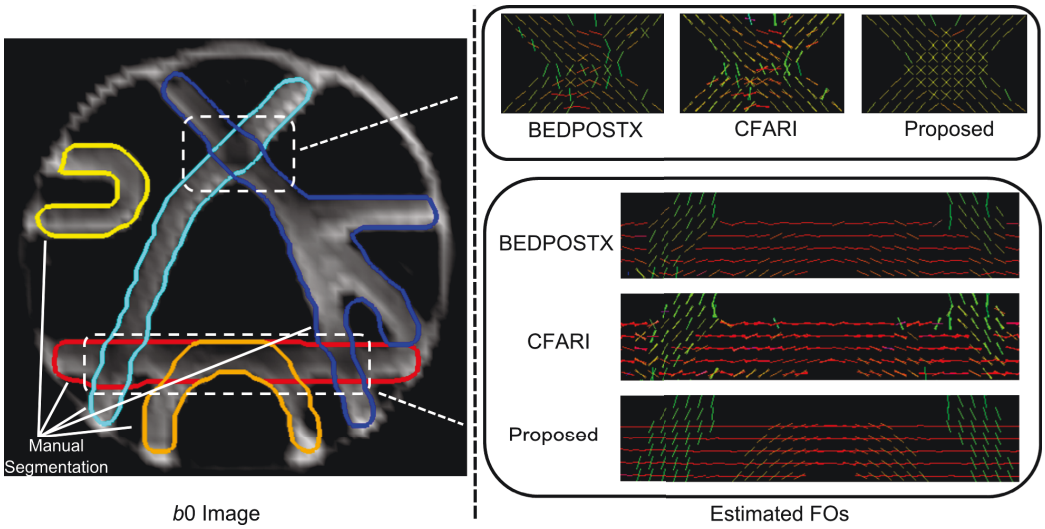

Figure 3.4: The Fiber Cup phantom ($b0$ image), manually delineated 3D tract segmentation, and estimated FOs in the two highlighted crossing regions.

3.3.3 Brain DTI

The method was applied to a brain DTI data set comprising 18 healthy subjects. The DWIs were acquired on a 3T MR scanner (Intera, Philips Medical Systems, Netherlands) using a multi-slice, single-shot EPI sequence. The sequence consists of 30 diffusion gradient directions, each with $b = 700$ s/mm^2, and one $b0$ image. The native in-plane resolution is 2.2 mm $\times$ 2.2 mm (matrix size: 96 $\times$ 96), and the native slice thickness is 2.2 mm. The scanner resampled the slices and generated the output resolution of 0.828 mm $\times$ 0.828 mm $\times$ 2.2 mm (matrix size: 256 $\times$ 256). We then isotropically resampled the DWIs, yielding an isotropic voxel resolution of 0.828 mm, and the diffusion tensors were calculated with CATNAP [108].

DOTS was applied to the acquired diffusion data set. In this experiment, we demonstrate the results for the tracts of the anterior/posterior/superior thalamic

radiation (ATR/PTR/STR), the frontal/posterior/superior corpus callosum (CCF/CCP/CCS), the corticopontine tract (CPT), and the optic radiation (OPR). Except for the CCF, the CCP, and the CCS, which cross the midline of the brain, we selected the left side of these tracts for demonstration. An example of the DOTS segmentation of these tracts is shown in Figure 3.5. Here we are showing the complete tracts, where noncrossing and crossing regions are already combined.

Using the tract segmentation from DOTS, we estimated the FOs within each tract and then carried out tractography using these results. The seeding voxels were decided as follows. For each tract, we first calculated the signed distance map from the corresponding binary tract segmentation mask. Then, among the voxels inside the tract, we selected the ones that are more than d voxels away from the tract boundary. This step is to account for possible tract overestimation in the segmentation algorithm. Finally, among these voxels, only those in the noncrossing regions were used as seeding voxels.

3.3.3.1 Demonstration on a Representative Subject

We compared our fiber tracking results with three methods on a representative subject. First, FACT [3] was used as a baseline tractography method. The method is based on the single tensor model and cannot resolve crossing fibers. Second, we used the BEDPOSTX algorithm [26] to estimate FOs followed by the XST algorithm [109] to perform fiber tracking. Third, we applied the CFARI algorithm and INFACT

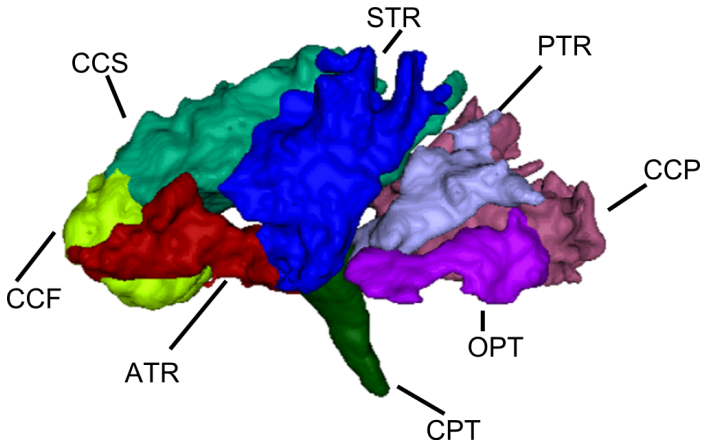

Figure 3.5: An example of DOTS segmentation of the tracts demonstrated in this work.

tracking, which are both described in [27]. The second and third methods are designed to resolve crossing fibers. Based on the fiber tracking results, the connectivity of fiber tracts to cortical labels was also calculated and compared. Here the connectivity is represented by the counts of reconstructed streamlines hitting the labels. Note that as suggested in [110] we use the term "counts of streamlines" instead of fiber counts, because tractography does not produce estimates of actual nerve fibers. The cortical labels were obtained using the method in [111] as implemented in the FreeSurfer software [112] (`https://surfer.nmr.mgh.harvard.edu/`). The fiber tracking results and the connectivity results are shown in Figures 3.6 to 3.13. The tracked streamlines are overlaid on the FA map.

As can be seen in Figure 3.6, in contrast to the other three methods, the proposed method does not create the false ATR streamlines that cross the hemisphere. Also, the proposed method reduces the false PTR and STR streamlines. The reduction of false

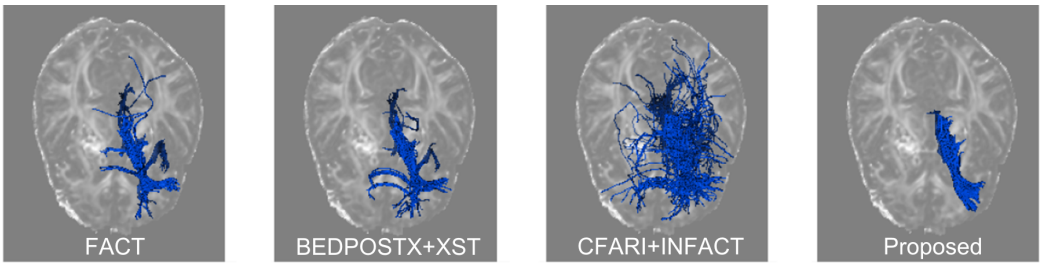

(a) Left ATR

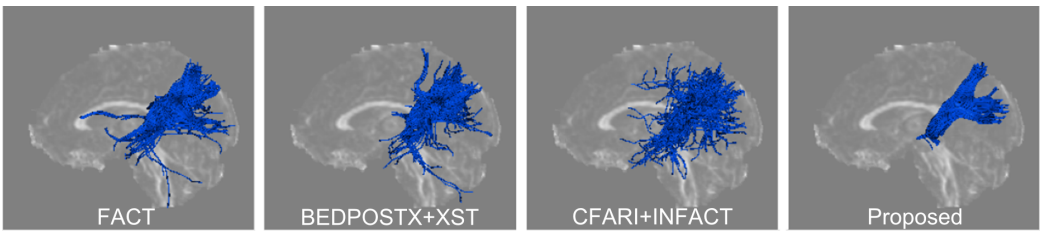

(b) Left PTR

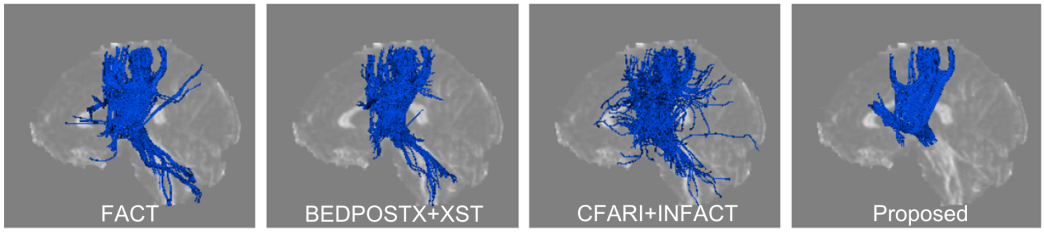

(c) Left STR

Figure 3.6: Fiber tracking results overlaid on the FA map: (a) ATR, (b) PTR, and (c) STR.

fiber streamlines can also be observed from the connectivity results in Figure 3.7. The proposed method does not produce the connections between the hemispheres, and produces a more concentrated connectivity pattern, which reflects that fewer false streamlines are tracked.

Figures 3.8(a) and 3.8(b) show that for the CCF and the CCP the proposed method does not generate the false streamlines that enter the cingulum tract which propagate in the anterior-posterior direction. This is also demonstrated in the connectivity maps in Figure 3.9 (the first and second rows). For the CCS, the proposed

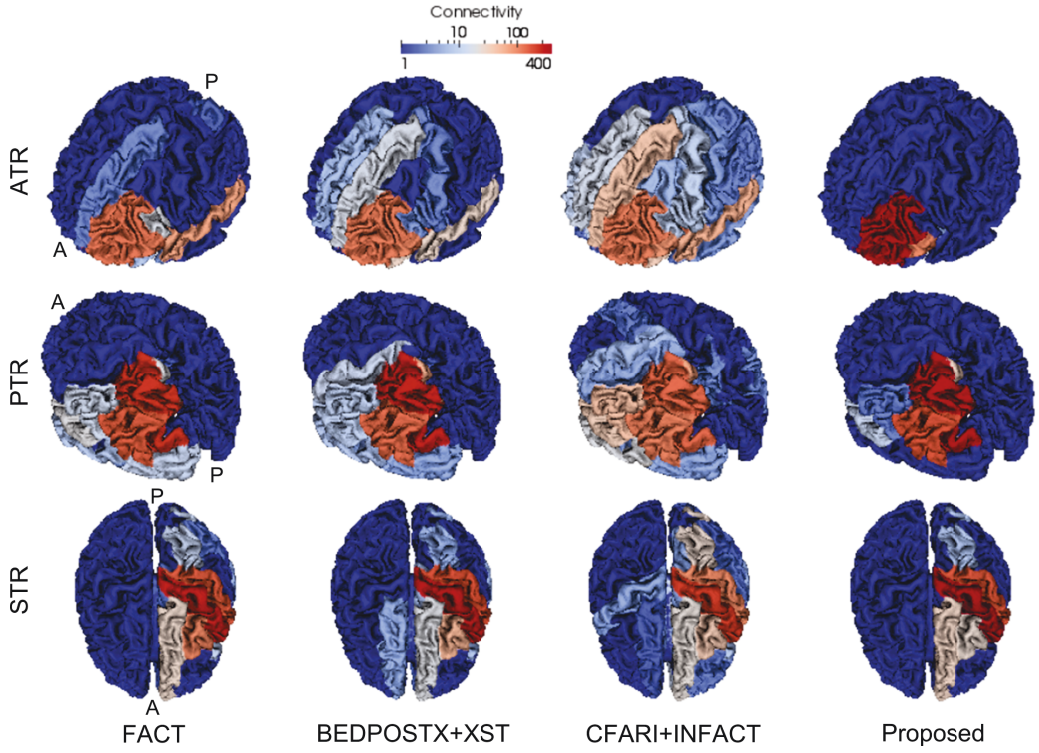

Figure 3.7: Connectivity to cortical labels: ATR, PTR, and STR. The orientations are identified in the first column.

method prevents the streamlines from entering the corticopontine tract that propagates in the inferior-superior direction, as shown in Figure 3.8(c). Figure 3.9 (the third row) shows the difference in CCS connectivity between the methods.

In Figure 3.10, the proposed method does not produce the false CPT streamlines that enter the cerebellum or propagate to the anterior or posterior regions of the brain as in the other methods. As shown in Figure 3.11, the CPT produced by the proposed method shows a strong connection to the precentral cortical label while in the other methods the CPT are connected to both precentral and postcentral cortical regions.

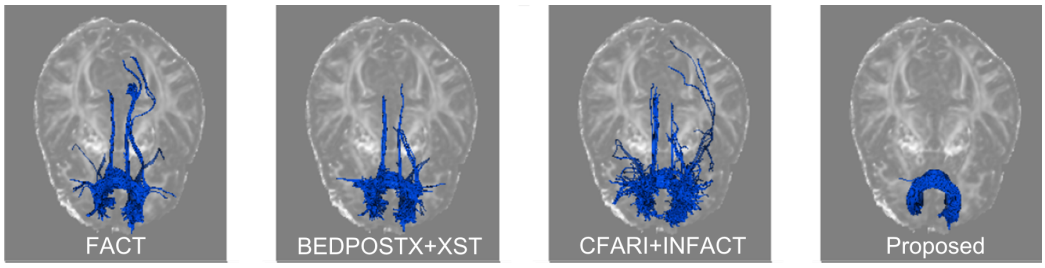

(a) CCF

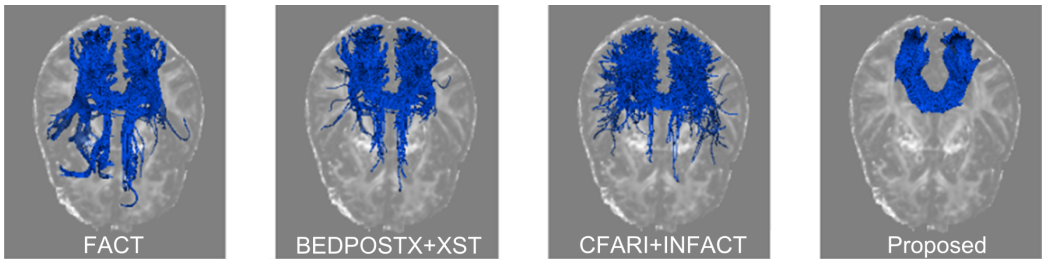

(b) CCP

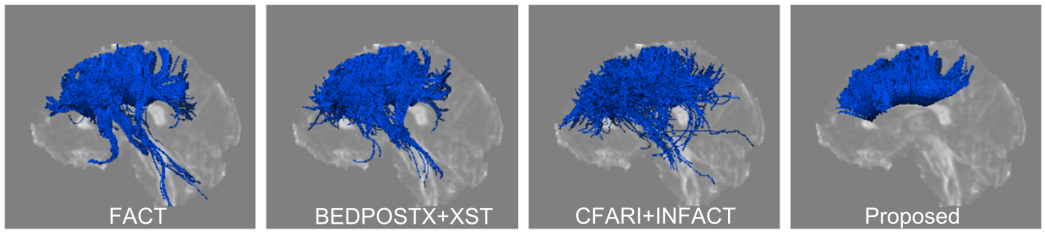

(c) CCS

Figure 3.8: Fiber tracking results overlaid on the FA map: (a) CCF, (b) CCP, and (c) CCS.

In Figure 3.12, which shows the OPR, the proposed method does not generate the false streamlines entering the CCP pathway and crossing the mid-sagittal plane. The connectivity map in Figure 3.13 also demonstrates that the false streamlines are reduced with the proposed method.

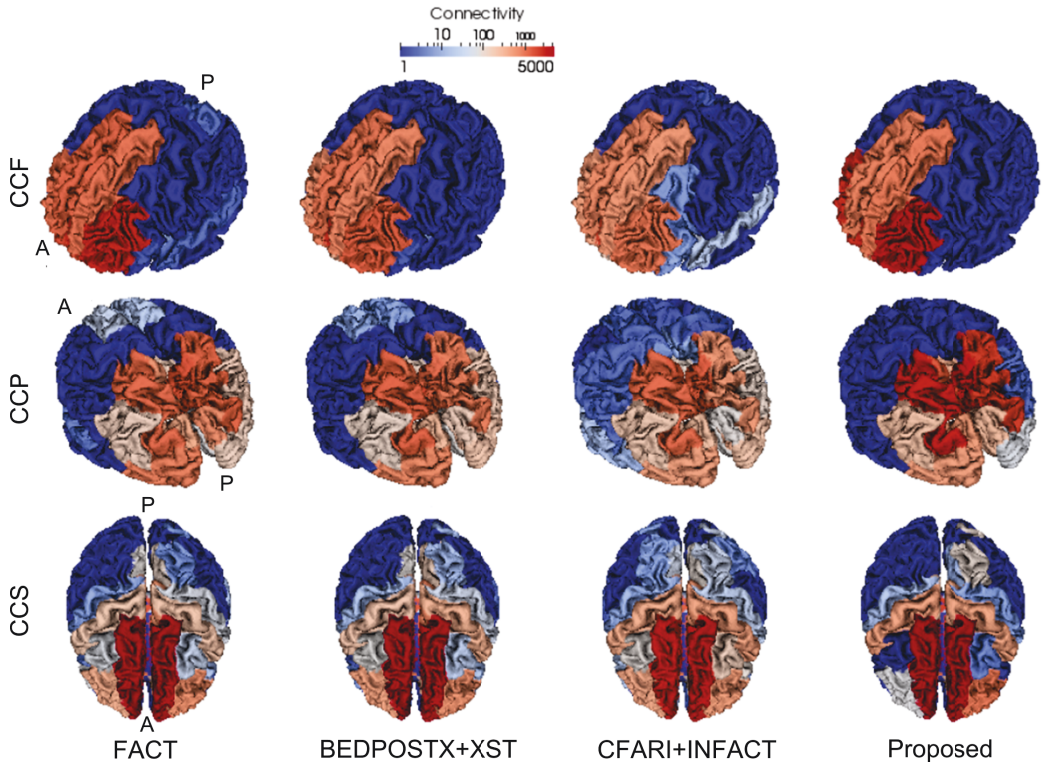

Figure 3.9: Connectivity to cortical labels: CCF, CCP, and CCS. The orientations are identified in the first column.

3.3.3.2 Connectivity Patterns in 18 Normal Subjects

Next, we studied the connectivity patterns of these tracts using the results of the proposed method on all 18 healthy subjects. To compare the counts of reconstructed streamlines across different subjects, we define a normalized connectivity for cortical label i:

$$C_i = \frac{N_i}{\sum_j N_j}, \tag{3.19}$$

where N_i is the number of streamlines hitting label i.

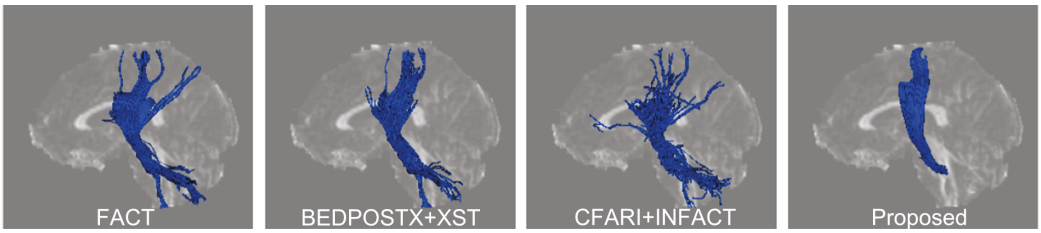

Figure 3.10: Fiber tracking results overlaid on the FA map: left CPT.

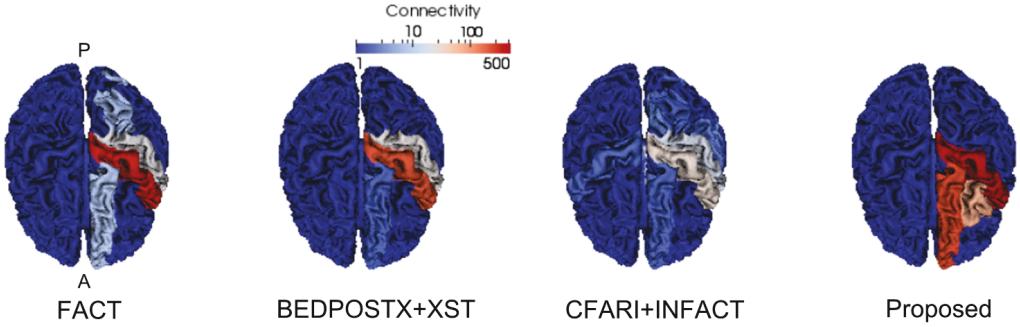

Figure 3.11: Connectivity to cortical labels: left CPT. The orientation is identified in the first column.

The matrices showing the connectivity of each tract to the cortical areas are shown in Figures 3.14, where the means, the standard deviations, and the medians of the normalized connectivity are plotted. Here "lh" and "rh" represent left and right hemispheres, respectively. It can be seen that no false connection across the hemisphere is created for the ATR, the PTR, and the STR. The ATR shows consistent connection to the lateral orbitofrontal area and the rostral middle frontal area. The PTR shows consistent connection to the inferior parietal area and the superior parietal area. The STR shows consistent connection to the postcentral area and the precentral area. The CCF is consistently connected to both left and right rostral anterior cingulate areas, rostral middle frontal areas, and superior frontal areas; the CCP is consistently con-

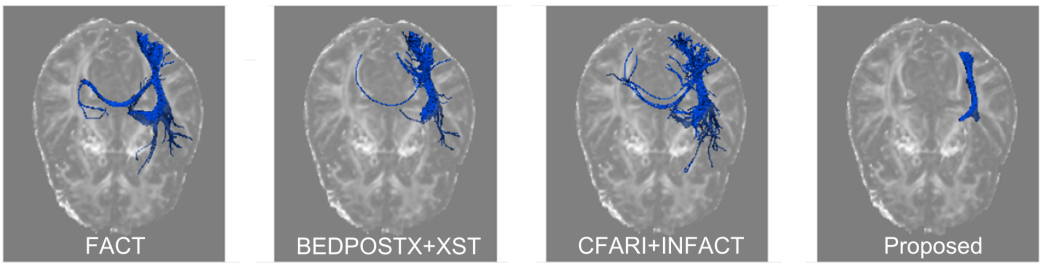

Figure 3.12: Fiber tracking results overlaid on the FA map: left OPR.

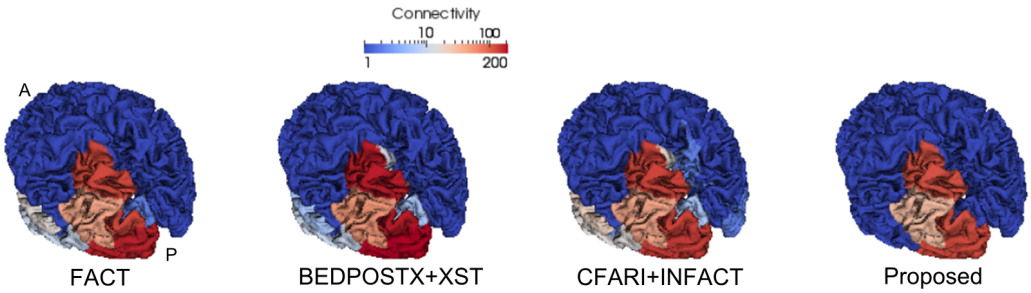

Figure 3.13: Connectivity to cortical labels: left OPR. The orientation is identified in the first column.

nected to both left and right isthmus cingulate areas, precuneus areas, and superior parietal areas; and the CCS is consistently connected to both left and right superior frontal areas. For the CPT and the OPR, no false connection across the hemisphere is created. The CPT is consistently connected to the precentral area, and the OPR is consistently connected to the fusiform and the lateral occipital area. It can also been observed that relatively higher standard deviations are associated with higher means and medians of the normalized connectivity.

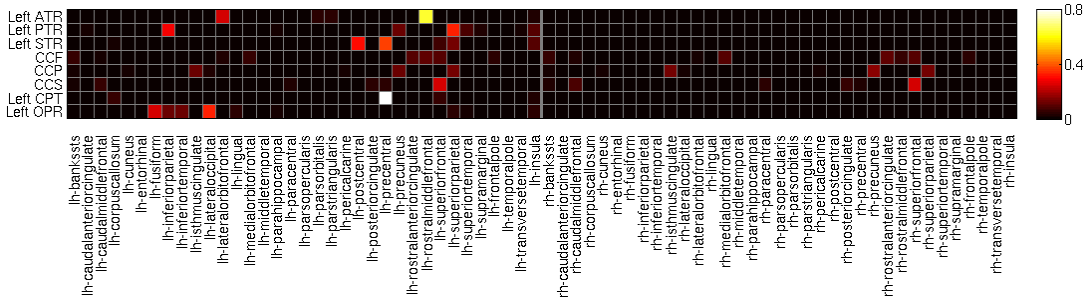

(a) Means of the normalized connectivity

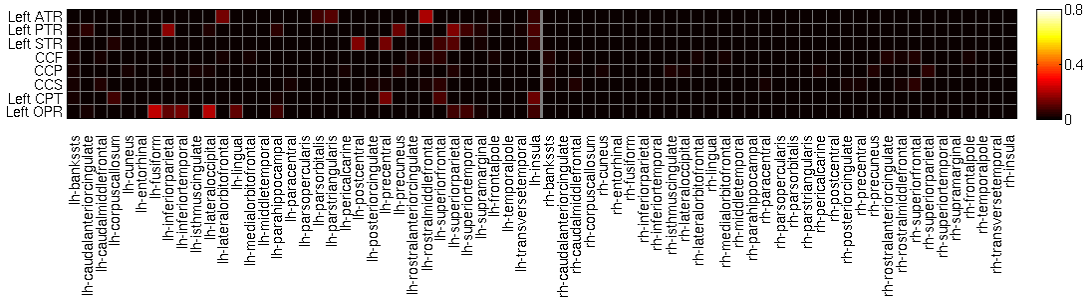

(b) Standard deviations of the normalized connectivity

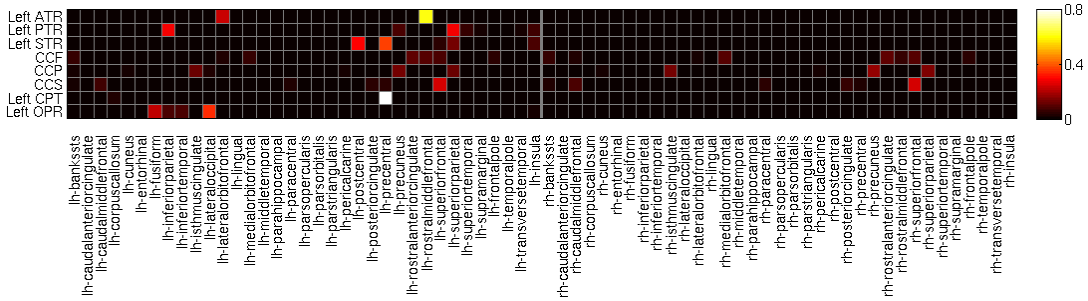

(c) Medians of the normalized connectivity

Figure 3.14: Normalized connectivity of each tract to the cortical areas: (a) mean, (b) standard deviation, and (c) median. "lh" and "rh" represent left and right hemispheres, respectively.

3.4 Discussion

The proposed method estimates the FOs within named white matter tracts using guidance from volumetric tract segmentation. There are limitations to the method. For example, its performance will be affected by the accuracy of the segmentation

algorithm. The weighting parameter μ_0 controls the influence of the segmentation. In our phantom test, because the ground truth is used, higher values of μ_0 lead to more accurate FO estimation. However, in practice, the segmentation method may result in various types of inaccuracy, which is difficult to simulate in the phantom test. Thus, the choice of μ_0 should be made with respect to the segmentation algorithm in a real application. A smaller value of μ_0 should be used with less accurate segmentation. The worst case scenario would be zero weighting ($\mu_0 = 0$) where the solution becomes a diffusion process of smoothing.

The choice of the smoothing parameter α can be dependent on the shape of the tract. In the phantom test, because the ground truth FOs are identical throughout the tract, higher α leads to a better estimate. However, if the tract is curved, α values that are too large will generate FOs not agreeing with the tract shape.

The FO estimation is also affected by the tract model that is used by the segmentation algorithm. For example, in the Fiber Cup phantom, the tracts could be defined differently. If the tract with three branches (the blue one in Figure 3.4) were defined as three separate tracts, the estimated FOs could become slightly different accordingly. In the brain DTI data, we do not estimate the FOs in the lateral parts of the corpus callosum, which propagate the streamlines to the lateral part of the brain, because the lateral corpus callosum is not included in the DOTS atlas (which is based on the tract atlas in [90]). Similarly, if another tract segmentation algorithm were to be used, the resulting FO estimates would follow the new tract definition.

In addition, if the method were to be applied on patients, the FO estimation results could be influenced by the presence of disease, because the segmentation performance could be affected.

We have used the streamline count as a measure of connectivity to demonstrate the performance of the proposed method. This also gives a potential scientific application of studying connectivity of tracts. It should be noted that, for scientific studies, the streamline count is not necessarily an accurate quantitative measure of strength of connectivity [110], which could also be a reason for the relatively large variations in normalized connectivity in Figure 3.14. Instead, the connectivity patterns provide a qualitative evaluation of connectivity [110].

3.5 Summary and Conclusion

We have proposed a Bayesian approach to FO estimation guided by volumetric tract segmentation. The prior information encodes spatial smoothness of the FOs and the constraint of volumetric tract segmentation, and the likelihood term ensures data fidelity. By maximizing the posterior probability density of FOs, an objective function is achieved. Using calculus of variations, the FO is estimated by iteratively solving the Euler-Lagrange equations. Then, a streamlining fiber tracking strategy using the estimated FOs is presented.

Experiments performed on a digital crossing phantom, the Fiber Cup phantom,

and brain DTI data demonstrate that the proposed method can reduce the effect of noise, resolve crossing fibers, and reduce anatomically incorrect streamlines. The experiments on tract connectivity to cortical regions also show the potential application of the proposed method to scientific studies.

3.A Derivation for the Iterative FO Update

Using the approximation in [101], we have

$$\begin{aligned} \nabla^2 f_x &= \overline{f_x} - f_x, \\ \nabla^2 f_y &= \overline{f_y} - f_y, \\ \nabla^2 f_z &= \overline{f_z} - f_z, \end{aligned} \tag{3.20}$$

where $\overline{f_x}$, $\overline{f_y}$, and $\overline{f_z}$ are the local averages of f_x, f_y, and f_z, respectively. Using Eq. (3.20), Eq. (3.16) can be written as

$$\begin{aligned} \alpha(\overline{f_x} - f_x) &= \mu g_x(f_x g_x + f_y g_y + f_z g_z) + \lambda(f_x - v_x), \\ \alpha(\overline{f_y} - f_y) &= \mu g_y(f_x g_x + f_y g_y + f_z g_z) + \lambda(f_y - v_y), \\ \alpha(\overline{f_z} - f_z) &= \mu g_z(f_x g_x + f_y g_y + f_z g_z) + \lambda(f_z - v_z). \end{aligned} \tag{3.21}$$

Solving Eq. (3.21), we have:

$$
\begin{aligned}
f_x = &\overline{f_x} - \frac{\mu g_x(g_x\overline{f_x} + g_y\overline{f_y} + g_z\overline{f_z})}{\alpha+\lambda+\mu(g_x^2+g_y^2+g_z^2)} + \\
&\frac{\lambda[(\alpha+\lambda)(v_x-\overline{f_x}) + \mu(g_y^2+g_z^2)(v_x-\overline{f_x}) - \mu g_x g_y(v_y-\overline{f_y}) - \mu g_x g_z(v_z-\overline{f_z})]}{(\alpha+\lambda)(\alpha+\lambda+\mu(g_x^2+g_y^2+g_z^2))}, \\
f_y = &\overline{f_y} - \frac{\mu g_y(g_x\overline{f_x} + g_y\overline{f_y} + g_z\overline{f_z})}{\alpha+\lambda+\mu(g_x^2+g_y^2+g_z^2)} + \\
&\frac{\lambda[(\alpha+\lambda)(v_y-\overline{f_y}) - \mu g_x g_y(v_x-\overline{f_x}) + \mu(g_x^2+g_z^2)(v_y-\overline{f_y}) - \mu g_y g_z(v_z-\overline{f_z})]}{(\alpha+\lambda)(\alpha+\lambda+\mu(g_x^2+g_y^2+g_z^2))}, \\
f_z = &\overline{f_z} - \frac{\mu g_z(g_x\overline{f_x} + g_y\overline{f_y} + g_z\overline{f_z})}{\alpha+\lambda+\mu(g_x^2+g_y^2+g_z^2)} + \\
&\frac{\lambda[(\alpha+\lambda)(v_z-\overline{f_z}) - \mu g_x g_z(v_x-\overline{f_x}) - \mu g_y g_z(v_y-\overline{f_y}) + \mu(g_x^2+g_y^2)(v_z-\overline{f_z})]}{(\alpha+\lambda)(\alpha+\lambda+\mu(g_x^2+g_y^2+g_z^2))}.
\end{aligned}
\tag{3.22}
$$

Then the problem is solved by iteratively updating $\boldsymbol{f}$, which leads to Eq. (3.17).

Chapter 4

Distinguishing Interdigitated Tongue Muscles with Limited DTI

4.1 Motivation

Several studies have used diffusion tensor imaging (DTI) to study tongue muscles [40,92–94,113,114]. For example, in [93], based on diffusion tensors, fiber tracking was used to reconstruct key muscle fibers and visualize the tongue anatomy. In [94], muscle fibers were studied together with strain rate to demonstrate the relationship between fiber organization and tissue deformation during swallowing. Using DTI, studies on the influence of interventions on the tongue muscles have also been performed. In [92] and [114], preliminary studies were carried out to track the deformed muscle fibers in patients with oral appliances. In [113], tongue muscle fibers were

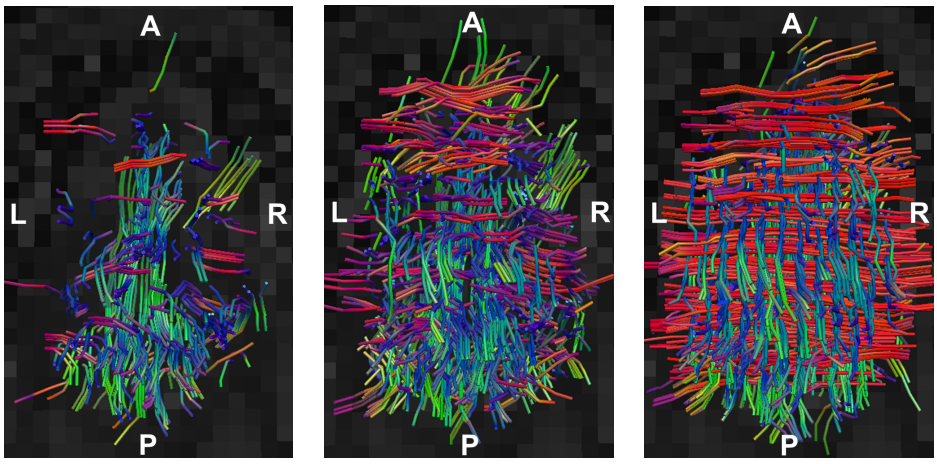

(a) (b) (c)

Figure 4.1: An example of fiber tracking seeded in the transverse muscle, which in this axial view should be seen as left to right (red) streamlines. Each segment of the fibers is color-coded by the standard DTI color scheme. (a) DTI model. (b) Multi-tensor model. (c) Proposed method with prior information.

tracked for a patient after the glossectomy and compared with a control subject.

These studies [92–94, 113, 114] all used DTI-based fiber tracking [3, 115]. However, many of the tongue muscles interdigitate, and it is well known that DTI cannot represent crossing fiber orientations (FOs) [116]. Thus, using the tensor model is insufficient for reconstructing interdigitated tongue muscles. For example, the transverse muscle interdigitates with the genioglossus, and DTI fails to reconstruct the transverse muscle. Figure 4.1(a) gives a typical example of fibers tracked with DTI when seeded in the transverse muscle; it can be seen that the majority of the transverse muscle fibers, which should be reconstructed as left to right (red) streamlines, are missing. Therefore, a fiber tracking method that is able to resolve crossing fibers is crucial for correct representation of the tongue muscles.

To address the problem of tracking crossing fibers, different imaging modalities that seek to obtain more comprehensive directional information, including high angular resolution diffusion imaging (HARDI) [60] and diffusion spectrum imaging (DSI) [61], have been proposed. Since these modalities typically acquire around or even more than 100 gradient directions and demand long scan times (which limits their application in clinical research), a number of attempts to accelerate the imaging process have been made [117–119]. However, because of the involuntary swallowing, which limits the available time to around 2–3 minutes for *in vivo* acquisition in the tongue, especially in cases where pathology is present, only a dozen (or so) gradient directions are achievable in practice. Thus, there is insufficient time for the acquisition of HARDI and DSI, despite the efforts to accelerate image acquisition. In addition, a great number of existing DTI data sets have been acquired and need better analysis. Therefore, although both HARDI and DSI data could be used for the methods described in this work, we limit the presentation of results to the conventional DTI acquisitions that are presently achievable.

There are also methods designed to better exploit the information in DTI to resolve crossing fibers. For example, Behrens et al. [26] and Peled et al. [55] use two-tensor models to recover crossing directions. In [26], a Bayesian estimation is used to fit the parameters of the model, which is achieved by Markov chain Monte Carlo sampling. The method in [55] places a number of constraints on the tensors in the two-tensor model to reduce the number of free parameters, and resolves two crossing

FOs using a nonlinear least squares method. Several prior research studies [27, 56, 58] use multi-tensor models with a fixed tensor basis to resolve crossing fibers. In [58], diffusion signals are modeled as a discrete mixture of Gaussian random variables and are deconvolved using a set of diffusion basis functions which represent FOs. In [27], a sparse reconstruction technique is used, where a dictionary is constructed with a fixed tensor basis. The FOs are estimated by solving the ℓ_1-norm regularized least squares problem. Zhou et al. [56] add an isotropic component in the multi-tensor model and solves the problem with ℓ_1-norm and TV-norm regularization.

Using the number of gradient directions that is common in clinical research (around 30), the two-tensor or multi-tensor models are able to resolve crossing fibers. However, due to the limited number of gradient directions in *in vivo* tongue diffusion data acquisition, there is insufficient information for successful resolution of crossing fibers using these methods. Figure 4.1(b) gives an example of fibers tracked using the multi-tensor model in [27], when the fibers were seeded in the transverse muscle. Although part of the transverse muscle is reconstructed, it is clear that the major body is missing. Thus, distinguishing interdigitated tongue muscles, which constitute a large percentage of the tongue volume, is very challenging.

In this work, we present a multi-tensor method for distinguishing interdigitated tongue muscles that incorporates prior directional knowledge within a Bayesian framework. The proposed method is named Fiber Interdigitation Estimation by Bayesian Reconstruction (FIEBR). In FIEBR, the prior directional knowledge provides infor-

mation on likely FOs at each voxel, and can be computed with anatomical knowledge of tongue muscles.

An example of the FIEBR result is shown in Figure 4.1(c). In contrast to the DTI model and the multi-tensor results in Figures 4.1(a) and 4.1(b), FIEBR successfully reconstructs the transverse muscle. In FIEBR, we use a fixed tensor basis to model the diffusion weighted signals in each voxel, and then we determine the contribution of each basis tensor using maximum a posteriori (MAP) estimation. The prior distribution contains both the prior directional information and sparsity constraints, and data fidelity is modeled in the likelihood term. The resulting objective function can be solved as a noise-aware version of a weighted ℓ_1-norm minimization [120]. Using the estimated FOs from FIEBR, we also propose a streamlining fiber tracking strategy to reconstruct tongue muscles.

4.2 Theory and Algorithm

In this section, we first introduce a multi-tensor model with a fixed tensor basis. Then, the MAP estimation of the FOs incorporating prior directional knowledge is presented, and an approach to obtaining prior knowledge of tongue muscle FOs is provided. A streamlining fiber tracking strategy using the estimated FOs is also described. Finally, the constants used in the proposed FIEBR and streamlining algorithms are summarized.

4.2.1 Multi-tensor Model with a Fixed Tensor Basis

We define a fixed tensor basis comprising N prolate tensors $\mathbf{D}_i$ whose primary eigenvectors (PEVs) are oriented over the sphere. Each $\mathbf{D}_i$ represents an FO given by its PEV. In this work, $N = 253$, the second and third eigenvalues of each basis tensor are equal to 0.5×10^{-3} mm^2/s, and the primary eigenvalue is equal to 2×10^{-3} mm^2/s. At each voxel, the diffusion weighted signals can be modeled as a mixture of the attenuated signals from these tensors. Using the Stejskal-Tanner tensor formulation [30], we have [27]

$$S_k = S_0 \sum_{i=1}^{N} f_i e^{-b\boldsymbol{g}_k^T \mathbf{D}_i \boldsymbol{g}_k} + n_k, \tag{4.1}$$

where b is the b-value, $\boldsymbol{g}_k$ is the k-th gradient direction ($k \in \{1, 2, ..., K\}$ where K is the number of gradient directions), S_k is the diffusion signal in the k-th direction, S_0 is the baseline signal without diffusion weighting, f_i is the (unknown) nonnegative mixture fraction for $\mathbf{D}_i$, and n_k is a noise term. Note that in this signal model, as in [58], [121], and [27], we do not explicitly require $\sum_{i=1}^{N} f_i = 1$, but the f_i's can be interpreted as mixture fractions when they are normalized to sum to one [27]. By defining $y_k = S_k/S_0$ and $\eta_k = n_k/S_0$, Eq. (4.1) can be written as:

$$\boldsymbol{y} = \mathbf{G}\boldsymbol{f} + \boldsymbol{\eta}, \tag{4.2}$$

where $\boldsymbol{y} = (y_1, y_2, ..., y_K)^T$, $\mathbf{G}$ is a $K \times N$ matrix comprising the attenuation terms $G_{ki} = e^{-b\boldsymbol{g}_k^T \mathbf{D}_i \boldsymbol{g}_k}$, $\boldsymbol{f} = (f_1, f_2, ..., f_N)^T$, and $\boldsymbol{\eta} = (\eta_1, \eta_2, ..., \eta_K)^T$.

4.2.2 Mixture Fraction Estimation with Prior Knowledge

We use MAP estimation to estimate the mixture fractions $\boldsymbol{f}$. Accordingly, we seek to maximize the posterior probability of $\boldsymbol{f}$ given the observations $\boldsymbol{y}$. The posterior probability is given by

$$p(\boldsymbol{f}|\boldsymbol{y}) = \frac{p(\boldsymbol{f})p(\boldsymbol{y}|\boldsymbol{f})}{\int p(\boldsymbol{f})p(\boldsymbol{y}|\boldsymbol{f})\mathrm{d}\boldsymbol{f}}. \tag{4.3}$$

Therefore, since the denominator in Eq. (4.3) is constant with respect to $\boldsymbol{f}$, the desired solution is

$$\hat{\boldsymbol{f}} = \arg\max_{\boldsymbol{f}} p(\boldsymbol{f})p(\boldsymbol{y}|\boldsymbol{f}) \tag{4.4}$$

Since at each voxel the number of FOs is expected to be small, we promote sparseness in $\boldsymbol{f}$ by using the Laplace prior density: $p(\boldsymbol{f}) \propto e^{-\lambda||\boldsymbol{f}||_1}$, where λ is a positive constant. However, sparsity alone is not sufficient prior information when the observations do not include a large number of gradient directions (as in DTI of the *in vivo* tongue). Therefore, we further supplement the prior knowledge with directional information. Suppose prior information about likely FOs were known at each voxel.

For each voxel, let the prior directions be represented by the collection of vectors $\{\boldsymbol{w}_1, \boldsymbol{w}_2, ..., \boldsymbol{w}_P\}$, where P is the number of prior FOs. A similarity vector $\boldsymbol{a}$ can be constructed between the directions represented by the basis tensors and the prior directions:

$$\boldsymbol{a} = (\max_m |\boldsymbol{v}_1 \cdot \boldsymbol{w}_m|, \max_m |\boldsymbol{v}_2 \cdot \boldsymbol{w}_m|, ..., \max_m |\boldsymbol{v}_N \cdot \boldsymbol{w}_m|)^T, \tag{4.5}$$

where $\boldsymbol{v}_i$ is the PEV of the basis tensor $\mathbf{D}_i$. Each entry a_i in $\boldsymbol{a}$ represents the similarity between the basis direction $\boldsymbol{v}_i$ and its closest prior direction. Note that $\boldsymbol{w}_m$ and $\boldsymbol{v}_i$ are unit vectors and thus $a_i \in [0, 1]$. We modify the prior density by incorporating the similarity vector as follows: $p(\boldsymbol{f}) \propto e^{-\lambda||\boldsymbol{f}||_1} e^{\gamma \boldsymbol{a} \cdot \boldsymbol{f}}$, where γ is a nonnegative constant. In this way, basis tensors closer to the prior directions are made to be more likely *a priori* (except when $\gamma = 0$ and no prior information is incorporated).

Since $\boldsymbol{f} \geq \mathbf{0}$, we have

$$\begin{aligned} \lambda||\boldsymbol{f}||_1 - \gamma \boldsymbol{a} \cdot \boldsymbol{f} &= \lambda \mathbf{1} \cdot \boldsymbol{f} - \gamma \boldsymbol{a} \cdot \boldsymbol{f} \\ &= \lambda(\mathbf{1} - \frac{\gamma}{\lambda}\boldsymbol{a}) \cdot \boldsymbol{f} \\ &= \lambda(\mathbf{1} - \alpha \boldsymbol{a}) \cdot \boldsymbol{f} \\ &= \lambda||\mathbf{C}\boldsymbol{f}||_1, \end{aligned} \tag{4.6}$$

where

$$\alpha = \frac{\gamma}{\lambda} \tag{4.7}$$

and $\mathbf{C}$ is a diagonal matrix with $C_{ii} = (1 - \alpha a_i)$ (note that $\alpha \geq 0$). Therefore, $p(\boldsymbol{f})$ has a truncated Laplace density given by

$$p(\boldsymbol{f}) = \frac{1}{Z_{\mathrm{p}}(\alpha, \lambda)} e^{-\lambda ||\mathbf{C}\boldsymbol{f}||_1}, \quad \boldsymbol{f} \geq \mathbf{0}, \tag{4.8}$$

where $Z_{\mathrm{p}}(\alpha, \lambda)$ is a normalization constant. We require $\alpha < 1$ to ensure that $C_{ii} > 0$. Thus, $0 \leq \alpha < 1$.

Suppose the noise $\boldsymbol{\eta}$ in Eq. (4.2) follows a Rician distribution. A Rician distribution can be approximated by a Gaussian distribution when the signal-to-noise ratio (SNR) is above 3:1 [122], which holds for most observed data in the proposed application. The conditional density for the observed data is then modeled as a Gaussian density: $p(\boldsymbol{y}|\boldsymbol{f}) \propto e^{-||\mathbf{G}\boldsymbol{f}-\boldsymbol{y}||_2^2/\sigma_\eta^2}$, where σ_η is the noise level.

Using Eq. (4.3), we can then write the posterior density as

$$p(\boldsymbol{f}|\boldsymbol{y}) = \frac{1}{Z(\alpha, \lambda, \sigma_\eta, \mathbf{G})} e^{-(||\mathbf{G}\boldsymbol{f}-\boldsymbol{y}||_2^2/\sigma_\eta^2 + \lambda||\mathbf{C}\boldsymbol{f}||_1)}, \tag{4.9}$$

where $Z(\alpha, \lambda, \sigma_\eta, \mathbf{G})$ is a normalization constant. The MAP estimate of $\boldsymbol{f}$ is found

by maximizing either $p(\boldsymbol{f}|\boldsymbol{y})$ or $\ln p(\boldsymbol{f}|\boldsymbol{y})$, which implies that

$$\hat{\boldsymbol{f}} = \underset{\boldsymbol{f}\geq\mathbf{0}}{\arg\min} \frac{1}{\sigma_\eta^2}||\mathbf{G}\boldsymbol{f} - \boldsymbol{y}||_2^2 + \lambda||\mathbf{C}\boldsymbol{f}||_1. \tag{4.10}$$

By using $\beta = \lambda\sigma_\eta^2$, the minimization in Eq. (4.10) is equivalent to

$$\hat{\boldsymbol{f}} = \underset{\boldsymbol{f}\geq\mathbf{0}}{\arg\min} ||\mathbf{G}\boldsymbol{f} - \boldsymbol{y}||_2^2 + \beta||\mathbf{C}\boldsymbol{f}||_1, \tag{4.11}$$

which is a noise-aware version of a weighted ℓ_1-norm minimization [120]. We note that this formulation is equivalent to the CFARI objective function developed in [27] when $\alpha = 0$ (i.e., $\mathbf{C} = \mathbf{I}$). Thus, our approach, developed with an alternative Bayesian perspective, is a generalization of the CFARI algorithm.

To solve Eq. (4.11), we use a new variable $\boldsymbol{g} = \mathbf{C}\boldsymbol{f}$. Since $\mathbf{C}$ is diagonal and $C_{ii} > 0$, $\mathbf{C}$ is invertible and therefore $\boldsymbol{f} = \mathbf{C}^{-1}\boldsymbol{g}$. Letting $\tilde{\mathbf{G}} = \mathbf{G}\mathbf{C}^{-1}$, we have

$$\hat{\boldsymbol{g}} = \underset{\boldsymbol{g}\geq\mathbf{0}}{\arg\min} ||\tilde{\mathbf{G}}\boldsymbol{g} - \boldsymbol{y}||_2^2 + \beta||\boldsymbol{g}||_1. \tag{4.12}$$

We find $\hat{\boldsymbol{g}}$ using the optimization method in [123] and the mixture fractions $\boldsymbol{f}$ can be estimated as:

$$\hat{\boldsymbol{f}} = \mathbf{C}^{-1}\hat{\boldsymbol{g}}. \tag{4.13}$$

Finally, the mixture fractions are normalized so that they sum to one:

$$\tilde{f}_i = \frac{\hat{f}_i}{\sum_{j=1}^{N} \hat{f}_j}. \tag{4.14}$$

Directions associated with nonzero mixture fractions are interpreted as FOs, and the value of $\tilde{f}_i$ indicates the contribution of the corresponding direction in the diffusion signal.

4.2.3 Prior Directions for the Tongue Muscles

To obtain prior directions, we built a template by manually identifying regions of interest (ROIs) for the genioglossus (GG) muscles, the geniohyoid (GH) muscles, the inferior longitudinal (IL) muscles, the superior longitudinal (SL) muscles, the transverse (T) muscles, and the vertical (V) muscles according to [96] on a high resolution structural image (0.8 mm isotropic) of a subject. The $b0$ image (the image without diffusion weighting) was also acquired for this template subject in the same position as the high resolution structural image. A mask of the tongue area was delineated on the $b0$ image. The muscle ROIs were subsampled to have the same resolution as the $b0$ image. For each test subject, a manual mask of the tongue was drawn on the $b0$ image. We used SyN deformable registration [124] between the $b0$ images masked by the tongue regions to deform the template to the target space, where cross correlation was used as the similarity metric.

Using deformed ROIs of the tracts, the prior directions can be obtained as follows. GG is known to be fan-shaped; therefore, we use fan-shaped prior directions for GG, as illustrated in Figure 4.2(a). Specifically, the origin of GG in the mid-sagittal slice can be identified on the test subject during the delineation of the whole tongue. Suppose the x-axis represents the left-right (L-R) direction, the y-axis represents the anterior-posterior (A-P) direction, and the z-axis represents the inferior-superior (I-S) direction. Then at a voxel $\boldsymbol{x}_{\mathrm{GG}} = (x_{\mathrm{GG}}, y_{\mathrm{GG}}, z_{\mathrm{GG}})$ belonging to GG, fanning GG prior directions can be obtained with respect to the GG origin $(x_{\mathrm{o}}, y_{\mathrm{o}}, z_{\mathrm{o}})$ as $\boldsymbol{w}_{\mathrm{GG}} = (0, y_{\mathrm{GG}} - y_{\mathrm{o}}, z_{\mathrm{GG}} - z_{\mathrm{o}})$. Similarly, since V is known to fan out like GG, for a voxel $\boldsymbol{x}_{\mathrm{V}} = (x_{\mathrm{V}}, y_{\mathrm{V}}, z_{\mathrm{V}})$ in V, its prior FO is set as $\boldsymbol{w}_{\mathrm{V}} = (0, y_{\mathrm{V}} - y_{\mathrm{o}}, z_{\mathrm{V}} - z_{\mathrm{o}})$. The GH and IL have A-P FOs, therefore in GH and IL voxels we use $\boldsymbol{w}_{\mathrm{GH}} = \boldsymbol{w}_{\mathrm{IL}} = (0, 1, 0)$ as the prior directions. The fibers in T propagate transversely, therefore the prior direction $\boldsymbol{w}_{\mathrm{T}}$ of a T voxel is $\boldsymbol{w}_{\mathrm{T}} = (1, 0, 0)$. Finally, SL has arc-shaped fibers close to the top and back surface of the tongue, as illustrated in Figure 4.2(a). The approximate circle center for the arc in the mid-sagittal slice is manually identified on the test subject as $\boldsymbol{x}_{\mathrm{c}} = (x_{\mathrm{c}}, y_{\mathrm{c}}, z_{\mathrm{c}})$. For a voxel $\boldsymbol{x}_{\mathrm{SL}} = (x_{\mathrm{SL}}, y_{\mathrm{SL}}, z_{\mathrm{SL}})$ belonging to SL, its prior direction can be calculated as $\boldsymbol{w}_{\mathrm{SL}} = (0, -(z_{\mathrm{SL}} - z_{\mathrm{c}}), y_{\mathrm{SL}} - y_{\mathrm{c}})$, which is tangential to the arc. An example of the prior directions on a test subject is shown in Figure 4.2(b). The directions are color-coded by the standard DTI scheme. Note that in the coronal view, the A-P directions (GH and IL) are not visible, and in the sagittal view, the L-R directions (T) are not visible.

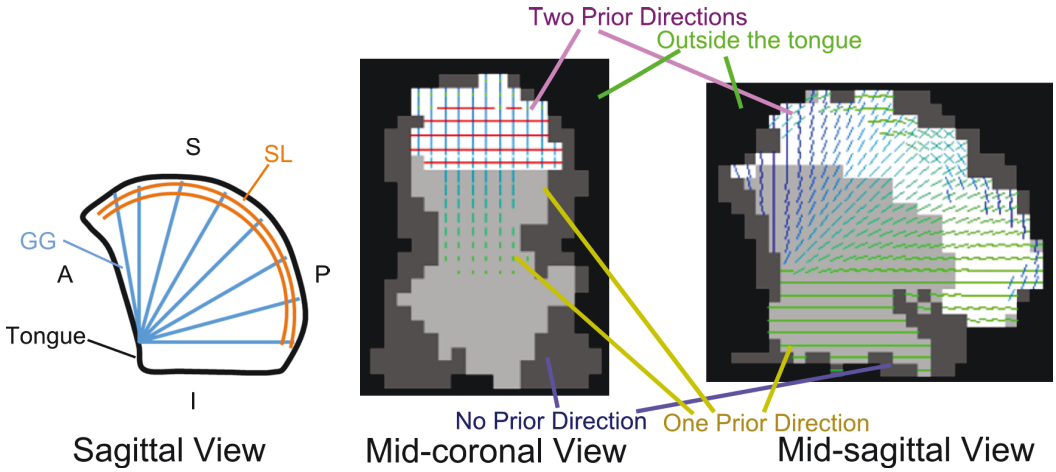

(a) Schematic of GG and SL (b) Prior FOs on a test subject

Figure 4.2: (a) A schematic of GG and SL FOs (sagittal view). (b) An example of prior directions on a test subject in the mid-coronal view and mid-sagittal view. The directions are color-coded by the standard DTI scheme. Note that in the coronal view, A-P directions (GH and IL) are not visible, and in the sagittal view, L-R directions (T) are not visible.

It is possible that the prescribed knowledge is incorrect due to an anatomical abnormality or error in its specification. Some variation is to be expected and can be compensated by selecting the weight assigned to the prior knowledge appropriately (see experiments below). However, when the prior knowledge varies grossly from the data, it is best to recognize this and adaptively downweight or remove this particular prior knowledge. For example, when there is one FO ($P = 1$), the priors should not deviate much from that FO; when there are two FOs ($P = 2$), the prior directions should be close to the plane defined by the two FOs, or in other words they are close to orthogonal to the normal of the plane.

One way of removing incorrect priors is to use the diffusion tensor information, which is calculated from the diffusion weighted images (DWIs). Suppose the first and

third eigenvectors of the diffusion tensor are $\boldsymbol{v}_{\mathrm{d1}}$ and $\boldsymbol{v}_{\mathrm{d3}}$, respectively; $\boldsymbol{v}_{\mathrm{d1}}$ provides an estimate of the FO when there is no crossing fiber, and $\boldsymbol{v}_{\mathrm{d3}}$ provides an estimate of the normal of the plane defined by the FOs when there are two crossing fibers. Accordingly, we discard prior FOs when

$$\arccos |\boldsymbol{w}_1 \cdot \boldsymbol{v}_{\mathrm{d1}}| > \xi_1, \text{ if } P = 1 \tag{4.15}$$

or

$$\min_{m=\{1,2\}} \arccos |\boldsymbol{w}_m \cdot \boldsymbol{v}_{\mathrm{d3}}| < \xi_2, \text{ if } P = 2, \tag{4.16}$$

where ξ_1 and ξ_2 are thresholds.

4.2.4 Fiber Tracking

Given the FIEBR estimated FOs, fiber tracking can be carried out using a streamlining technique similar to [27]. Starting from a seed voxel, the FOs with $\tilde{f}_i > t_{\mathrm{mf}}$ are used to initiate fibers, where t_{mf} is a threshold, because directions with small $\tilde{f}_i$'s are interpreted as components of isotropic diffusion. For each initiated fiber, at each step, one of the FOs in the current voxel is selected as the propagation direction until the fiber reaches the next voxel. In selecting FOs, only those with $\tilde{f}_i > t_{\mathrm{mf}}$ are considered. As in [27], the FO that maximizes the importance weighting $\tilde{f}_i |\boldsymbol{v}_i \cdot \boldsymbol{v}_{\mathrm{last}}|^4$ is selected.

Table 4.1: A summary of the constants used in the proposed method.

	Constants	Default Values
Mixture Fraction Estimation	α	N/A
	β	N/A
	ξ_1	$\pi/4$
	ξ_2	$\pi/4$
Fiber Tracking	t_{mf}	0.1
	t_{FA}	0.2
	θ_t	40°

Here $\boldsymbol{v}_{\text{last}}$ is the unit propagation direction in the previous tracking step. Starting and terminating criteria based on fractional anisotropy (FA) are used. Only voxels with FA larger than a threshold t_{FA} are used to initiate fibers, and when fibers reach FA values lower than t_{FA}, they are terminated. Finally, a turning angle threshold θ_{t} is used: when the angle between the current and previous propagation directions is larger than θ_{t}, the fibers are terminated. In this work, $t_{\text{mf}} = 0.1$, $t_{\text{FA}} = 0.2$, and $\theta_{\text{t}} = 40°$, which are common settings in other DTI fiber tracking algorithms [27, 102, 103].

4.2.5 Summary of Constants

A table summarizing the constants used in the proposed method is shown in Table 4.1. α, β, ξ_1, and ξ_2 are used in the mixture fraction estimation, and t_{mf}, t_{FA}, and θ_t are used in the fiber tracking process. Note that for α and β, different values are used based on the levels of noise in each voxel. Their values are determined in Section 4.3.1.3 and are not listed in Table 4.1.

4.3 Experiments

FIEBR was first applied on a digital crossing phantom. Different settings of α and β (see Eqs. (4.7) and (4.11)) were tested with different levels of noise. In addition, we studied the influence of the accuracy of prior knowledge. Parameters learned from these computational phantom studies were used on the next set of experiments involving *in vivo* tongue diffusion data, where three control subjects and three patients with glossectomies were included. FOs were estimated and muscle fibers were tracked on all six subjects. These results are visualized for qualitative comparison and histograms of FOs are numerically evaluated for quantitative comparison.

4.3.1 Digital Crossing Phantom

A 3D crossing phantom with two tracts crossing at 90° was generated to verify the operation of the FIEBR algorithm. Figure 4.3 shows an axial view of this computational phantom. Twelve diffusion gradient direction acquisitions were simulated and both FIEBR and CFARI [27] were applied to these data.

4.3.1.1 Noise-free Case

First we applied FIEBR on this noise-free phantom for a proof-of-concept experiment. The horizontal and vertical directions—i.e., the correct directions—were used as the prior directions for the horizontal and vertical tracts, respectively. A result

with $\alpha = 0.5$ and $\beta = 0.05$ is shown and compared with CFARI results ($\beta = 0.05$) in Figures 4.3(a) and 4.3(b). Here the standard DTI color scheme is used. Since directions with small $\tilde{f}_i$'s are interpreted as components of isotropic diffusion, we only show directions with $\tilde{f}_i > t_{\text{mf}}$. In the crossing regions, CFARI fails to produce the correct crossing directions (Figure 4.3(a)), while FIEBR correctly generates the crossing pattern (Figure 4.3(b)).

Next, we studied the performance of FIEBR with inaccurate prior directions. To introduce errors in the prior directions, we rotated the true directions by $\theta = 10^\circ$ and used the rotated directions as the prior directions. Two cases of rotations were tested: in and out of the axial plane. Specifically, in the first case the horizontal and vertical directions were both rotated clockwise in the axial plane; and in the second case the horizontal directions were rotated around the vertical line out of the axial plane and the vertical directions were rotated around the horizontal line out of the axial plane. The results of the two cases are shown in Figures 4.3(c) and 4.3(d). In both cases, even with inaccurate prior directions, FIEBR correctly estimates noncrossing and crossing FOs.

4.3.1.2 Influence of Noise, Algorithm Parameters, and Prior Direction Inaccuracies

To make the simulation more realistic, we added Rician noise in the phantom test. We selected three sample voxels in the phantom: one in the noncrossing hor-

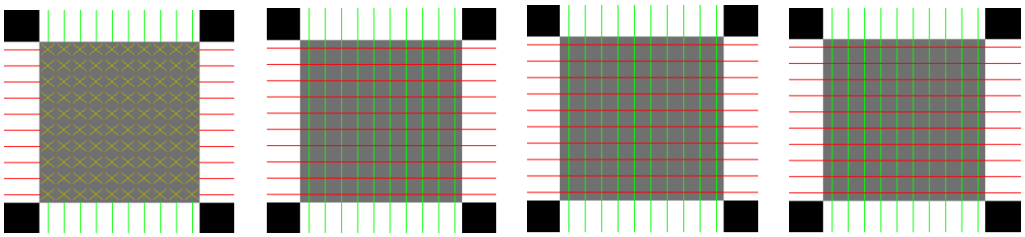

(a) (b) (c) (d)

Figure 4.3: Axial view of the FA of the crossing phantom. Estimated FOs from (a) CFARI and (b)-(d) FIEBR when (b) the prior directions are correct, (c) the prior directions are rotated by 10° in the plane, and (d) the prior directions are rotated by 10° out of the plane.

izontal tract, one in the noncrossing vertical tract, and one in the crossing region. Different levels σ_η of Rician noise $\boldsymbol{\eta}$ in Eq. (4.2) were added to the sample voxels, and we tested with different values of α, β, and prior direction inaccuracy θ. The inaccurate prior directions were obtained with in-plane and out-of-plane rotation by θ. The sets of the testing parameters were: $\sigma_\eta \in \Sigma_\eta = \{0, 0.04, 0.08, 0.12\}$, $\alpha \in A = \{0.1, 0.2, \ldots, 0.9, 0.99\}$, $\beta \in B = \{0.05, 0.2, 0.4, \ldots, 2.0\}$, and $\theta \in \Theta = \{0°, 10°, 20°, 30°\}$. For each combination of σ_η, α, β, and θ, 100 simulations were performed for each sample voxel.

To quantitatively evaluate the results, we define two error measures for angles:

$$e_1 = \frac{1}{N_1} \sum_{\substack{i=1 \\ \tilde{f}_i > t}}^{N} \min_j \arccos(\boldsymbol{v}_i \cdot \boldsymbol{u}_j) \cdot \frac{180°}{\pi}, \tag{4.17}$$

$$e_2 = \frac{1}{N_2} \sum_{j=1}^{N_2} \min_{i:\tilde{f}_i > t} \arccos(\boldsymbol{v}_i \cdot \boldsymbol{u}_j) \cdot \frac{180°}{\pi}. \tag{4.18}$$

Here N_1 is the number of directions with normalized mixture fractions $\tilde{f}_i$ larger than

a threshold t (in this case $t = 0.1$), $\boldsymbol{v}_i$ is the basis direction, $\boldsymbol{u}_j$ is the ground truth of FO, and N_2 is the number of ground truth directions. N_2 can be 1 or 2, depending on whether crossing fibers exist at the location. e_1 measures how close the estimated directions are to the ground truth, and e_2 measures how well each true direction is estimated. Note that using only e_1 or e_2 is insufficient because the estimated directions can agree with one of the true crossing directions and ignore the other, or each true direction can be properly estimated but there are other estimated directions representing incorrect directions.

Examples of the mean errors of the estimated FOs are plotted in Figures 4.4 and 4.5 for $\sigma = 0.04$, $\theta \in \{0°, 10°\}$, $\alpha \in A$, and $\beta \in B$. For the inaccurate prior directions rotated by θ, the results of the in-plane and out-of-plane cases are averaged. The results for the two noncrossing voxels are averaged as the noncrossing cases. Note that the cases with $\alpha = 0$ are equivalent to CFARI results.

Figure 4.4 shows examples when noise of $\sigma_\eta = 0.04$ is added to noncrossing voxels. Using the correct prior directions ($\theta = 0°$) reduces the effect of noise (see Figures 4.4(a) and 4.4(c)). When errors are introduced in the prior directions, the effect of noise can still be reduced with the proper selection of α and β (see $\alpha = 0.4$ and $\beta = 1.2$ in Figures 4.4(b) and 4.4(d)). Figure 4.5 gives examples of the crossing cases. It can be seen that the effect of noise can be reduced with true or inaccurate prior directions. Note that for $\theta = 10°$, the errors can be smaller than 10°, which indicates the result is better than simply using the prior directions as the estimate.

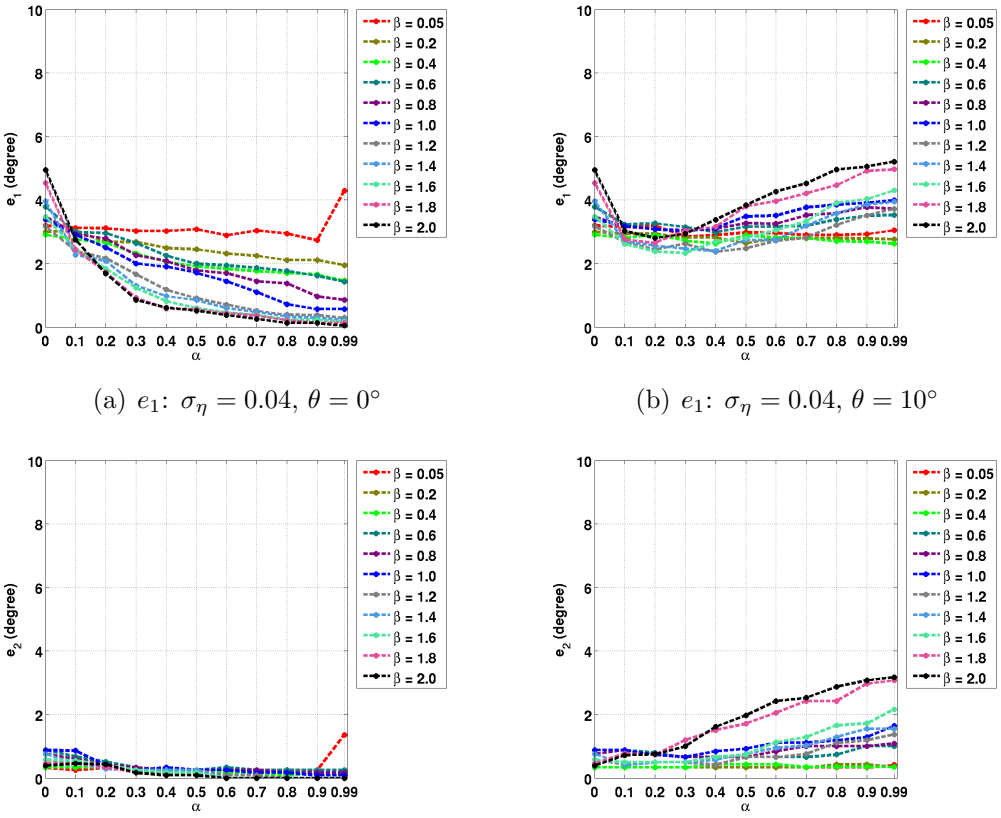

(a) e_1: $\sigma_\eta = 0.04$, $\theta = 0°$

(b) e_1: $\sigma_\eta = 0.04$, $\theta = 10°$

(c) e_2: $\sigma_\eta = 0.04$, $\theta = 0°$

(d) e_2: $\sigma_\eta = 0.04$, $\theta = 10°$

Figure 4.4: Mean e_1 and e_2 errors in the noncrossing cases with $\sigma_\eta = 0.04$ and different θ, α, and β.

4.3.1.3 Determination of Algorithm Parameters Based on Noise Levels

We used all the combinations of σ_η, α, β, and θ to determine the best parameter settings for real data. For each combination of σ_η, α, and β, we averaged the errors with different θ for the noncrossing and crossing cases separately. Then for each σ_η, the α and β which minimize the average error using all the θ were selected for the noncrossing and crossing cases. Using the plots in Figures 4.4 and 4.5 and other

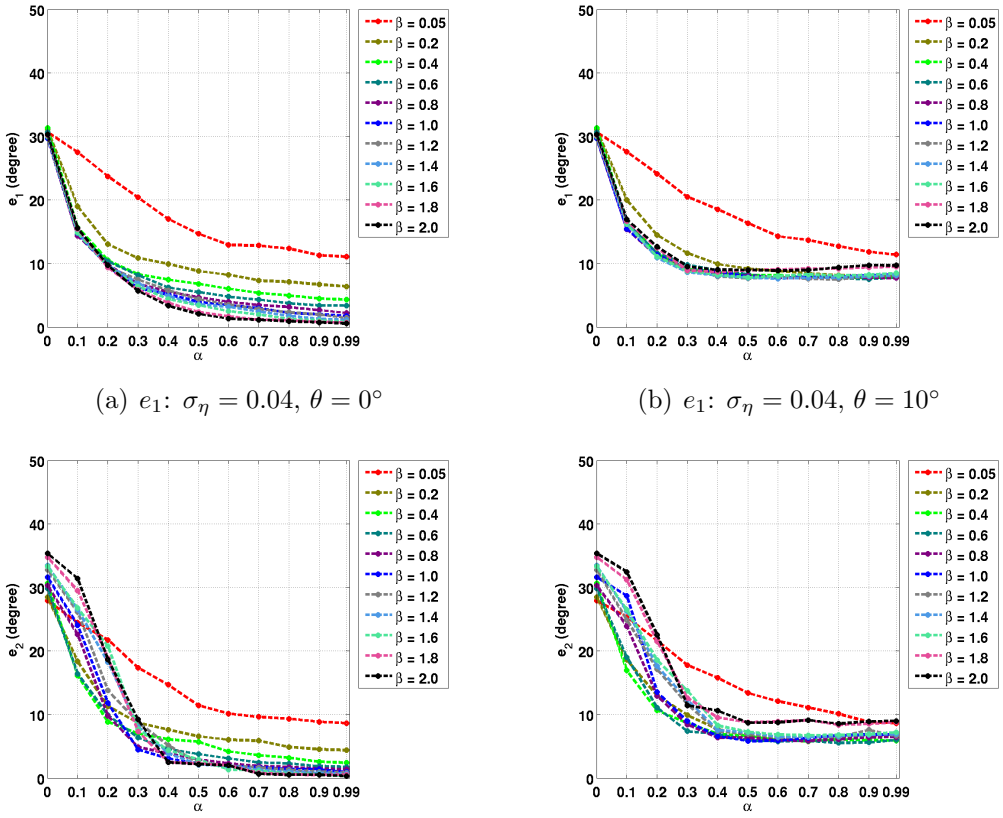

(a) e_1: $\sigma_\eta = 0.04$, $\theta = 0°$

(b) e_1: $\sigma_\eta = 0.04$, $\theta = 10°$

(c) e_2: $\sigma_\eta = 0.04$, $\theta = 0°$

(d) e_2: $\sigma_\eta = 0.04$, $\theta = 10°$

Figure 4.5: Mean e_1 and e_2 errors in the crossing cases with $\sigma_\eta = 0.04$ and different θ, α, and β.

similar plots not shown, the selection is summarized in Table 4.2. This table is later used to determine α and β in the real data application.

Based on Table 4.2, different α and β values are used for different levels of noise. To estimate the noise level σ_η, which is calculated by the image noise term in Eq. (4.1) and the $b0$ image intensity, we first estimate the image noise level σ by placing an ROI in the background. Here we assume the background noise follows a Rayleigh

Table 4.2: A summary of the selected α and β with different σ_η.

	Noncrossing Case				Crossing Case			
σ_η	0	0.04	0.08	0.12	0	0.04	0.08	0.12
α	0.5	0.4	0.5	0.5	0.5	0.7	0.8	0.6
β	0.2	0.6	1.0	1.6	0.2	0.6	1.0	1.6

distribution, and σ^2 can be estimated as [125]

$$\widehat{\sigma^2} \approx \frac{1}{2N_{\mathrm{b}}} \sum_{i=1}^{N_{\mathrm{b}}} I_i^2, \tag{4.19}$$

where I_i's are the intensities of the background voxels in the bounding box, and N_{b} is the number of these voxels. Then, σ is estimated as

$$\hat{\sigma} \approx \sqrt{\widehat{\sigma^2}}. \tag{4.20}$$

Thus, at each voxel x, $\sigma_\eta(x)$ can be estimated as

$$\hat{\sigma}_\eta(x) \approx \frac{\hat{\sigma}}{S_0(x)}, \tag{4.21}$$

where $S_0(x)$ is the baseline signal without diffusion weighting at x. Using the estimated $\hat{\sigma}_\eta(x)$ and Table 4.2, we decide $\alpha(x)$ and $\beta(x)$ for each voxel x as follows. In

noncrossing regions:

$$(\alpha(x), \beta(x)) = \begin{cases} (0.5, 0.2), & \text{if} \quad 0 \leq \hat{\sigma}_\eta(x) < 0.02 \\ (0.4, 0.6), & \text{if} \quad 0.02 \leq \hat{\sigma}_\eta(x) < 0.06 \\ (0.5, 1.0), & \text{if} \quad 0.06 \leq \hat{\sigma}_\eta(x) < 0.10 \\ (0.5, 1.6), & \text{if} \quad \hat{\sigma}_\eta(x) \geq 0.10 \end{cases} \tag{4.22}$$

In crossing regions:

$$(\alpha(x), \beta(x)) = \begin{cases} (0.5, 0.2), & \text{if} \quad 0 \leq \hat{\sigma}_\eta(x) < 0.02 \\ (0.7, 0.6), & \text{if} \quad 0.02 \leq \hat{\sigma}_\eta(x) < 0.06 \\ (0.8, 1.0), & \text{if} \quad 0.06 \leq \hat{\sigma}_\eta(x) < 0.10 \\ (0.6, 1.6), & \text{if} \quad \hat{\sigma}_\eta(x) \geq 0.10 \end{cases} \tag{4.23}$$

In this way, the selected parameter pairs minimize the average errors at their corresponding noise levels.

4.3.2 *In Vivo* Tongue Diffusion Data

We applied our method to *in vivo* tongue diffusion data, where three control subjects and three patients with glossectomies were included. DWIs were acquired on a 3T MR scanner (Magnetom Trio, Siemens Medical Solutions, Erlangen, Germany).

Each scan has 12 gradient directions and one $b0$ image. The b-value is 500 s/mm^2. The field of view (FOV) is 240 mm $\times$ 240 mm $\times$ 84 mm. TR/TE=5000/68 ms. The resolution is 3 mm isotropic. The acquisition of each subject took about two minutes and 30 seconds, which must be this short because it is difficult for subjects to resist for a longer time period the involuntary urge to swallow.

4.3.2.1 Application to Control Subjects

We first applied FIEBR on the control subjects using the parameter settings in Eqs. (4.22) and (4.23), which are computed independently for each voxel. An example of the estimated FOs on a representative control subject is shown and compared with the PEV of the diffusion tensor and the CFARI algorithm [27] in Figure 4.6. In the mid-sagittal view, we highlight the regions of GG crossing with SL, and in the mid-coronal view, a region of GG/V and T crossing is highlighted. The PEV alone obviously cannot represent crossing FOs and the CFARI algorithm fails to resolve crossing fibers, while FIEBR is able to recover the crossing directions.

In Figure 4.7, we plot the distribution of FOs in the whole tongue of this control subject for all three algorithms. The distributions are plotted on the upper part of the unit sphere and viewed from top. A sketch of the tongue orientation relative to these hemispheres is shown in Figure 4.7(a). The surface of the hemisphere is divided into bins by discretizing the azimuth angle and the elevation angle. In each bin, the density is calculated by dividing the number of the FOs that fall in the bin

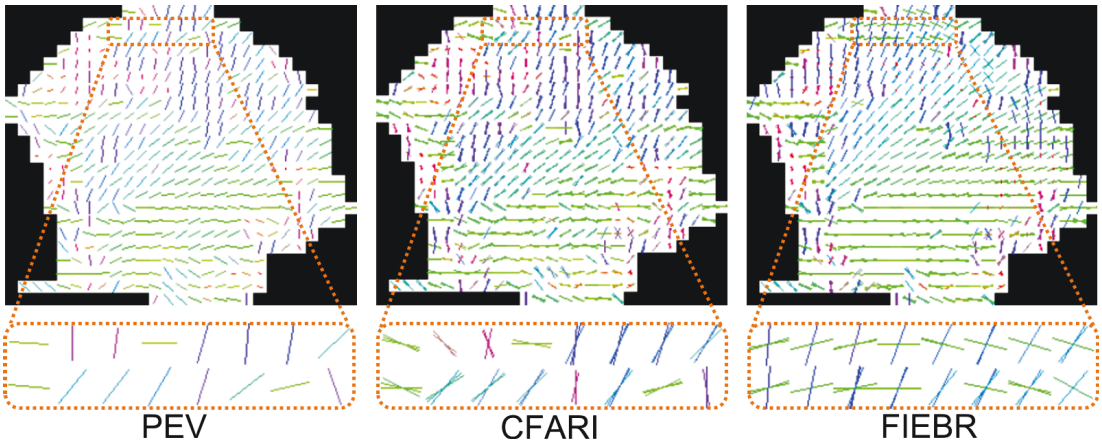

(a) Mid-sagittal View

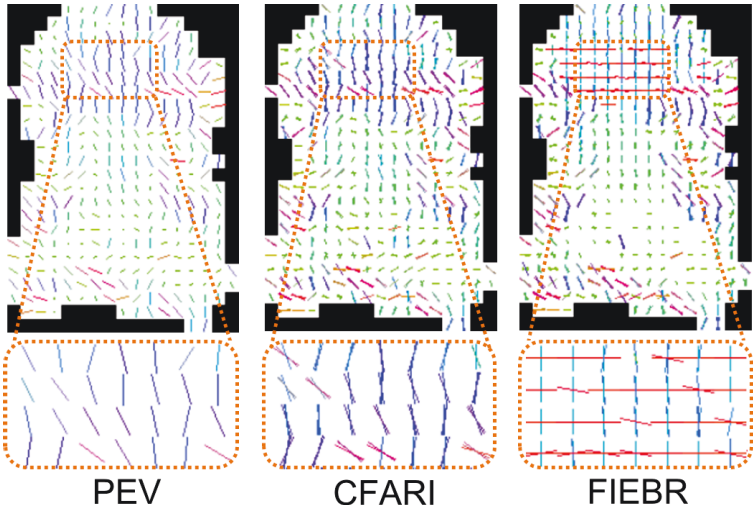

(b) Mid-coronal View

Figure 4.6: Estimated FOs from FIEBR compared with the PEV and the CFARI algorithm: (a) mid-sagittal view and (b) mid-coronal view. Note the highlighted regions for comparison.

by the bin area. In the FIEBR result, there are many L-R FOs, which are indicated by the bins near $(-1, 0)$ and $(1, 0)$ (highlighted as region A in Figure 4.7(d)). The L-R directions represent the T FOs. There are also many FOs in the A-P direction, which are indicated by the bin near $(0, -1)$ (highlighted as region B in Figure 4.7(d)). These directions represent the IL, GH, and part of GG fibers. The three bins on the

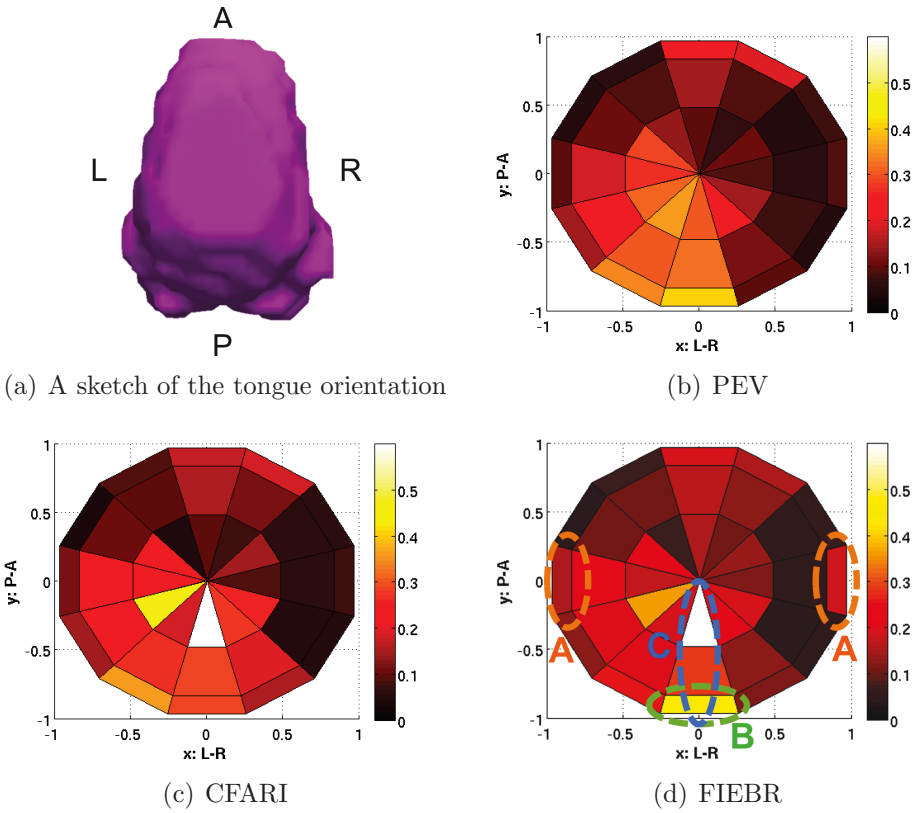

(a) A sketch of the tongue orientation (b) PEV

(c) CFARI (d) FIEBR

Figure 4.7: FO distributions of a representative control subject plotted on the upper unit sphere (viewed from top). (a) A sketch of the tongue orientation relative to these hemispheres and (b)-(d) FO distributions. Regions are highlighted in the FIEBR result for evaluation.

negative part of the line $x = 0$ show the fanning pattern of GG FOs (highlighted as region C in Figure 4.7(d)). In the results from the PEVs and CFARI, far fewer L-R directions are observed.

Next, fiber tracking was performed for further validation of the FO estimation. Using fiber tracking, we can evaluate the coherence of the FOs qualitatively. We placed seeds in GG and T separately. The results on the representative control subject are shown in Figures 4.8 and 4.9, where FIEBR is compared with both the

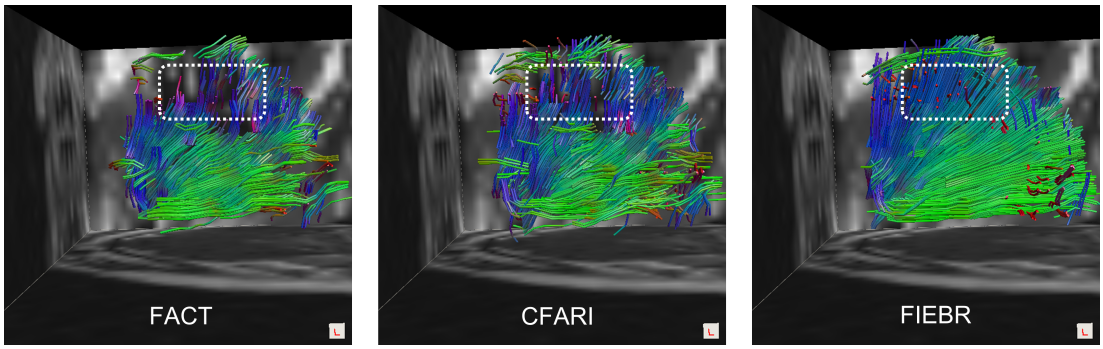

Figure 4.8: Fiber tracking results seeded in GG. Note the highlighted region for comparison.

FACT algorithm [3] and the fiber tracking method proposed in [27] that uses CFARI results. The visualization of fibers was created in TrackVis [126], where the fibers are color-coded by the orientation of each segment.

In Figure 4.8, it can be seen that, many of the GG fibers produced by FACT and CFARI terminate due to the crossing of GG with T and SL, while FIEBR tracks GG through these crossing regions (see the highlighted region). It is also evident that FIEBR produces smoother and more fan-shaped GG fibers than FACT and CFARI. Note that because of the seeds placed in crossing regions, in the FIEBR result we can also observe that some T and SL fibers are tracked. In Figure 4.9, FACT fails to produce T fibers, and CFARI only produces T fibers at the anterior portion of the tongue, while FIEBR reconstructs transverse T fibers throughout the tongue.

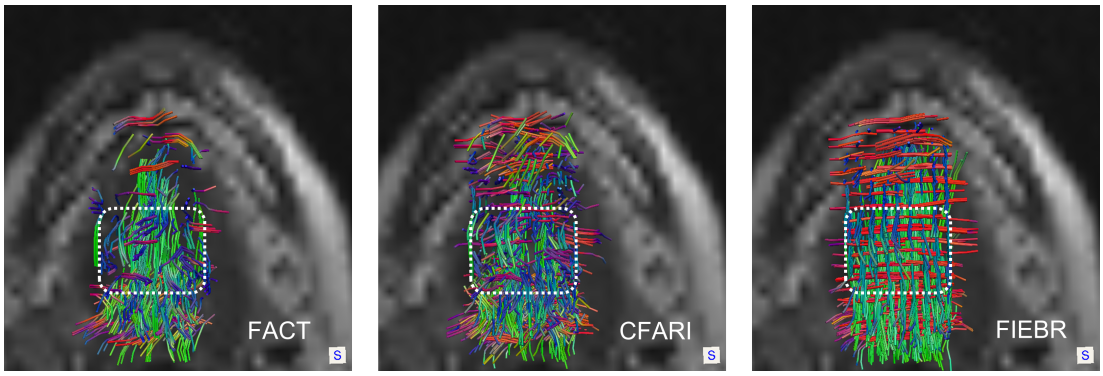

Figure 4.9: Fiber tracking results seeded in T. Note the highlighted region for comparison.

4.3.2.2 Application to Patients with Glossectomies

We then performed FIEBR on patients with partial glossectomies. An example and comparison of fiber tracking results is shown in Figure 4.10. Here we show the areas that are affected by the surgery near the mid-sagittal plane. Seeds were placed in GG. Compared to FACT and CFARI, FIEBR tracks GG through the crossing areas of GG and T (see the highlighted region). In the FIEBR result, it can be seen that sparser GG fibers in the lesion were tracked than outside the lesion. Note that because of seeding in the crossing regions of GG and T, some T fibers were also produced in the FIEBR result, and the T fibers are also sparser in the lesion than outside the lesion.

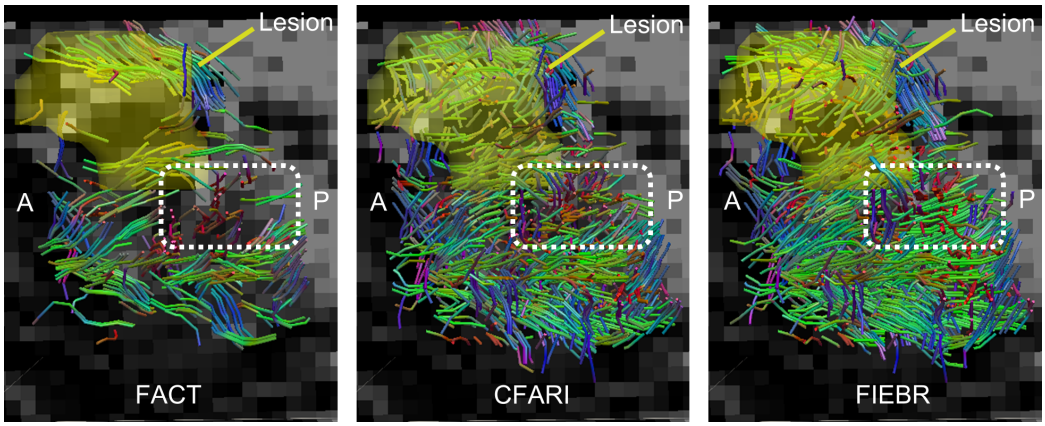

Figure 4.10: Fiber tracking results seeded in GG on a patient with a partial glossectomy. The results are shown near the lesion, which was delineated on the sagittal slices near the mid-sagittal plane. Note the highlighted region for comparison.

4.3.2.3 Comparison between Controls and Patients with Glossectomies

To investigate the influence of glossectomies on the muscles, we computed FO histograms for all patients. The distributions of the FOs in the tongue are plotted in Figure 4.11. Compared with the distribution in Figure 4.7, patients 1 and 3 show a similar organization of FOs, while patient 2 has a very different fiber organization. To quantitatively demonstrate this, we calculated the symmetric Kullback–Leibler divergence for the direction distributions between the subjects and list the result in Table 4.3. It can be seen that the divergence values between patient 2 and other subjects are much larger than those between the other subject pairs.

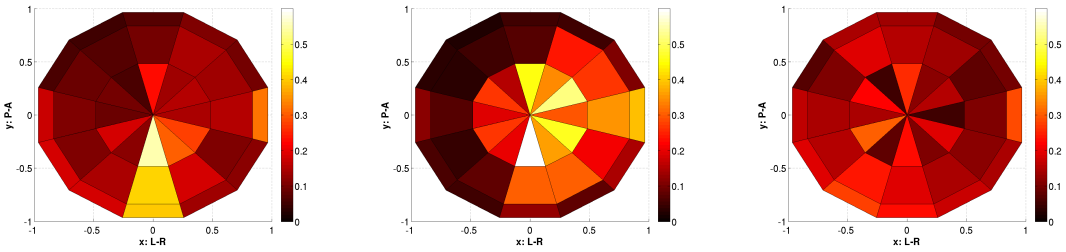

(a) Patient 1 (b) Patient 2 (c) Patient 3

Figure 4.11: Distributions of FOs of the patients plotted on the upper unit sphere. The hemisphere is viewed from top.

Table 4.3: The symmetric Kullback–Leibler divergence of the FO distributions between subjects.

	Control 1	Control 2	Control 3	Patient 1	Patient 2	Patient 3
Control 1	0	0.1292	0.0956	0.1117	0.3886	0.1316
Control 2		0	0.1820	0.1356	0.4486	0.1028
Control 3			0	0.1266	0.3483	0.1104
Patient 1				0	0.1958	0.1279
Patient 2					0	0.3541
Patient 3						0

4.4 Discussion

In the crossing phantom test, we observed that the inclusion of prior directional information enables the method to find the crossing patterns and reduce the effect of noise, even with inaccurate prior directions. The choice of the parameters should consider the factors such as noise levels and prior direction inaccuracy. Because the noise level can be estimated from the image but it is difficult to determine how accurate the prior information is, we tested different prior direction inaccuracies for each noise level, and used the average performance to decide the parameter setting for the real data application. These settings achieved results that are consistent with the anatomical structures of the muscles. For example, we have tracked transverse T

fibers and fanning GG fibers.

In the experiments on real tongue data, FIEBR tracks crossing fibers better than FACT [3] with the single tensor model and CFARI [27] which usually requires around 30 gradient directions. The addition of prior knowledge can also have a smoothing effect on fiber tracking. For the patients, the method is still able to distinguish interdigitated muscles, such as GG and T. It also reflects the anomalies caused by glossectomies, where the GG and T fibers terminate in the lesion.

The case study between the subjects shows that the control subjects share a consistent pattern of FOs (indicated by the divergence values in Table 4.3). Less organized FOs were observed in patient 2 while the other two patients have similar FO distributions as the control subjects. This could indicate that patient 2 is more affected by the glossectomy, where tongue muscles must be adapted to function after the surgery. This case study provides a possible example of applying the proposed method for clinical use.

4.5 Summary and Conclusion

In this chapter, we have proposed a Bayesian approach to distinguishing interdigitated tongue muscles with limited diffusion magnetic resonance imaging by incorporating prior directional knowledge. The diffusion weighted signals are modeled with a fixed tensor basis. We use MAP estimation, where the prior directional informa-

tion and the sparsity of the basis tensors are included in the prior distribution, and data fidelity is ensured in the likelihood term. The FOs are estimated by solving the resulting weighted ℓ_1-norm regularized least squares problem. Using the estimated FOs, a fiber tracking method is also presented.

The method was first applied on a digital crossing phantom for quantitative evaluation, and the results show that the use of prior information can correctly resolve crossing fibers and reduce the effect of noise. Based on the phantom results, parameter settings were determined for real data. Then the experiments were performed on *in vivo* tongue diffusion data and the results demonstrate that the proposed method is able to resolve crossing tongue muscle fibers with limited gradient directions. A case study on three control subjects and three patients with glossectomies shows that the method can reveal the difference in FO distributions between subjects. In particular, the Kullback–Leibler divergence values indicate that one of the patients is observed to have quite different organizations of FOs than the other subjects. This case study provides a potential tool to examine the influence of glossectomies on tongue muscles.

Chapter 5

Automatic Volumetric Segmentation of the Cerebellar Peduncles

5.1 Motivation

Previous studies on cerebellar peduncle atrophy have used manual delineations of the peduncles on magnetic resonance imaging (MRI) [51, 79], which can be subjective and time-consuming. Automatic segmentation of the cerebellar peduncles is therefore a crucial step which will enable larger studies involving more objective, reproducible, and efficient analytic methods.

Although fiber tract segmentation methods based on diffusion tensor imaging

(DTI) have been developed, none of the existing methods adequately segment the decussation of the superior cerebellar peduncles (dSCP). In [69] and [127], for example, fiber clustering is used to label the superior cerebellar peduncles (SCPs). However, the dSCP is entirely missing such that the SCPs pass beyond the red nuclei while never crossing (see Figure 5.1(a)). The problem occurs in large part because fiber tracking methods do not correctly track the separate tracts through the dSCP. Fiber tracking methods that resolve crossing regions have been reported [26, 27, 55–59, 109], but none of them have yet demonstrated the ability to resolve the dSCP. Although imaging methods that acquire more diffusion information—e.g., high angular resolution diffusion imaging (HARDI) [60] and diffusion spectrum imaging (DSI) [61]—can potentially enable detailed evaluation of the crossing fibers in the dSCP, they take a much longer imaging time than standard DTI, which makes them less practical for clinical use. In addition, with the large number of existing and ongoing DTI acquisitions, scientific studies on the cerebellar peduncles using DTI are still widely performed [82–88]. Therefore, development of better cerebellar peduncle segmentation methods on DTI remains an important technical goal.

To avoid using fiber tracking in tract segmentation, methods that directly segment the tracts by labeling the voxels based on features derived from DTI have been proposed. For example, the DOTS method reported in [15] explicitly models crossing regions and attempts to find them by matching their features near where they are expected to be found according to an atlas registered to the subject. Unfortunately,

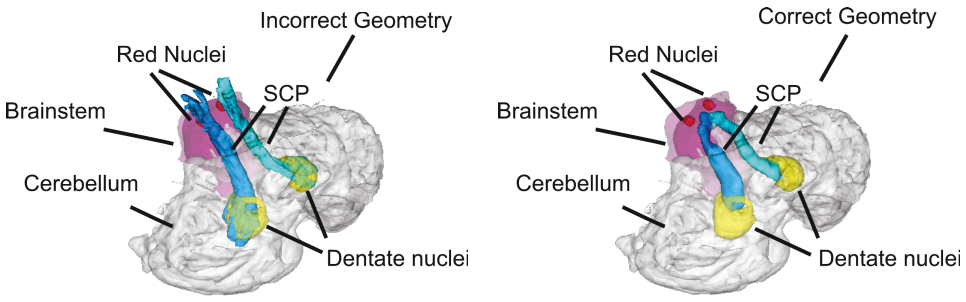

(a) (b)

Figure 5.1: The SCPs (blue and green) shown with the red nuclei (red) and the dentate nuclei (yellow): (a) typical incorrect SCPs obtained from DTI and (b) segmentation of the SCPs including the decussation in the proposed method. Note that our SCPs do not extend through the dentate nuclei, which leads to a different appearance of the dentate nuclei due to transparency.

because of the small size of the dSCP, DOTS is unable to register the feature atlas close enough to find the dSCP in test subjects. An improvement to DOTS reported in [18] incorporates the linear Westin index [128] as an additional feature, but this is still insufficient to provide a robust initialization and segmentation of the dSCP.

In this work, we propose an automatic method to volumetrically segment the cerebellar peduncles including the dSCP. The method models the dSCP, the noncrossing portions of the SCPs, the middle cerebellar peduncle (MCP), and the inferior cerebellar peduncles (ICPs) as separate objects based on the observation that the diffusion properties in these regions, including the primary eigenvectors (PEVs) of the tensors and the Westin indices [128], exhibit certain homogeneous properties. These features, together with spatial position information, are used to train a random forest classifier (RFC) [129] from manual delineations. The RFC is then used on new subjects to segment and label the peduncles. Because smoothness is not enforced in the RFC, a

further segmentation step is carried out using the multi-object geometric deformable model (MGDM) framework [130], which refines and smooths out the boundaries. An example of the proposed segmentation, depicting the SCPs that decussate, is shown in Figure 5.1(b). Note that in this work, we do not include the SCPs beyond the decussation because they cannot be well identified on DTI [90].

To show that the algorithm is scientifically useful, we studied differences between healthy controls and patients with a genetically defined cerebellar disease, spinocerebellar ataxia type 6 (SCA6). SCA6 is an autosomal dominant cerebellar ataxia and is characterized by progressive problems with movement [79]. Patients with SCA6 can experience discoordination, speech difficulties, and involuntary eye movements [131]. By studying the relationship between the cerebellar peduncles and SCA6, a better understanding of the disease with respect to anatomical changes can be obtained. Although previous studies have partially explored this relationship, they are applied in an indirect way by either measuring the diameter of the midbrain at the SCP level [79], or manually delineating regions of interest (ROIs) for analysis [51]. In this work, we automatically segmented the cerebellar peduncles of controls and SCA6 patients. Then the volume, fractional anisotropy (FA), and mean diffusivity (MD) of each peduncle were quantified and compared between the two groups.

5.2 Theory and Algorithm

5.2.1 Random Forest Classification of the Cerebellar Peduncles

An RFC is used to label each voxel, providing an initial estimation of the locations of the cerebellar peduncles. The RFC, which is trained by manual delineations of the peduncles, determines the classification using characteristic features including diffusion properties and spatial location information.

5.2.1.1 RFC

An RFC is a supervised classifier that is composed of a number of decision trees. Each tree is constructed based on the values of a random vector sampled from the training feature vectors independently [129]. For each test sample, a membership function m_i indicating the likelihood of the sample belonging to class i can be calculated as $m_i = N_i/N$, where N_i is the number of the trees predicting class i, and N is the total number of the trees in the forest. The class that corresponds to the maximum membership is selected as the label. This process yields both an estimated label and membership functions for all the labels which will be later used in the MGDM segmentation. In this work, seven labels are used: left noncrossing SCP (lSCP), right noncrossing SCP (rSCP), dSCP, MCP, left ICP (lICP), right ICP (rICP), and back-

ground (BG). Note that the noncrossing SCPs and the dSCP are different objects.

5.2.1.2 Features in the RFC

To apply the RFC, features must be extracted from the images and input into the classifier. Here, based on the observation that the cerebellar peduncles can be identified using the diffusion properties and spatial location, we use the PEV, the Westin indices [128], and a registered template to provide features.

When there is one primary diffusion direction, the PEV provides a good approximation of the direction [3]. Therefore, the PEV is a useful feature indicating the existence of tracts where there is no overlap. However, the PEV has bidirectional ambiguity; for example, $(-1, 0, 0)$ and $(1, 0, 0)$ represent the same PEV. Therefore, we map the PEV $\boldsymbol{u} = (u_1, u_2, u_3)$ into a 5D Knutsson space as follows [132]:

$$\begin{aligned} \boldsymbol{v} &= (v_1, v_2, v_3, v_4, v_5) \\ &= \frac{1}{||\boldsymbol{u}||}(u_1^2 - u_2^2, 2u_1u_2, 2u_1u_3, 2u_2u_3, \frac{1}{\sqrt{3}}(2u_3^2 - u_1^2 - u_2^2)). \end{aligned} \tag{5.1}$$

This mapping eliminates the directional ambiguity, and the resulting 5D Knutsson vector $\boldsymbol{v}$ serves as a feature in the RFC. An example of the Knutsson vector focused on the cerebellar peduncles in two axial slices is shown in Figure 5.2(a). The locations of the cerebellar peduncles are indicated within these slices and also shown as labels in Figure 5.2(b).

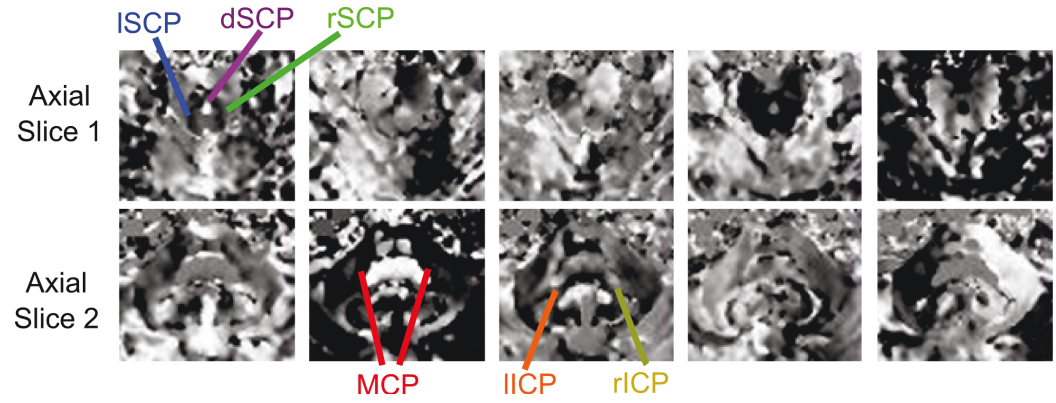

(a) 5D Knutsson Vector $\boldsymbol{v} = (v_1, v_2, v_3, v_4, v_5)$

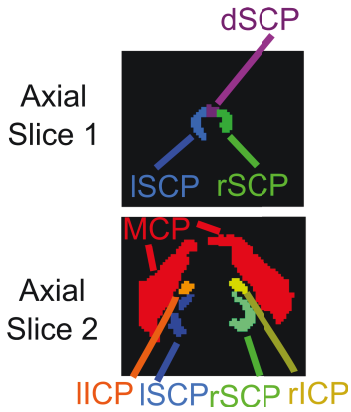

(b) Cerebellar Peduncles

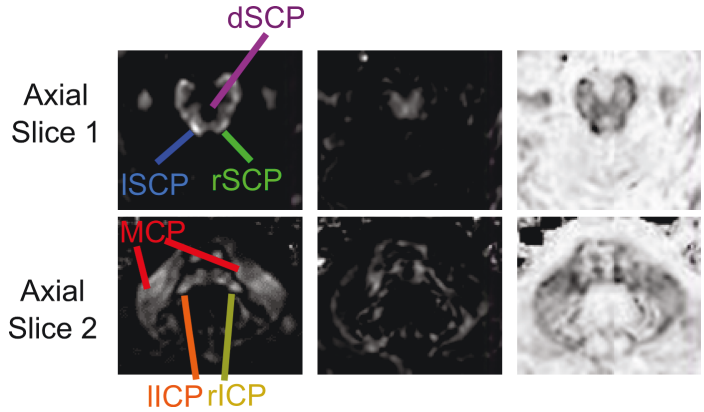

(c) Westin Indices $\boldsymbol{C} = (C_l, C_p, C_s)$

Figure 5.2: Diffusion properties and cerebellar peduncles on two representative slices (Row 1 and 2 in each subfigure): (a) the 5D Knutsson vector, (b) the cerebellar peduncles for reference, and (c) the Westin indices. Within each subfigure, Row 1 shows an axial slice cutting through the brainstem where the SCPs decussate, and Row 2 shows an axial slice cutting through the body of the MCP.

Although the PEV is a useful feature for the identification of tracts, it does not give useful information on whether fibers cross in a region. Thus, additional information for differentiation of noncrossing and crossing regions is required. The Westin indices can be used for this purpose [128]. The linear index C_l, the planar index C_p, and the spherical index C_s describe how linear, planar, and spherical, a tensor is shaped, respectively. Let $\lambda_1 \geq \lambda_2 \geq \lambda_3 \geq 0$ be the eigenvalues of the diffusion tensor; the

Westin indices are calculated as follows [128]:

$$C_l = \frac{\lambda_1 - \lambda_2}{\lambda_1 + \lambda_2 + \lambda_3}, \quad C_p = \frac{2(\lambda_2 - \lambda_3)}{\lambda_1 + \lambda_2 + \lambda_3}, \text{ and } C_s = \frac{3\lambda_3}{\lambda_1 + \lambda_2 + \lambda_3}. \tag{5.2}$$

Note that $0 \leq C_l, C_p, C_s \leq 1$ and $C_l + C_p + C_s = 1$. An example of the Westin indices is provided in Figure 5.2(c). When there is one primary diffusion direction, the tensor is linear-shaped and therefore high C_l values are expected. In the dSCP, the tensor is planar because it has crossing fibers, and therefore C_p increases and C_l drops. In isotropic areas, the tensor is spherical, and therefore C_s is large. Therefore, the Westin indices $\boldsymbol{C} = (C_l, C_p, C_s)$ are included as features to differentiate the cases of noncrossing tracts, crossing tracts, and isotropic areas.

An initial estimate of the spatial locations of all the cerebellar peduncles including the dSCP can be provided by registering a template to the subject to be segmented. We generated such a template by manual segmentation of a single subject. After experimentation, we determined that SyN registration [124] using the linear Westin index provides a reliable registration of the template to the target subject, where the mean square difference is selected as the similarity measure. To incorporate the information provided by SyN registration into the RFC, signed distance functions (SDFs), ϕ_{lSCP}, ϕ_{rSCP}, ϕ_{dSCP}, ϕ_{MCP}, ϕ_{lICP}, and ϕ_{rICP} are calculated from these transformed lSCP, rSCP, dSCP, MCP, lICP, and rICP labels, respectively. We refer to the SDFs as *spatial information* because these features provide infor-

mation on the spatial locations of the cerebellar peduncles. These distance maps $\boldsymbol{\phi} = (\phi_{\text{lSCP}}, \phi_{\text{rSCP}}, \phi_{\text{dSCP}}, \phi_{\text{MCP}}, \phi_{\text{lICP}}, \phi_{\text{rICP}})$ can indicate how far a voxel of the target subject is from the registered labels. Since the tracts should be close to the registered labels, lower values on a certain SDF could indicate higher possibility of the voxel belonging to the tract.

For each voxel at (x, y, z), we also supplement the SDFs with relative positions to the centers of the registered labels as additional spatial features:

$$\boldsymbol{x}_i = (x_i, y_i, z_i) = (x - \bar{x}_i, y - \bar{y}_i, z - \bar{z}_i),\ i \in \{\text{lSCP}, \text{rSCP}, \text{dSCP}, \text{MCP}, \text{lICP}, \text{rICP}\}, \tag{5.3}$$

where $(\bar{x}_i, \bar{y}_i, \bar{z}_i)$ is the center of the registered labels. The relative positions

$$\boldsymbol{x} = (\boldsymbol{x}_{\text{lSCP}}, \boldsymbol{x}_{\text{rSCP}}, \boldsymbol{x}_{\text{dSCP}}, \boldsymbol{x}_{\text{MCP}}, \boldsymbol{x}_{\text{lICP}}, \boldsymbol{x}_{\text{rICP}}) \tag{5.4}$$

give more detailed relationships between voxels and transformed templates.

In summary, the final feature vector $\boldsymbol{f}$ to be used in the RFC is a 32-dimensional vector composed of the Knutsson vector $\boldsymbol{v}$, the Westin indices $\boldsymbol{C}$, and the spatial information from the SDFs $\boldsymbol{\phi}$, and the relative positions $\boldsymbol{x}$, i.e.,

$$\boldsymbol{f} = (\boldsymbol{v}, \boldsymbol{C}, \boldsymbol{\phi}, \boldsymbol{x}). \tag{5.5}$$

5.2.1.3 Manual Delineations

To train the RFC, manual delineations of the cerebellar peduncles were made using a PEV edge map [133] and the linear Westin index. The PEV edge map is computed by first estimating the gradient matrix $\mathbf{G}$ of the 5D Knutsson vector with a finite difference operator [133]:

$$\mathbf{G} = \begin{pmatrix} \frac{\partial v_1}{\partial x} & \frac{\partial v_1}{\partial y} & \frac{\partial v_1}{\partial z} \\ \frac{\partial v_2}{\partial x} & \frac{\partial v_2}{\partial y} & \frac{\partial v_2}{\partial z} \\ \frac{\partial v_3}{\partial x} & \frac{\partial v_3}{\partial y} & \frac{\partial v_3}{\partial z} \\ \frac{\partial v_4}{\partial x} & \frac{\partial v_4}{\partial y} & \frac{\partial v_4}{\partial z} \\ \frac{\partial v_5}{\partial x} & \frac{\partial v_5}{\partial y} & \frac{\partial v_5}{\partial z} \end{pmatrix}. \tag{5.6}$$

Then the Frobenius norm can be calculated to obtain the edge map [133]:

$$||\mathbf{G}||_F = \sqrt{\sum_{j=1}^{3}\sum_{i=1}^{5} G_{ij}^2}. \tag{5.7}$$

On the PEV edge map, the PEVs inside a tract are homogeneous and appear as dark regions; at the tract boundaries, the PEVs are different from their neighbors and appear as bright edges (see Figure 5.3). Therefore, the PEV edge map contributes to the identification of the tracts for human raters. In addition, the noncrossing tracts have higher C_l values and crossing tracts have lower C_l values, which makes the C_l map a useful feature for tract delineation. In practice, these two maps are sufficient

for manual determination of the cerebellar peduncles. Figure 5.3 gives an example of the manual delineation and its relationship with the PEV edge map and the C_l map.

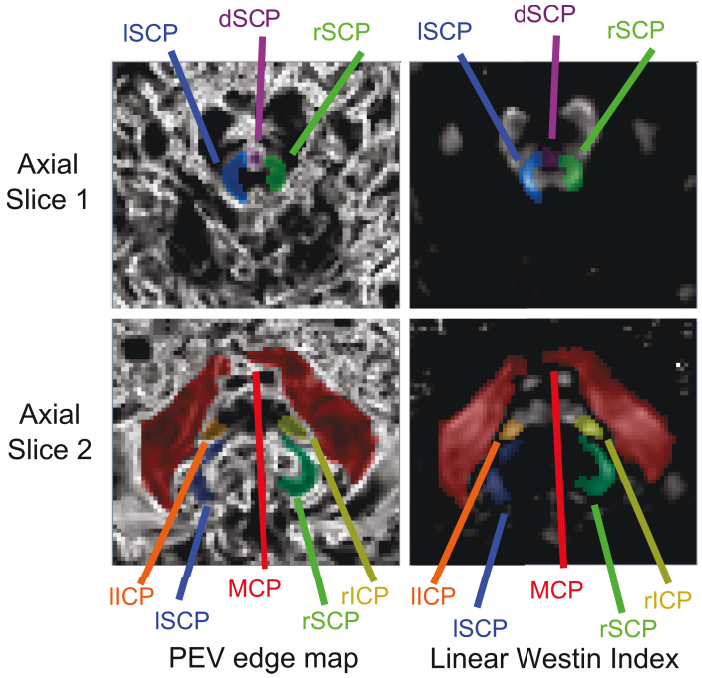

Figure 5.3: Manual delineations of the cerebellar peduncles overlaid on the PEV edge map (left) and the C_l map (right) on two representative slices (Row 1 and 2) in correspondence with Figure 5.2. Row 1 shows an axial slice cutting through the brainstem where the SCPs decussate, and Row 2 shows an axial slice cutting through the body of the MCP.

5.2.2 MGDM Segmentation

The RFC provides an initial classification of the cerebellar peduncles, but we still have two problems to contend with. First, the RFC applies to each voxel independently, which potentially leaves objects disconnected or highly irregular. Second, the RFC training may have unbalanced samples (where majority classes tend to be

favored in RFC decisions), which will produce a bias in the sizes or positions of segmented objects. We therefore use MGDM [130] as a second stage in order to provide both spatial smoothness and additional fidelity to the data.

5.2.2.1 MGDM

MGDM is a framework for multiple object segmentation [130]. It efficiently evolves objects using a decomposition of the signed distance functions of all objects, and prevents overlaps and gaps between objects. The conventional speed functions that are used in geometric deformable models [134, 135] can be applied in MGDM, and MGDM also enables users to use different speed functions on the boundaries between different object pairs. Let $\phi_{i,j}$ be the level set function for the boundary between object i and j. Then its evolution can be written as:

$$\frac{\partial \phi_{i,j}}{\partial t} + f_{\text{reg:}i,j}|\nabla \phi_{i,j}| + \boldsymbol{f}_{\text{adv:}i,j} \cdot \nabla \phi_{i,j} = \epsilon\kappa|\nabla \phi_{i,j}|, \tag{5.8}$$

where $f_{\text{reg:}i,j}$ represents a region speed, $\boldsymbol{f}_{\text{adv:}i,j}$ stands for an advection speed, and κ is a curvature speed. As with any deformable model, MGDM works best if initialized close to the final configuration. Therefore, our RFC segmentation result forms the initialization for MGDM. Using this framework, we can design the speed functions for specific boundaries to refine the RFC segmentation.

5.2.2.2 Speed Design of MGDM Smoothing

To preserve smoothness, a curvature speed on each boundary is used in MGDM. Using the membership functions from the RFC output, region speeds are also specified. A region speed shrinks or expands the boundary according to the membership functions and prevents the shrinkage caused by the curvature speed so that the boundaries will not deviate far from the RFC result. Region speeds can also correct bias in the RFC. Since the number of background voxels exceeds those of the tracts and the ratio can range from the scale of 10:1 to 1000:1, depending on which peduncle it is, the RFC results can be biased. For example, a voxel belonging to the cerebellar peduncles can have a relatively high membership value of the true label, yet it is exceeded by an even higher background membership value. By choosing thresholds of the membership in the region speeds, a compensation for the RFC bias can be achieved.

Specifically, the region speed on each boundary is designed as follows:

$$\begin{cases} f_{\text{reg:}i,\text{BG}} = \alpha(m_i - t_i), & i \neq \text{BG} \\ f_{\text{reg:}i,j} = \alpha(m_i - m_j), & i, j \neq \text{BG} \end{cases} . \tag{5.9}$$

Here α is a weighting constant, t_i is a thresholding constant for tract i, and m_i represents the corresponding membership computed from the RFC. The constant t_i replaces the background membership for the RFC bias compensation, and is deter-

mined empirically. In practice, this replacement achieves more accurate results and prevents the background from being overestimated.

5.3 Experiments

The proposed segmentation algorithm was first validated using diffusion MRI from nine subjects (five controls and four patients with SCA6). These nine subjects compose the first data set. Then the diffusion MRI from 32 controls and 11 SCA6 patients that are different from the subjects in the first data set were used to study group differences. These 43 subjects compose the second data set. Diffusion weighted images (DWIs) were acquired using a multi-slice, single-shot EPI sequence on a 3T MR scanner (Intera, Philips Medical Systems, Netherlands). The sequence in the first and second data set consist of 32 and 30 gradient directions, respectively, and one $b0$ image. The b-value is 700 s/mm^2. The original in-plane resolution of the two data sets is 2.2 mm $\times$ 2.2 mm, with a matrix size of 96 $\times$ 96; and the original slice thickness of the two data sets is 2.2 mm. The scanner resampled the slices and generated the output resolution of 0.828 mm $\times$ 0.828 mm $\times$ 2.2 mm, where the in-plane matrix size is 256 $\times$ 256. Then we isotropically resampled the DWIs, where the resolutions of the first and the second data set are 1 mm and 0.828 mm isotropic, respectively. Finally, diffusion tensors were computed using CATNAP [108] in the JIST software [107].

5.3.1 Validation

A leave-one-out cross-validation was performed on the nine subjects in the first data set. Manual delineations of the cerebellar peduncles including the dSCP were made on these subjects. For each test subject, the other eight subjects were used in the training phase. In the RFC, 100 trees were constructed and at each tree node five features were sampled. Both control subjects and patients with SCA6 were included in the training. To save computational time and memory in the training phase, only voxels that are within a certain distance to any of the transformed labels on the registered template were considered. The distance was empirically set to 10 mm to include all the possible voxels of the cerebellar peduncles.

In training an RFC, a measure of the relative importance of each feature called *variable importance* [129] can be computed. The variable importance measures the mean decrease in classification accuracy after permuting the feature over all the trees [129]. In this experiment, the patterns of the variable importance are similar across the subjects. The means and standard deviations of the variable importance of the elements in the feature vector are shown in Figure 5.4. The SDF of the MCP and the linear Westin index have much higher importance than the other features.

After training, test data were segmented as proposed. An example of the 3D rendering of the segmentation result is displayed in an oblique view in Figure 5.5(a), where the noncrossing and crossing SCPs are combined to get the complete left and right SCPs. Examples of the cross sections of the segmentation result overlaid on the

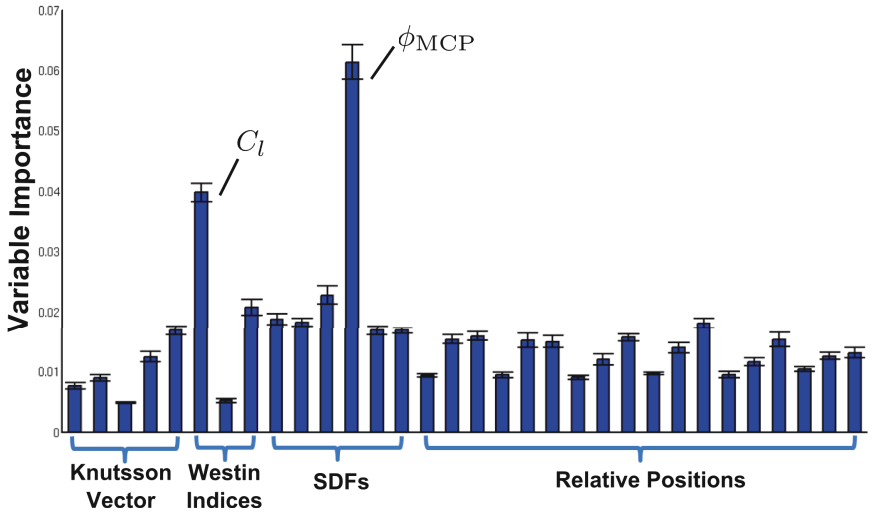

Figure 5.4: Means and standard deviations of the variable importance in the cross-validation test. The order of the variables is the same as in the feature vector $\boldsymbol{f} = (\boldsymbol{v}, \boldsymbol{C}, \boldsymbol{\phi}, \boldsymbol{x})$.

FA map are also given on different slices and compared with the manual delineations in Figures 5.5(b) and 5.5(c). The first axial slice shows a cut through the brainstem where the SCPs decussate, and the second slice shows a cut through the cerebellum where all the cerebellar peduncles are visible. It can be seen that the proposed segmentation method is able to correctly localize the cerebellar peduncles.

To quantitatively evaluate the segmentation accuracy of the proposed method, the Dice coefficients [136] and average surface distances (ASDs) between the segmentation results and manual delineations were computed, and they are listed in Tables 5.1 and 5.2, respectively. The numbers are also listed for the RFC initialization to show the improvement of MGDM over RFC alone. For convenience, in the tables, the intermediate RFC result and the final segmentation after MGDM refinement are

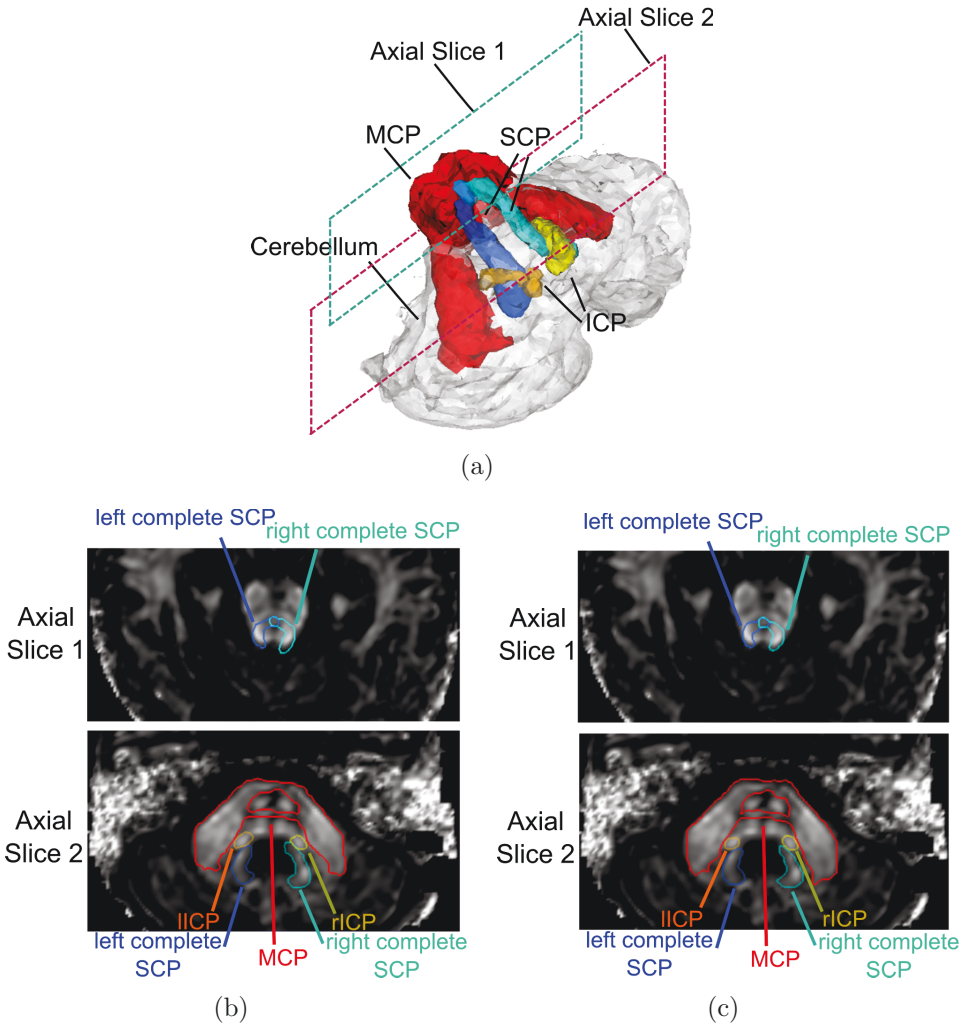

Figure 5.5: A segmentation result. (a) A 3D rendering (oblique view) of the cerebellar peduncles segmented by the proposed method in the cross-validation test, shown together with the cerebellum (gray). Axial cross sections of (b) the manual delineations and (c) the proposed segmentation contours overlaid on the FA map. Slice 1: a cut through the brainstem where the SCPs decussate. Slice 2: a cut through the cerebellum where all the cerebellar peduncles are visible. In all figures here, the left and right noncrossing SCPs are combined respectively with the dSCP to obtain the complete left and right SCPs. Blue: left complete SCP; green: right complete SCP; red: MCP; orange: lICP; yellow: rICP.

called "RFC" and "RFC + MGDM", respectively.

Since no existing method provides a comparison of the segmentation of cerebellar

peduncles including the dSCP, and volumetric delineations of the cerebellar peduncles of the subjects are available, we compared our result with two registration-based methods. Each subject was segmented by the two registration-based methods using a leave-one-out cross-validation as well. For the first comparison method, we used the SyN registration algorithm [124] to map the training delineations to the test target, using the C_l images and mean square difference as the similarity measure. The C_l images were chosen over the FA maps because they provide better contrast for the tracts. Then spatial STAPLE [137] was used as the voting scheme. Spatial STAPLE achieves better label fusion than the STAPLE algorithm [138] by incorporating spatially varying rater performance. For the second comparison method, we applied the tensor-based registration method implemented in DTI-TK [139] to map the training delineations to the test target using the diffusion tensor. Then spatial STAPLE [137] was also used to provide the final segmentation. The two comparison methods are referred to as "SyN + s-STAPLE" and "DTI-TK + s-STAPLE", respectively. The corresponding Dice coefficients and the ASDs are given in Tables 5.1 and 5.2.

The final segmentation of our method is compared with our intermediate RFC result, the SyN + s-STAPLE result, and the DTI-TK + s-STAPLE result. To show the statistical significance of the performance difference, the paired Student's t-test and Wilcoxon signed-rank test were performed with respect to the Dice coefficients and ASDs, respectively. The p-values are shown in Tables 5.3 and 5.4.

To better understand the implications of these experimental results, we first study

Table 5.1: The Dice coefficients between the segmentation results and manual delineations. Mean Dice coefficients from the proposed method are set in bold font.

	RFC						RFC + MGDM					
	lSCP	rSCP	dSCP	MCP	lICP	rICP	lSCP	rSCP	dSCP	MCP	lICP	rICP
S1	0.828	0.793	0.702	0.826	0.753	0.762	0.839	0.762	0.689	0.817	0.782	0.787
S2	0.776	0.766	0.753	0.860	0.670	0.660	0.824	0.816	0.815	0.850	0.675	0.676
S3	0.774	0.722	0.834	0.831	0.712	0.710	0.803	0.783	0.870	0.828	0.759	0.752
S4	0.739	0.797	0.719	0.874	0.655	0.616	0.815	0.809	0.758	0.870	0.695	0.648
S5	0.820	0.797	0.816	0.856	0.777	0.728	0.798	0.775	0.862	0.864	0.777	0.778
S6	0.813	0.778	0.286	0.838	0.678	0.689	0.786	0.770	0.711	0.843	0.704	0.729
S7	0.833	0.820	0.755	0.865	0.720	0.680	0.769	0.795	0.775	0.872	0.731	0.702
S8	0.807	0.785	0.826	0.829	0.640	0.668	0.785	0.767	0.785	0.851	0.681	0.705
S9	0.785	0.763	0.787	0.851	0.739	0.674	0.799	0.795	0.833	0.855	0.765	0.707
Mean	0.797	0.780	0.720	0.848	0.705	0.688	**0.802**	**0.786**	**0.789**	**0.850**	**0.730**	**0.720**
Std.	0.031	0.028	0.169	0.017	0.047	0.042	0.022	0.019	0.063	0.018	0.042	0.046
	SyN + s-STAPLE						DTI-TK + s-STAPLE					
	lSCP	rSCP	dSCP	MCP	lICP	rICP	lSCP	rSCP	dSCP	MCP	lICP	rICP
S1	0.748	0.693	0.637	0.832	0.732	0.773	0.784	0.770	0.725	0.819	0.751	0.757
S2	0.793	0.797	0.704	0.852	0.625	0.657	0.803	0.799	0.746	0.839	0.672	0.683
S3	0.731	0.757	0.794	0.815	0.715	0.622	0.724	0.726	0.597	0.813	0.764	0.692
S4	0.804	0.771	0.764	0.865	0.729	0.662	0.796	0.780	0.585	0.852	0.753	0.694
S5	0.721	0.697	0.752	0.856	0.705	0.728	0.803	0.770	0.741	0.832	0.737	0.727
S6	0.689	0.750	0.528	0.853	0.662	0.723	0.686	0.725	0.563	0.853	0.648	0.682
S7	0.709	0.753	0.640	0.848	0.637	0.678	0.748	0.748	0.571	0.835	0.625	0.651
S8	0.753	0.697	0.618	0.814	0.675	0.672	0.765	0.754	0.630	0.790	0.634	0.586
S9	0.764	0.774	0.836	0.838	0.746	0.742	0.758	0.770	0.817	0.814	0.710	0.725
Mean	0.746	0.744	0.697	0.841	0.692	0.695	0.763	0.760	0.664	0.828	0.699	0.689
Std.	0.038	0.038	0.099	0.018	0.044	0.048	0.039	0.025	0.094	0.020	0.055	0.049

Table 5.2: The ASDs (mm) between the segmentation results and manual delineations. The mean ASDs from the proposed method are set in bold font.

	RFC						RFC + MGDM					
	lSCP	rSCP	dSCP	MCP	lICP	rICP	lSCP	rSCP	dSCP	MCP	lICP	rICP
S1	0.391	0.562	0.484	0.618	0.647	0.561	0.408	0.675	0.552	0.700	0.582	0.523
S2	0.621	0.627	0.385	0.542	0.895	0.816	0.501	0.510	0.298	0.599	0.902	0.796
S3	0.585	0.748	0.314	0.621	0.700	0.676	0.521	0.590	0.268	0.663	0.611	0.614
S4	0.591	0.452	0.423	0.504	0.826	0.893	0.424	0.449	0.358	0.551	0.797	0.873
S5	0.820	0.797	0.816	0.856	0.777	0.728	0.512	0.539	0.212	0.569	0.589	0.516
S6	0.416	0.486	0.945	0.801	0.776	0.723	0.492	0.552	0.395	0.789	0.735	0.635
S7	0.354	0.377	0.275	0.734	0.645	0.813	0.533	0.503	0.313	0.678	0.641	0.755
S8	0.430	0.456	0.234	0.846	0.876	0.785	0.518	0.543	0.291	0.759	0.819	0.710
S9	0.450	0.516	0.376	0.720	0.635	0.801	0.458	0.471	0.328	0.684	0.596	0.725
Mean	0.518	0.558	0.472	0.694	0.753	0.755	**0.485**	**0.537**	**0.335**	**0.666**	**0.697**	**0.683**
Std.	0.149	0.141	0.246	0.129	0.101	0.097	0.045	0.067	0.097	0.081	0.119	0.121
	SyN + s-STAPLE						DTI-TK + s-STAPLE					
	lSCP	rSCP	dSCP	MCP	lICP	rICP	lSCP	rSCP	dSCP	MCP	lICP	rICP
S1	0.669	0.827	0.684	0.614	0.691	0.540	0.519	0.612	0.463	0.690	0.633	0.583
S2	0.547	0.534	0.562	0.611	1.089	0.984	0.527	0.517	0.388	0.730	0.854	0.739
S3	0.711	0.638	0.400	0.684	0.761	1.183	0.711	0.679	0.772	0.685	0.604	0.842
S4	0.558	0.540	0.411	0.541	0.618	0.810	0.786	0.515	0.571	0.590	0.577	0.704
S5	0.698	0.743	0.386	0.587	0.843	0.698	0.481	0.540	0.350	0.664	0.673	0.677
S6	0.782	0.607	0.831	0.624	0.737	0.657	0.793	0.686	0.787	0.662	0.795	0.706
S7	0.786	0.614	0.568	0.899	0.909	0.803	0.585	0.578	0.640	0.998	0.926	0.835
S8	0.595	0.764	0.630	1.042	0.764	0.770	0.531	0.564	0.567	1.168	0.870	1.003
S9	0.593	0.533	0.309	0.963	0.641	0.655	0.629	0.526	0.314	1.047	0.724	0.675
Mean	0.660	0.645	0.531	0.729	0.784	0.789	0.618	0.580	0.539	0.804	0.740	0.752
Std.	0.091	0.109	0.169	0.186	0.146	0.194	0.119	0.066	0.174	0.208	0.127	0.124

the difference between RFC and RFC + MGDM results. It can be seen from Table 5.1 that the proposed method (RFC + MGDM) improves over the RFC results and has mean Dice coefficients ranging from 0.720 to 0.850, a range which is generally thought to be acceptable, especially for small white matter tracts [16, 140]. In Table 5.2, it can be seen that the mean ASDs of the proposed intermediate RFC segmentation and final RFC + MGDM segmentation are in the range of 0.472 mm to 0.755 mm and 0.335 mm to 0.697 mm, respectively. Compared to RFC results, the final segmentation (RFC+MGDM) has higher mean Dice coefficients and lower mean ASDs for all the structures, showing the improvement of using MGDM. The improvement of the lICP and rICP segmentation is significant in terms of both Dice coefficients and ASDs in both statistical tests (see Tables 5.3 and 5.4).

We now turn to the comparisons of our method (RFC + MGDM) with the two multi-atlas registration-based methods. In Tables 5.1 and 5.2, for all the structures, the mean Dice coefficients of the final results of the proposed method are higher than the two competing methods, and the mean ASDs of the proposed method are lower than the two competing methods. With respect to the Dice coefficients, in both statistical tests (see Table 5.3), the proposed method performs better than SyN + s-STAPLE with significance for the lSCP, the rSCP, the dSCP, and the lICP; the proposed method also shows significantly better performance than DTI-TK + s-STAPLE for the lSCP, the rSCP, the dSCP, and the MCP. With respect to the ASDs, in the paired Student's test (see Table 5.4), the proposed method better segments the

Table 5.3: The p-values of the paired Student's t-test and the Wilcoxon signed-rank test for comparing the Dice coefficients between RFC + MGDM results and the other three results. Note that the mean Dice coefficients of RFC + MGDM are greater than those in the other three results as shown in Table 5.1.

	Paired Student's t-test					
	lSCP	rSCP	dSCP	MCP	lICP	rICP
RFC	0.7520	0.6341	0.1726	0.5317	0.0019*	1.4E-5***
SyN + s-STAPLE	0.0005***	0.0007***	0.0037*	0.1521	0.0161*	0.1424
DTI-TK + s-STAPLE	0.0080*	0.0071*	0.0044*	0.0162*	0.0834	0.0882
	Wilcoxon signed-rank test					
	lSCP	rSCP	dSCP	MCP	lICP	rICP
RFC	0.8203	0.7344	0.0547	0.6523	0.0039*	0.0039*
SyN + s-STAPLE	0.0039*	0.0039*	0.0195*	0.2031	0.0195*	0.1641
DTI-TK + s-STAPLE	0.0078*	0.0117*	0.0117*	0.0195*	0.1641	0.0742

Note: $^{*}p < 0.05$, $^{***}p < 0.001$

lSCP, the rSCP, and the dSCP than SyN + s-STAPLE with significance, and better segments the lSCP and the dSCP than DTI-TK + s-STAPLE with significance; in the Wilcoxon signed-rank test (see Table 5.4), the proposed method better segments the lSCP, the rSCP, and the dSCP than SyN + s-STAPLE and DTI-TK + s-STAPLE with significance.

5.3.2 Application to SCA6

The proposed method was next applied on the second data set which contains 32 controls and 11 patients. All the data in the first smaller data set were included in the training phase and were not used in the testing phase.

Tract volumes, average FAs, and average MDs of the segmented cerebellar peduncles were calculated. The values were corrected using a general linear model to remove the confounding effects of age and sex using the method in [141]. These cor-

Table 5.4: The p-values of the paired Student's t-test and the Wilcoxon signed-rank test for comparing the ASDs between RFC + MGDM results and the other three results. Note that the mean ASDs in RFC + MGDM results are lower than those in the other three results as shown in Table 5.2.

	Paired Student's t-test					
	lSCP	rSCP	dSCP	MCP	lICP	rICP
RFC	0.5339	0.6506	0.1458	0.4810	0.0190*	0.0057*
SyN + s-STAPLE	0.0003***	0.0018*	0.0033*	0.2686	0.1160	0.1430
DTI-TK + s-STAPLE	0.0184*	0.0571	0.0130*	0.0560	0.3740	0.1970
	Wilcoxon signed-rank test					
	lSCP	rSCP	dSCP	MCP	lICP	rICP
RFC	0.8203	0.7344	0.2031	0.8203	0.0117*	0.0039*
SyN + s-STAPLE	0.0039*	0.0039*	0.0078*	0.2500	0.1289	0.2031
DTI-TK + s-STAPLE	0.0195*	0.0391*	0.0195*	0.0547	0.2031	0.1641

Note: $^{*}p < 0.05$, $^{***}p < 0.001$

rected numbers were then analyzed with a Student's t-test and a Wilcoxon rank-sum test for comparison between the two groups. The corrected statistics are shown in the box plots in Figure 5.6, where structures with significant differences observed in both the Student's t-test and the Wilcoxon rank-sum test are indicated. The p-values in the two tests are listed in Table 5.5. Significant decreases in the volumes of the dSCP, the lICP, and the rICP are observed in the SCA6 group in both statistical tests. Although a significant FA increase in the lICP is observed in the SCA6 group in the Wilcoxon rank-sum test, no significant FA changes in both statistical tests are found for any tract. The MD is observed to be increasing with statistical significance in the lSCP, the rSCP, the MCP, the lICP, and the rICP in the SCA6 group in both statistical tests.

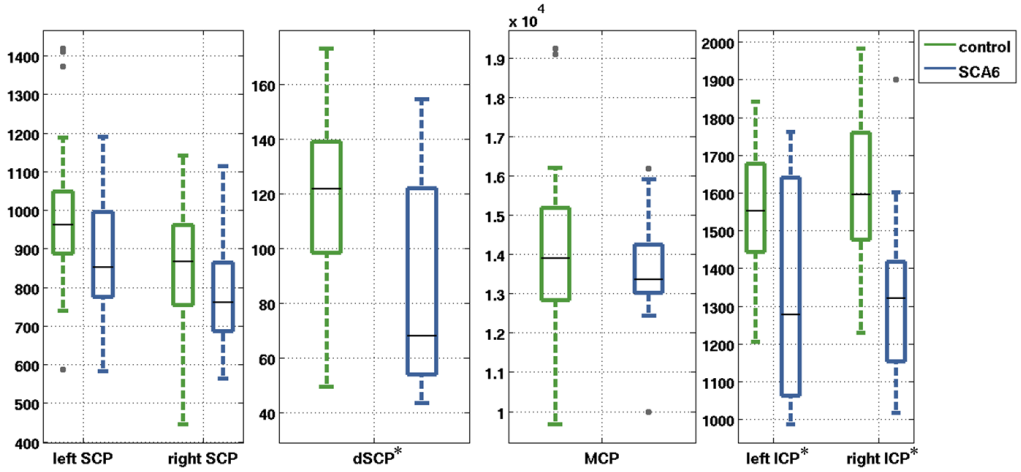

(a) Volume (mm^3)

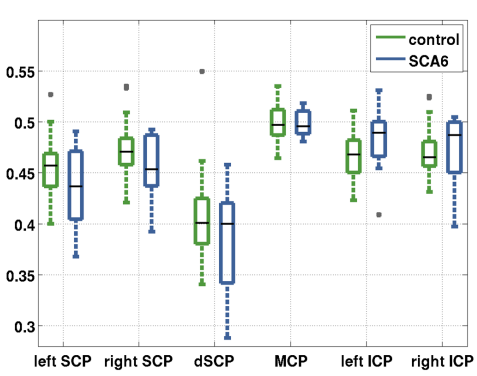

(b) FA

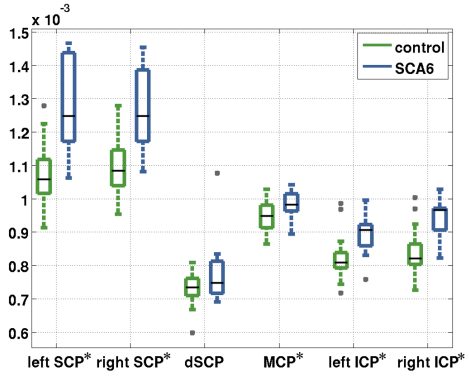

(c) MD (mm^2/s)

Figure 5.6: Box plots of (a) tract volumes, (b) average FAs, and (c) average MDs of the segmented cerebellar peduncles. The numbers are compared between the control and the SCA6 group. Asterisks (*) indicate that statistically significant difference ($p < 0.05$) is observed in both Student's t-test and Wilcoxon rank-sum test.

5.4 Discussion

For the SCP, we have focused on the dSCP and the noncrossing portions below the dSCP. The boundary of the SCP beyond the dSCP is quite ambiguous on the PEV edge map and the C_l map which we use for delineation. The manual delineations

Table 5.5: The p-values of the Student's t-test and the Wilcoxon rank-sum test for comparing the volumes, average FAs, and average MDs of the cerebellar peduncles between the control and SCA6 group.

	Volume					
	lSCP	rSCP	dSCP	MCP	lICP	rICP
Student's t-test	0.0857	0.2902	0.0321*	0.3737	0.0465*	0.0055*
Wilcoxon rank-sum test	0.0977	0.1517	0.0269*	0.5683	0.0466*	0.0013*
	FA					
	lSCP	rSCP	dSCP	MCP	lICP	rICP
Student's t-test	0.2089	0.1335	0.2344	0.9134	0.1576	0.7310
Wilcoxon rank-sum test	0.3806	0.2596	0.4276	0.9889	0.0466*	0.4116
	MD					
	lSCP	rSCP	dSCP	MCP	lICP	rICP
Student's t-test	0.0005***	0.0010*	0.1476	0.0262*	0.0028*	0.0002***
Wilcoxon rank-sum test	0.0001***	0.0002***	0.2368	0.0332*	0.0014*	0.0002***

Note: $^{*}p < 0.05$, $^{***}p < 0.001$

of this part of the SCPs involve a large amount of speculation, and therefore it is not included in this work. Despite the exclusion, the segmentation of the dSCP and the SCP below the dSCP is able to reveal anatomical differences between groups, as shown in the results, and therefore we believe the proposed method is valuable for scientific studies.

In training the RFC, the high variable importance of ϕ_{MCP} is probably because the number of MCP voxels is much larger than those of the other peduncles. The high variable importance of C_l is consistent with the fact that manual delineations are based, in part, on the C_l map and also because C_l is high for noncrossing white matter tracts, which is largely what is being segmented.

In the cross-validation study, the ICPs have worse mean Dice coefficients and ASDs than the other structures. This could be because the ICPs extend out of the

cerebellum and can be influenced by the field of view (FOV) of the DWIs.

The measurement of the Dice coefficients and ASDs and the statistical tests indicate that the proposed final results (RFC + MGDM) achieve more accurate segmentation than the intermediate RFC. These results also show the superiority of the proposed algorithm to the two multi-atlas registration-based methods. Note that for the dSCP, the proposed method improves the mean Dice coefficient over SyN + s-STAPLE and DTI-TK + s-STAPLE by 0.092 (13.2%) and 0.125 (18.8%), respectively, and improves the mean ASD over SyN + s-STAPLE and DTI-TK + s-STAPLE by 0.196 mm (36.9%) and 0.204 mm (37.8%), respectively. The improvement of the dSCP segmentation is larger than those of the segmentation of the other noncrossing structures. Moreover, this improvement is significant in both statistical tests.

In the second experiment that studies the group differences between controls and SCA6 patients, the significant decreases in the volumes of the dSCP, the lSCP, and the rICP in the SCA6 group reveal atrophy of the cerebellar peduncles. Note that the volumes of the noncrossing SCPs do not demonstrate significant differences, which emphasizes the importance of segmenting the crossing regions. In the comparison of FA values, it is worth noting that the mean FAs in the ICPs of the SCA6 group tend to be higher than those in the control group. This could be a result of the ICP volume decrease, where the regions with lower FA near the tract boundaries are more affected than the regions with higher FA close to the centerline of the tract. The ICPs with lower FA atrophy more while the ICPs with higher FA are better preserved, causing

the average FA in the ICPs to increase. Furthermore, the MD is observed to be increasing significantly in the lSCP, the rSCP, the MCP, the lICP, and the rICP in the SCA6 group. The MD increase can be possibly due to the degeneration of the neural tracts, which could lead to reduction of cells that constrain water and therefore higher diffusion. Thus the increasing MD in these tracts is also a possible sign of their degeneration.

5.5 Summary and Conclusion

In this chapter, we have proposed an automatic method for segmenting the cerebellar peduncles including the decussation of the SCPs, which is nearly always missing in previous studies. Like the noncrossing cerebellar peduncles, the dSCP is modeled explicitly as a single class. An RFC is used to classify the voxels based on the PEVs, the Westin indices, and spatial information. The RFC result is further refined by MGDM segmentation to confer smoothness and compensate for possible bias due to unbalanced samples.

A leave-one-out cross-validation was carried out for qualitative and quantitative evaluation of the method. The Dice coefficients and average surface distances were calculated. Results on nine subjects indicate that the method is able to resolve the crossing of the SCPs and accurately segment the cerebellar peduncles. Furthermore, the proposed method outperforms two registration-based methods.

Experiments on a larger data set were performed to show that the method is useful for scientific studies. Results indicate that the volumes of the dSCP, the lICP, and the rICP decrease with statistical significance in the SCA6 group. The changes involving the dSCP also emphasizes the importance of the ability to identify the decussation. Furthermore, the mean MD values in noncrossing SCP regions, the MCP, and the ICPs are significantly larger in the SCA6 group, which is also a possible indicator of tract degeneration. These findings are consistent with the degeneration of the cerebellar peduncles in SCA6 patients and show the benefit of applying the proposed method for scientific studies.

Chapter 6

Conclusions and Future Work

6.1 Summary

This thesis presented fiber tracking and tract segmentation methods that can tackle the issue of crossing fibers based on diffusion tensor imaging (DTI). First, a fiber tracking method guided by volumetric tract segmentation was developed, which incorporates anatomical information to reduce errors caused by image noise and crossing fibers. Second, an algorithm for distinguishing interdigitated tongue muscles was designed, where prior directional knowledge is included to account for the insufficient information due to limited diffusion gradient directions in *in vivo* tongue diffusion imaging. Finally, a volumetric tract segmentation method focused on the cerebellar peduncles was described. It is able to resolve crossing tracts and accurately localize the small crossing regions. Moreover, the method was applied

for a study of spinocerebellar ataxia type 6 (SCA6), where anatomical changes with respect to the disease were investigated. In this chapter, a summary of the main results in the thesis is provided and future work directions are discussed.

6.2 Fiber Tracking Guided by Volumetric Segmentation

6.2.1 Main Results

1. The proposed method incorporates anatomical information from volumetric tract segmentation to guide fiber tracking, which has not been previously explored.

2. In the digital crossing phantom test, the proposed method estimates fiber orientations (FOs) more accurately than two popular multi-tensor models, BEDPOSTX and CFARI.

3. In the physical phantom test, the proposed method better produces crossing FOs than BEDPOSTX and CFARI.

4. On a representative control subject, compared with the DTI model, BEDPOSTX, and CFARI, the proposed method reduces false fiber streamlines and cortical connections due to crossing fibers and image noise.

5. We performed a study on the brain connectome using 18 control subjects, where connectivity of named tracts to cortical regions was investigated.

6.2.2 Future Work

There are ways to extend and further improve this methodology. For example, we have applied the proposed method on the DTI model and it would be interesting to combine the guidance of volumetric tract segmentation with multi-tensor models or more advanced imaging techniques such as high angular resolution diffusion imaging (HARDI) [60] and diffusion spectrum imaging (DSI) [61]. Raw FOs without guidance of volumetric segmentation can be estimated using multi-tensor models [26, 27, 56] or a spherical ridgelet model [57] on DTI, constrained spherical deconvolution [142] or q-ball reconstruction [23] on HARDI, and local maximum method on DSI [143]. In noncrossing regions, the FOs to be estimated should agree with tract segmentation and the single raw FOs calculated from these more advanced techniques. In crossing regions, it can be either using only the information from tract segmentation as proposed in this paper or also considering one of the crossing raw FOs. In the first case, the proposed method can be readily applied. In the latter case, the energy function in Eq. (3.13) becomes

$$\begin{aligned}\hat{\boldsymbol{f}} &= \underset{|\boldsymbol{f}(x)|=1}{\arg\min} \sum_{x\in\mathcal{L}} (\alpha|\nabla \boldsymbol{f}(x)|^2 + \mu(x)|\boldsymbol{g}(x)\cdot \boldsymbol{f}(x)|^2 + \\ &\qquad \lambda_0 |S(\boldsymbol{v}_1(x), \boldsymbol{v}_2(x), \ldots, \boldsymbol{v}_n(x)) - \boldsymbol{f}(x)|^2), \end{aligned} \tag{6.1}$$

where $S(\cdot)$ is an orientation selection function, and $\boldsymbol{v}_i(x)$'s are the raw FOs estimated without the guidance from tract segmentation. If the selection is determined beforehand, for example, by applying a first run of the proposed FO estimation without using crossing directions (as in the first case) and choosing the closest $\boldsymbol{v}_i$ to the estimated FO, then the proposed optimization can still be applied. If the selection is also iteratively updated, the extension may not be straightforward and the current optimization needs to be modified to solve the minimization problem. Another issue in the orientation selection is the possible discrepancy between the segmentation and the raw FOs $\boldsymbol{v}_i(x)$. For example, a region identified by the segmentation as a crossing region can contain only one raw FO or a region labeled as noncrossing can have multiple raw FOs. In these cases, the selection of $\boldsymbol{v}_i(x)$ can be nontrivial.

The proposed method also potentially provides an algorithm for joint fiber tracking/labeling. As seen in the results, with a proper seeding mask inside a segmented tract, the tracked streamlines can also be viewed as the streamlines with the corresponding tract label. Currently, the seeding mask is chosen empirically and cannot guarantee to track the complete set of streamlines belonging to the tract. A further exploration into the seeding mask and false positive removal may solve the issue and provide simultaneous fiber tracking and labeling.

6.3 Resolution of Interdigitated Tongue Muscles

6.3.1 Main Results

1. The proposed method, Fiber Interdigitation Estimation by Bayesian Reconstruction (FIEBR), distinguishes interdigitated tongue muscles with limited diffusion gradient directions, where conventional multi-tensor models perform poorly.

2. By incorporating prior directional knowledge, FIEBR produces crossing muscle fibers that agree with anatomy and reduces the effect of noise.

3. The FO distributions also suggest that FIEBR produces anatomically desirable fiber organizations.

4. FIEBR was performed on patients with glossectomies, and it respects the anomalies in patients.

5. A case study on three control subjects and three patients demonstrates the differences in FO distributions between subjects, and suggests the potential clinical use of FIEBR.

6.3.2 Future Work

In this work, we assume the Rician noise model and approximate it with a Gaussian distribution. However, the Rician noise model does not hold for GRAPPA reconstruction, where the noise follows a noncentral χ distribution [144]. Although the Gaussian approximation of the noise is a reasonable choice in practice, it is possible to build more accurate models that take the noncentral χ noise distribution into consideration.

Currently the segmentation of the muscles is obtained by registration of a template. This could be replaced by a carefully designed volumetric segmentation algorithm to improve the segmentation accuracy. In the brain, such algorithms have been developed, such as DOTS [15] and TRACULA [19]. There is also an effort that segments the *ex vivo* calf tongue muscles [95]. These methods could be adapted and then applied on the human tongue muscles to provide better regions of interest (ROIs) of muscles.

In the case study, the FOs were compared globally (in the whole tongue). It is possible to make more detailed local analysis that involves specific ROIs, which can provide information that may not be revealed in the global comparison. For example, the FOs near the lesion can be examined to determine if muscle structures are well preserved. Besides the FOs, fiber tracking could also be used for these studies. Fiber properties such as length, curvature, and mean orientations could be used to indicate the influence of the surgery on the muscles.

6.4 Automatic Volumetric Segmentation of the Cerebellar Peduncles

6.4.1 Main Results

1. The proposed method segments the cerebellar peduncles, which comprise the superior cerebellar peduncles (SCPs), the middle cerebellar peduncle (MCP), and the inferior cerebellar peduncles (ICPs), including the decussation of the SCPs (dSCP), which is the crossing region of the SCPs.

2. The segmentation accuracy was evaluated using the Dice coefficient and average surface distances. The range of the Dice coefficients is from 0.720 to 0.850, and the range of the average surface distances is from 0.335 mm to 0.697 mm. The proposed method achieves better segmentation performance than two registration-based methods. For the dSCP, the performance of the proposed method is significantly better than the two comparing methods.

3. In a study on SCA6, anatomical differences were observed compared to the healthy subjects. Compared with the control group, the volumes of the dSCP, the left ICP, and the right ICP decrease significantly in the SCA6 group; the mean diffusivities (MDs) in the left and right noncrossing SCPs, the MCP, and the left and right ICPs increase significantly in the SCA6 group.

6.4.2 Future Work

Currently, the features used in the random forest classifier (RFC) are based on the quantities calculated from the single tensor model. It is also possible to use the features from multi-tensor models which estimate multiple FOs in a voxel. For example, if a two-tensor model is used, such as [26], the 5D Knutsson map can also be calculated for the two FOs respectively. Similarly, the proposed method can also be combined with HARDI and DSI, where multiple FOs can be estimated using constrained spherical deconvolution [142] or q-ball reconstruction with the spherical harmonic basis [145] on HARDI, and local maximum method [143] on DSI. One practical issue may be the order of the multiple FOs. When the contributions of the FOs are close, the order may be influenced by noise, which causes incorrect feature correspondence. Besides the directional information, scalar quantities such as mixture fractions [26, 27] and generalized fractional anisotropy (FA) [23] can also be included to aid classification.

The proposed method segments the structure of the cerebellar peduncles. It is also possible to extend it as a general tract segmentation method. For a general set of tracts, the noncrossing and crossing regions need to be identified manually using the C_l and the Knutsson edge map on training subjects. Features can then be calculated to train the RFC. The quality of the manual delineations and the required number of training data will depend on the variability of the tracts of interest, and the manual delineations could take a large amount of time when the tracts have complex

structures.

We performed a preliminary study that shows the potential application of the proposed method to the study of cerebellar ataxia. However, the measurement of FA and MD is based on the single tensor and could have limitations. For example, the FA in crossing regions may cause misleading interpretation because the values can be influenced by tract integrity and/or crossing fibers. Also, the study currently uses measurements calculated in the whole tract volume, but it can be extended with more detailed analysis of the tracts. For example, Yushkevich et al. [146] use medial representations of tracts and enable statistical analysis in a shape-based coordinate system, where detailed information with respect to spatial location can also be analyzed.

6.5 Overall Perspective

DTI provides a unique tool for noninvasively investigating fiber structures. In this thesis, we explored fiber tracking and tract segmentation methods that produce better representation of fibers and demonstrated their potential scientific and clinical use. These methods can also be applied for scientific studies that have not been discussed in this thesis. We hope that the proposed work can contribute to further advancements in the understanding of structures and diseases, and it can help further development of tools for medical image analysis.

Bibliography

[1] P. J. Basser, J. Mattiello, and D. LeBihan, "MR diffusion tensor spectroscopy and imaging," *Biophysical Journal*, vol. 66, no. 1, pp. 259–267, 1994.

[2] D. Le Bihan, J.-F. Mangin, C. Poupon, C. A. Clark, S. Pappata, N. Molko, and H. Chabriat, "Diffusion tensor imaging: concepts and applications," *Journal of Magnetic Resonance Imaging*, vol. 13, no. 4, pp. 534–546, 2001.

[3] S. Mori, B. J. Crain, V. P. Chacko, and P. Van Zijl, "Three-dimensional tracking of axonal projections in the brain by magnetic resonance imaging," *Annals of Neurology*, vol. 45, no. 2, pp. 265–269, 1999.

[4] P. Basser, S. Pajevic, C. Pierpaoli, J. Duda, and A. Aldroubi, "In vivo fiber tractography using DT-MRI data," *Magnetic Resonance in Medicine*, vol. 44, no. 4, pp. 625–632, 2000.

[5] A. Horn, D. Ostwald, M. Reisert, and F. Blankenburg, "The structural-functional connectome and the default mode network of the human brain,"

NeuroImage, vol. 102, Part 1, no. 0, pp. 142–151, 2014. [Online]. Available: http://www.sciencedirect.com/science/article/pii/S1053811913010057

[6] X. Wang, W. E. L. Grimson, and C. F. Westin, "Tractography segmentation using a hierarchical dirichlet processes mixture model," *NeuroImage*, vol. 54, no. 1, pp. 290–302, 2011. [Online]. Available: http://www.sciencedirect.com/science/article/pii/S1053811910010232

[7] D. Zhu, K. Li, L. Guo, X. Jiang, T. Zhang, D. Zhang, H. Chen, F. Deng, C. Faraco, C. Jin, C.-Y. Wee, Y. Yuan, P. Lv, Y. Yin, X. Hu, L. Duan, X. Hu, J. Han, L. Wang, D. Shen, L. S. Miller, L. Li, and T. Liu, "DICCCOL: Dense individualized and common connectivity-based cortical landmarks," *Cerebral Cortex*, vol. 23, no. 4, pp. 786–800, 2013. [Online]. Available: http://cercor.oxfordjournals.org/content/23/4/786.abstract

[8] B. Audoin, M. Guye, F. Reuter, M.-V. Au Duong, S. Confort-Gouny, I. Malikova, E. Soulier, P. Viout, A. A. Chérif, P. J. Cozzone, J. Pelletier, and J.-P. Ranjeva, "Structure of WM bundles constituting the working memory system in early multiple sclerosis: a quantitative DTI tractography study," *NeuroImage*, vol. 36, no. 4, pp. 1324–1330, 2007.

[9] P. J. Planetta, E. T. Schulze, E. K. Geary, D. M. Corcos, J. G. Goldman, D. M. Little, and D. E. Vaillancourt, "Thalamic projection fiber integrity in de novo

Parkinson disease," *American Journal of Neuroradiology*, vol. 34, no. 1, pp. 74–79, 2013.

[10] G. R. Poudel, J. C. Stout, J. F. Domínguez D, L. Salmon, A. Churchyard, P. Chua, N. Georgiou-Karistianis, and G. F. Egan, "White matter connectivity reflects clinical and cognitive status in Huntington's disease," *Neurobiology of Disease*, vol. 65, no. 0, pp. 180–187, 2014.

[11] A. M. McIntosh, S. M. Maniega, G. K. S. Lymer, J. McKirdy, J. Hall, J. E. Sussmann, M. E. Bastin, J. D. Clayden, E. C. Johnstone, and S. M. Lawrie, "White matter tractography in bipolar disorder and schizophrenia," *Biological Psychiatry*, vol. 64, no. 12, pp. 1088–1092, 2008, schizophrenia: Neural Circuitry and Molecular Mechanisms. [Online]. Available: http://www.sciencedirect.com/science/article/pii/S0006322308009268

[12] K. Oishi, A. Faria, H. Jiang, X. Li, K. Akhter, J. Zhang, J. T. Hsu, M. I. Miller, P. C. van Zijl, M. Albert, C. G. Lyketsos, R. Woods, A. W. Toga, G. B. Pike, P. Rosa-Neto, A. Evans, J. Mazziotta, and S. Mori, "Atlas-based whole brain white matter analysis using large deformation diffeomorphic metric mapping: Application to normal elderly and Alzheimer's disease participants," *NeuroImage*, vol. 46, no. 2, pp. 486–499, 2009. [Online]. Available: http://www.sciencedirect.com/science/article/pii/S1053811909000093

[13] A. N. Voineskos, N. J. Lobaugh, S. Bouix, T. K. Rajji, D. Miranda, J. L.

Kennedy, B. H. Mulsant, B. G. Pollock, and M. E. Shenton, "Diffusion tensor tractography findings in schizophrenia across the adult lifespan," *Brain*, vol. 133, no. 5, pp. 1494–1504, 2010.

[14] L. J. O'Donnell, M. Kubicki, M. E. Shenton, M. H. Dreusicke, W. E. L. Grimson, and C. F. Westin, "A method for clustering white matter fiber tracts," *American Journal of Neuroradiology*, vol. 27, no. 5, pp. 1032–1036, 2006. [Online]. Available: http://www.ajnr.org/content/27/5/1032.abstract

[15] P.-L. Bazin, C. Ye, J. A. Bogovic, N. Shiee, D. S. Reich, J. L. Prince, and D. L. Pham, "Direct segmentation of the major white matter tracts in diffusion tensor images," *NeuroImage*, vol. 58, no. 2, pp. 458–468, 2011.

[16] S. P. Awate, Z. Hui, and J. C. Gee, "A fuzzy, nonparametric segmentation framework for DTI and MRI analysis: With applications to DTI-tract extraction," *IEEE Transactions on Medical Imaging*, vol. 26, no. 11, pp. 1525–1536, 2007.

[17] M.-R. Nazem-Zadeh, E. Davoodi-Bojd, and H. Soltanian-Zadeh, "Atlas-based fiber bundle segmentation using principal diffusion directions and spherical harmonic coefficients," *NeuroImage*, vol. 54, pp. S146–S164, 2011.

[18] C. Ye, J. A. Bogovic, S. H. Ying, and J. L. Prince, "Segmentation of the complete superior cerebellar peduncles using a multi-object geometric deformable

model," in *2013 IEEE 10th International Symposium on Biomedical Imaging (ISBI)*, 2013, pp. 49–52.

[19] A. Yendiki, P. Panneck, P. Srinivasan, A. Stevens, L. Zöllei, J. Augustinack, R. Wang, D. Salat, S. Ehrlich, T. Behrens, S. Jbabdi, R. Gollub, and B. Fischl, "Automated probabilistic reconstruction of white-matter pathways in health and disease using an atlas of the underlying anatomy," *Frontiers in Neuroinformatics*, vol. 5, 2011.

[20] C. Lenglet, M. Rousson, and R. Deriche, "DTI segmentation by statistical surface evolution," *IEEE Transactions on Medical Imaging*, vol. 25, no. 6, pp. 685–700, 2006.

[21] S. Z. Li, *Markov random field modeling in computer vision*. Springer-Verlag New York, Inc., 1995.

[22] S. Osher and N. Paragios, *Geometric level set methods in imaging, vision, and graphics*. Springer, 2003.

[23] D. S. Tuch, "Q-ball imaging," *Magnetic Resonance in Medicine*, vol. 52, no. 6, pp. 1358–1372, 2004.

[24] P. Cheng, V. A. Magnotta, D. Wu, P. Nopoulos, D. J. Moser, J. Paulsen, R. Jorge, and N. C. Andreasen, "Evaluation of the GTRACT diffusion ten-

sor tractography algorithm: a validation and reliability study." *NeuroImage*, vol. 31, no. 3, pp. 1075–1085, 2006.

[25] M. Kleinnijenhuis, M. Barth, D. C. Alexander, A.-M. van Cappellen van Walsum, and D. G. Norris, "Structure tensor informed fiber tractography (STIFT) by combining gradient echo MRI and diffusion weighted imaging," *NeuroImage*, vol. 59, no. 4, pp. 3941–3954, 2012.

[26] T. E. J. Behrens, H. J. Berg, S. Jbabdi, M. F. S. Rushworth, and M. W. Woolrich, "Probabilistic diffusion tractography with multiple fibre orientations: What can we gain?" *NeuroImage*, vol. 34, no. 1, pp. 144–155, 2007.

[27] B. A. Landman, J. A. Bogovic, H. Wan, F. E. Z. ElShahaby, P. L. Bazin, and J. L. Prince, "Resolution of crossing fibers with constrained compressed sensing using diffusion tensor MRI," *NeuroImage*, vol. 59, no. 3, pp. 2175–2186, 2012.

[28] C. Ye, A. Carass, E. Murano, M. Stone, and J. L. Prince, "A Bayesian approach to distinguishing interdigitated muscles in the tongue from limited diffusion weighted imaging," in *Bayesian and grAphical Models for Biomedical Imaging*, ser. Lecture Notes in Computer Science. Springer, 2014, vol. 8677, pp. 13–24.

[29] C. Ye, P.-L. Bazin, S. H. Ying, and J. L. Prince, "A fiber tracking method guided by volumetric tract segmentation," in *2012 IEEE Workshop on Mathematical Methods in Biomedical Image Analysis (MMBIA)*, 2012, pp. 137–142.

[30] E. O. Stejskal and J. E. Tanner, "Spin diffusion measurements: spin echoes in the presence of a time-dependent field gradient," *The Journal of Chemical Physics*, vol. 42, no. 1, p. 288, 1965.

[31] D. K. Jones, "The effect of gradient sampling schemes on measures derived from diffusion tensor MRI: a Monte Carlo study," *Magnetic Resonance in Medicine*, vol. 51, no. 4, pp. 807–815, 2004.

[32] C. G. Koay, L.-C. Chang, J. D. Carew, C. Pierpaoli, and P. J. Basser, "A unifying theoretical and algorithmic framework for least squares methods of estimation in diffusion tensor imaging," *Journal of Magnetic Resonance*, vol. 182, no. 1, pp. 115–125, 2006.

[33] L.-C. Chang, D. K. Jones, and C. Pierpaoli, "Restore: Robust estimation of tensors by outlier rejection," *Magnetic Resonance in Medicine*, vol. 53, no. 5, pp. 1088–1095, 2005. [Online]. Available: http://dx.doi.org/10.1002/mrm.20426

[34] P. J. Basser and C. Pierpaoli, "Microstructural and physiological features of tissues elucidated by quantitative-diffusion-tensor MRI," *Journal of Magnetic Resonance, Series B*, vol. 111, no. 3, pp. 209–219, 1996.

[35] D. Werring, C. Clark, G. Barker, A. Thompson, and D. Miller, "Diffusion tensor imaging of lesions and normal-appearing white matter in multiple sclerosis," *Neurology*, vol. 52, no. 8, pp. 1626–1626, 1999.

[36] M. F. Kraus, T. Susmaras, B. P. Caughlin, C. J. Walker, J. A. Sweeney, and D. M. Little, "White matter integrity and cognition in chronic traumatic brain injury: a diffusion tensor imaging study," *Brain*, vol. 130, no. 10, pp. 2508–2519, 2007.

[37] H. Johansen-Berg and T. E. Behrens, *Diffusion MRI: From quantitative measurement to in-vivo neuroanatomy*. Academic Press, 2009.

[38] P. Helm, M. F. Beg, M. I. Miller, and R. L. Winslow, "Measuring and mapping cardiac fiber and laminar architecture using diffusion tensor mr imaging," *Annals of the New York Academy of Sciences*, vol. 1047, no. 1, pp. 296–307, 2005.

[39] C. Van Donkelaar, L. Kretzers, P. Bovendeerd, L. Lataster, K. Nicolay, J. Janssen, and M. Drost, "Diffusion tensor imaging in biomechanical studies of skeletal muscle function," *Journal of Anatomy*, vol. 194, no. 1, pp. 79–88, 1999.

[40] R. J. Gilbert, "Three-dimensional muscular architecture of the human tongue determined in vivo with diffusion tensor magnetic resonance imaging," *Dysphagia*, vol. 20, no. 1, pp. 1–7, 2005.

[41] S. Roosendaal, J. Geurts, H. Vrenken, H. Hulst, K. Cover, J. Castelijns, P. Pouwels, and F. Barkhof, "Regional DTI differences in multiple sclerosis patients," *NeuroImage*, vol. 44, no. 4, pp. 1397–1403, 2009.

[42] R. A. Menke, J. Scholz, K. L. Miller, S. Deoni, S. Jbabdi, P. M. Matthews, and M. Zarei, "MRI characteristics of the substantia nigra in Parkinson's disease: A combined quantitative T1 and DTI study," *NeuroImage*, vol. 47, no. 2, pp. 435–441, 2009.

[43] N. Barnea-Goraly, H. Kwon, V. Menon, S. Eliez, L. Lotspeich, and A. L. Reiss, "White matter structure in autism: preliminary evidence from diffusion tensor imaging," *Biological Psychiatry*, vol. 55, no. 3, pp. 323–326, 2004.

[44] R. Sprengelmeyer, M. Orth, H.-P. Müller, R. Wolf, G. Grön, M. Depping, J. Kassubek, D. Justo, E. Rees, S. Haider, J. H. Cole, N. Z. Hobbs, R. A. C. Roos, A. Drr, S. J. Tabrizi, S. D. Süssmuth, and G. B. Landwehrmeyer, "The neuroanatomy of subthreshold depressive symptoms in Huntington's disease: a combined diffusion tensor imaging (DTI) and voxel-based morphometry (VBM) study," *Psychological medicine*, vol. 44, no. 09, pp. 1867–1878, 2014.

[45] Y. Zhou, J. H. Dougherty Jr, K. F. Hubner, B. Bai, R. L. Cannon, and R. K. Hutson, "Abnormal connectivity in the posterior cingulate and hippocampus in early Alzheimer's disease and mild cognitive impairment," *Alzheimer's & Dementia*, vol. 4, no. 4, pp. 265–270, 2008.

[46] F. U. Fischer, A. Scheurich, M. Wegrzyn, I. Schermuly, A. L. Bokde, S. Klppel, P. J. Pouwels, S. Teipel, I. Yakushev, and A. Fellgiebel, "Automated tractography of the cingulate bundle in Alzheimer's disease: A multicenter

DTI study," *Journal of Magnetic Resonance Imaging*, vol. 36, no. 1, pp. 84–91, 2012. [Online]. Available: http://dx.doi.org/10.1002/jmri.23621

[47] M. Shenton, H. Hamoda, J. Schneiderman, S. Bouix, O. Pasternak, Y. Rathi, M.-A. Vu, M. Purohit, K. Helmer, I. Koerte, A. Lin, C.-F. Westin, R. Kikinis, M. Kubicki, R. Stern, and R. Zafonte, "A review of magnetic resonance imaging and diffusion tensor imaging findings in mild traumatic brain injury," *Brain Imaging and Behavior*, vol. 6, no. 2, pp. 137–192, 2012.

[48] M. Kubicki, C.-F. Westin, R. W. McCarley, and M. E. Shenton, "The application of DTI to investigate white matter abnormalities in schizophrenia," *Annals of the New York Academy of Sciences*, vol. 1064, no. 1, pp. 134–148, 2005.

[49] T. Bracht, H. Horn, W. Strik, A. Federspiel, N. Razavi, K. Stegmayer, R. Wiest, T. Dierks, T. J. Mller, and S. Walther, "White matter pathway organization of the reward system is related to positive and negative symptoms in schizophrenia," *Schizophrenia Research*, vol. 153, no. 13, pp. 136–142, 2014. [Online]. Available: http://www.sciencedirect.com/science/article/pii/S0920996414000188

[50] A. Zalesky, A. Fornito, M. L. Seal, L. Cocchi, C.-F. Westin, E. T. Bullmore, G. F. Egan, and C. Pantelis, "Disrupted axonal fiber connectivity in schizophrenia," *Biological Psychiatry*, vol. 69, no. 1, pp. 80–89,

2011. [Online]. Available: http://www.sciencedirect.com/science/article/pii/S0006322310008875

[51] S. H. Ying, B. A. Landman, S. Chowdhury, A. H. Sinofsky, A. Gambini, S. Mori, D. S. Zee, and J. L. Prince, "Orthogonal diffusion-weighted MRI measures distinguish region-specific degeneration in cerebellar ataxia subtypes," *Journal of Neurology*, vol. 256, no. 11, pp. 1939–1942, 2009.

[52] B. Wang, Y. Fan, M. Lu, S. Li, Z. Song, X. Peng, R. Zhang, Q. Lin, Y. He, J. Wang, and R. Huang, "Brain anatomical networks in world class gymnasts: A DTI tractography study," *NeuroImage*, vol. 65, pp. 476–487, 2013.

[53] M. Lazar, D. M. Weinstein, J. S. Tsuruda, K. M. Hasan, K. Arfanakis, M. E. Meyerand, B. Badie, H. A. Rowley, V. Haughton, A. Field, and A. L. Alexander, "White matter tractography using diffusion tensor deflection," *Human Brain Mapping*, vol. 18, no. 4, pp. 306–321, 2003.

[54] Y. Lu, A. Aldroubi, J. C. Gore, A. W. Anderson, and Z. Ding, "Improved fiber tractography with Bayesian tensor regularization," *NeuroImage*, vol. 31, no. 3, pp. 1061–1074, 2006.

[55] S. Peled, O. Friman, F. Jolesz, and C. F. Westin, "Geometrically constrained two-tensor model for crossing tracts in DWI," *Magnetic Resonance Imaging*, vol. 24, no. 9, pp. 1263–1270, 2006.

[56] Q. Zhou, O. Michailovich, and Y. Rathi, "Resolving complex fibre architecture by means of sparse spherical deconvolution in the presence of isotropic diffusion," in *SPIE Medical Imaging*. International Society for Optics and Photonics, 2014, pp. 903 425–903 425.

[57] O. Michailovich, Y. Rathi, and S. Dolui, "Spatially regularized compressed sensing for high angular resolution diffusion imaging," *IEEE Transactions on Medical Imaging*, vol. 30, no. 5, pp. 1100–1115, 2011.

[58] A. Ramirez-Manzanares, M. Rivera, B. C. Vemuri, P. Carney, and T. Mareci, "Diffusion basis functions decomposition for estimating white matter intravoxel fiber geometry," *IEEE Transactions on Medical Imaging*, vol. 26, no. 8, pp. 1091–1102, 2007.

[59] J. G. Malcolm, O. Michailovich, S. Bouix, C. F. Westin, M. E. Shenton, and Y. Rathi, "A filtered approach to neural tractography using the Watson directional function," *Medical Image Analysis*, vol. 14, no. 1, pp. 58–69, 2010.

[60] D. S. Tuch, T. G. Reese, M. R. Wiegell, N. Makris, J. W. Belliveau, and V. J. Wedeen, "High angular resolution diffusion imaging reveals intravoxel white matter fiber heterogeneity," *Magnetic Resonance in Medicine*, vol. 48, no. 4, pp. 577–582, 2002. [Online]. Available: http://dx.doi.org/10.1002/mrm.10268

[61] V. J. Wedeen, P. Hagmann, W.-Y. I. Tseng, T. G. Reese, and R. M. Weisskoff, "Mapping complex tissue architecture with diffusion spectrum magnetic

resonance imaging," *Magnetic Resonance in Medicine*, vol. 54, no. 6, pp. 1377–1386, 2005. [Online]. Available: http://dx.doi.org/10.1002/mrm.20642

[62] F. Lin, S. Weng, B. Xie, G. Wu, and H. Lei, "Abnormal frontal cortex white matter connections in bipolar disorder: a DTI tractography study," *Journal of Affective Disorders*, vol. 131, no. 1, pp. 299–306, 2011.

[63] D. S. Reich, S. A. Smith, K. M. Zackowski, E. M. Gordon-Lipkin, C. K. Jones, J. A. Farrell, S. Mori, P. C. van Zijl, and P. A. Calabresi, "Multiparametric magnetic resonance imaging analysis of the corticospinal tract in multiple sclerosis," *NeuroImage*, vol. 38, no. 2, pp. 271–279, 2007.

[64] C. B. Goodlett, P. T. Fletcher, J. H. Gilmore, and G. Gerig, "Group analysis of DTI fiber tract statistics with application to neurodevelopment," *NeuroImage*, vol. 45, no. 1, Supplement 1, pp. S133–S142, 2009, mathematics in Brain Imaging.

[65] S. Niogi, P. Mukherjee, J. Ghajar, C. Johnson, R. Kolster, R. Sarkar, H. Lee, M. Meeker, R. Zimmerman, G. Manley, and B. McCandliss, "Extent of microstructural white matter injury in postconcussive syndrome correlates with impaired cognitive reaction time: A 3T diffusion tensor imaging study of mild traumatic brain injury," *American Journal of Neuroradiology*, vol. 29, no. 5, pp. 967–973, 2008.

[66] M. Buchsbaum, P. Schoenknecht, Y. Torosjan, R. Newmark, K.-W. Chu,

S. Mitelman, A. Brickman, L. Shihabuddin, M. Haznedar, E. Hazlett, S. Ahmed, and C. Tang, "Diffusion tensor imaging of frontal lobe white matter tracts in schizophrenia," *Annals of General Psychiatry*, vol. 5, no. 1, 2006.

[67] M. Maddah, A. U. J. Mewes, S. Haker, W. E. L. Grimson, and S. K. Warfield, "Automated atlas-based clustering of white matter fiber tracts from DTMRI," in *Medical Image Computing and Computer-Assisted Intervention–MICCAI 2005*, 2005, vol. 3749, pp. 188–195.

[68] M. Maddah, W. E. L. Grimson, S. K. Warfield, and W. M. Wells, "A unified framework for clustering and quantitative analysis of white matter fiber tracts," *Medical Image Analysis*, vol. 12, no. 2, pp. 191–202, 2008. [Online]. Available: http://www.sciencedirect.com/science/article/pii/S1361841507000990

[69] S. Zhang, S. Correia, and D. H. Laidlaw, "Identifying white-matter fiber bundles in DTI data using an automated proximity-based fiber-clustering method," *IEEE Transactions on Visualization and Computer Graphics*, vol. 14, no. 5, pp. 1044–1053, 2008.

[70] L. J. O'Donnell and C. F. Westin, "Automatic tractography segmentation using a high-dimensional white matter atlas," *IEEE Transactions on Medical Imaging*, vol. 26, no. 11, pp. 1562–1575, 2007.

[71] R. O. Suarez, O. Commowick, S. P. Prabhu, and S. K. Warfield, "Automated delineation of white matter fiber tracts with a multiple region-of-interest

approach," *NeuroImage*, vol. 59, no. 4, pp. 3690–3700, 2012. [Online]. Available: http://www.sciencedirect.com/science/article/pii/S1053811911013243

[72] I. N. C. Lawes, T. R. Barrick, V. Murugam, N. Spierings, D. R. Evans, M. Song, and C. A. Clark, "Atlas-based segmentation of white matter tracts of the human brain using diffusion tensor tractography and comparison with classical dissection," *NeuroImage*, vol. 39, no. 1, pp. 62–79, 2008.

[73] P. Guevara, C. Poupon, D. Rivire, Y. Cointepas, M. Descoteaux, B. Thirion, and J.-F. Mangin, "Robust clustering of massive tractography datasets," *NeuroImage*, vol. 54, no. 3, pp. 1975–1993, 2011.

[74] H. Li, Z. Xue, L. Guo, T. Liu, J. Hunter, and S. T. Wong, "A hybrid approach to automatic clustering of white matter fibers," *NeuroImage*, vol. 49, no. 2, pp. 1249–1258, 2010.

[75] X. Hao, K. Zygmunt, R. T. Whitaker, and P. T. Fletcher, "Improved segmentation of white matter tracts with adaptive riemannian metrics," *Medical Image Analysis*, vol. 18, no. 1, pp. 161–175, 2014.

[76] Z. Wang and B. C. Vemuri, "DTI segmentation using an information theoretic tensor dissimilarity measure," *IEEE Transactions on Medical Imaging*, vol. 24, no. 10, pp. 1267–1277, 2005.

[77] L. Sivaswamy, A. Kumar, D. Rajan, M. Behen, O. Muzik, D. Chugani, and

H. Chugani, "A diffusion tensor imaging study of the cerebellar pathways in children with autism spectrum disorder," *Journal of Child Neurology*, vol. 25, no. 10, pp. 1223–1231, 2010.

[78] J. Nolte, *The Human Brain: An Introduction to Its Functional Anatomy*. Mosby, 2002.

[79] Y. Murata, H. Kawakami, S. Yamaguchi, M. Nishimura, T. Kohriyama, F. Ishizaki, Z. Matsuyama, Y. Mimori, and S. Nakamura, "Characteristic magnetic resonance imaging findings in spinocerebellar ataxia 6," *Archives of Neurology*, vol. 55, no. 10, p. 1348, 1998.

[80] F. Wang, Z. Sun, X. Du, X. Wang, Z. Cong, H. Zhang, D. Zhang, and N. Hong, "A diffusion tensor imaging study of middle and superior cerebellar peduncle in male patients with schizophrenia," *Neuroscience Letters*, vol. 348, no. 3, pp. 135–138, 2003.

[81] G. Nicoletti, F. Fera, F. Condino, W. Auteri, O. Gallo, P. Pugliese, G. Arabia, L. Morgante, P. Barone, M. Zappia, and A. Quattrone, "MR imaging of middle cerebellar peduncle width: Differentiation of multiple system atrophy from Parkinson disease," *Radiology*, vol. 239, no. 3, pp. 825–830, 2006.

[82] M. Cavallari, N. Moscufo, P. Skudlarski, D. Meier, V. P. Panzer, G. D. Pearlson, W. B. White, L. Wolfson, and C. R. Guttmann, "Mobility impairment is associated with reduced microstructural integrity of the inferior and superior

cerebellar peduncles in elderly with no clinical signs of cerebellar dysfunction," *NeuroImage: Clinical*, vol. 2, no. 0, pp. 332–340, 2013.

[83] C. Clemm von Hohenberg, M. Schocke, M. Wigand, W. Nachbauer, C. Guttmann, M. Kubicki, M. Shenton, S. Boesch, and K. Egger, "Radial diffusivity in the cerebellar peduncles correlates with clinical severity in Friedreich ataxia," *Neurological Sciences*, vol. 34, no. 8, pp. 1459–1462, 2013.

[84] R. Hanaie, I. Mohri, K. Kagitani-Shimono, M. Tachibana, J. Azuma, J. Matsuzaki, Y. Watanabe, N. Fujita, and M. Taniike, "Altered microstructural connectivity of the superior cerebellar peduncle is related to motor dysfunction in children with autistic spectrum disorders," *The Cerebellum*, vol. 12, no. 5, pp. 645–656, 2013.

[85] J. Hüttlova, Z. Kikinis, M. Kerkovsky, S. Bouix, M.-A. Vu, N. Makris, M. Shenton, and T. Kasparek, "Abnormalities in myelination of the superior cerebellar peduncle in patients with schizophrenia and deficits in movement sequencing," *The Cerebellum*, pp. 1–10, 2014.

[86] S. Wang, G. G. Fan, K. Xu, and C. Wang, "Altered microstructural connectivity of the superior and middle cerebellar peduncles are related to motor dysfunction in children with diffuse periventricular leucomalacia born preterm: A DTI tractography study," *European Journal of Radiology*, vol. 83, no. 6, pp. 997–1004, 2014.

[87] A. W. Buijink, M. W. Caan, M. F. Contarino, P. R. Schuurman, P. van den Munckhof, R. M. de Bie, S. D. Olabarriaga, J. D. Speelman, and A.-F. van Rootselaar, "Structural changes in cerebellar outflow tracts after thalamotomy in essential tremor," *Parkinsonism & Related Disorders*, vol. 20, no. 5, pp. 554–557, 2014.

[88] J. G. Ojemann, S. C. Partridge, A. V. Poliakov, T. N. Niazi, D. W. Shaw, G. E. Ishak, A. Lee, S. R. Browd, J. Geyer, and R. G. Ellenbogen, "Diffusion tensor imaging of the superior cerebellar peduncle identifies patients with posterior fossa syndrome," *Child's Nervous System*, vol. 29, no. 11, pp. 2071–2077, 2013.

[89] P. Perrini, G. Tiezzi, M. Castagna, and R. Vannozzi, "Three-dimensional microsurgical anatomy of cerebellar peduncles," *Neurosurgical Review*, pp. 1–11, 2012.

[90] S. Mori, S. Wakana, P. C. Van Zijl, and L. Nagae-Poetscher, *MRI atlas of human white matter*. Am Soc Neuroradiology, 2005.

[91] R. J. Gilbert, "Three-dimensional muscular architecture of the human tongue determined in vivo with diffusion tensor magnetic resonance imaging," *Dysphagia*, vol. 20, no. 1, pp. 1–7, 2005.

[92] H. Shinagawa, E. Murano, J. Zhuo, B. Landman, R. Gullapalli, J. Prince, and M. Stone, "Effect of oral appliances on genioglossus muscle tonicity seen with diffusion tensor imaging: A pilot study," *Oral Surgery, Oral Medicine, Oral*

Pathology, Oral Radiology, and Endodontology, vol. 107, no. 3, pp. e57–e63, 2009.

[93] T. Gaige, T. Benner, R. Wang, V. Wedeen, and R. Gilbert, "Three dimensional myoarchitecture of the human tongue determined in vivo by diffusion tensor imaging with tractography," *Journal of Magnetic Resonance Imaging*, vol. 26, no. 3, pp. 654–661, 2007.

[94] S. M. Felton, T. A. Gaige, T. Benner, R. Wang, T. G. Reese, V. J. Wedeen, and R. J. Gilbert, "Associating the mesoscale fiber organization of the tongue with local strain rate during swallowing," *Journal of Biomechanics*, vol. 41, no. 8, pp. 1782–1789, 2008.

[95] S. Kim, A. Barnett, C. Pierpaoli, and G. Chi-Fishman, "Three-dimensional mapping of lingual myoarchitecture by diffusion tensor MRI," *NMR in Biomedicine*, vol. 21, no. 5, pp. 479–488, 2008.

[96] H. Takemoto, "Morphological analyses of the human tongue musculature for three-dimensional modeling," *Journal of Speech, Language, and Hearing Research*, vol. 44, no. 1, pp. 95–107, 2001.

[97] H. Gray, *Anatomy of the human body.* Lea & Febiger, 1918.

[98] R. Drake, A. W. Vogl, and A. W. Mitchell, *Gray's anatomy for students.* Elsevier Health Sciences, 2009.

BIBLIOGRAPHY

[99] R. Aranda, M. Rivera, and A. Ramirez-Manzanares, "A flocking based method for brain tractography," *Medical Image Analysis*, vol. 18, no. 3, pp. 515–530, 2014.

[100] R. Courant and D. Hilbert, *Methods of Mathematical Physics*. Wiley-Interscience, 1966, vol. 1.

[101] B. K. P. Horn and B. G. Schunck, "Determining optical flow," *Artificial Intelligence*, vol. 17, no. 1, pp. 185–203, 1981.

[102] C. Thomas, K. Humphreys, K.-J. Jung, N. Minshew, and M. Behrmann, "The anatomy of the callosal and visual-association pathways in high-functioning autism: A DTI tractography study," *Cortex*, vol. 47, no. 7, pp. 863–873, 2011.

[103] E. X. Wu, Y. Wu, J. M. Nicholls, J. Wang, S. Liao, S. Zhu, C.-P. Lau, and H.-F. Tse, "MR diffusion tensor imaging study of postinfarct myocardium structural remodeling in a porcine model," *Magnetic Resonance in Medicine*, vol. 58, no. 4, pp. 687–695, 2007.

[104] P. Fillard, M. Descoteaux, A. Goh, S. Gouttard, B. Jeurissen, J. Malcolm, A. Ramirez-Manzanares, M. Reisert, K. Sakaie, F. Tensaouti, T. Yo, J.-F. Mangin, and C. Poupon, "Quantitative evaluation of 10 tractography algorithms on a realistic diffusion MR phantom," *NeuroImage*, vol. 56, no. 1, pp. 220–234, 2011.

[105] C. Poupon, B. Rieul, I. Kezele, M. Perrin, F. Poupon, and J.-F. Mangin, "New diffusion phantoms dedicated to the study and validation of high-angular-resolution diffusion imaging (HARDI) models," *Magnetic Resonance in Medicine*, vol. 60, no. 6, pp. 1276–1283, 2008.

[106] M. Jenkinson, C. F. Beckmann, T. E. J. Behrens, M. W. Woolrich, and S. M. Smith, "FSL," *NeuroImage*, vol. 62, no. 2, pp. 782–790, 2012.

[107] B. C. Lucas, J. A. Bogovic, A. Carass, P.-L. Bazin, J. L. Prince, D. L. Pham, and B. A. Landman, "The Java image science toolkit (JIST) for rapid prototyping and publishing of neuroimaging software," *Neuroinformatics*, vol. 8, no. 1, pp. 5–17, 2010.

[108] B. A. Landman, J. A. D. Farrell, N.-L. Patel, S. Mori, and J. L. Prince, "DTI fiber tracking: the importance of adjusting DTI gradient tables for motion correction. CATNAP - a tool to simplify and accelerate DTI analysis," in *Proc. Org Human Brain Mapping 13th Annual Meeting*, 2007.

[109] A. Qazi, A. Radmanesh, L. O'Donnell, G. Kindlmann, S. Peled, S. Whalen, C. Westin, and A. Golby, "Resolving crossings in the corticospinal tract by two-tensor streamline tractography: Method and clinical assessment using fMRI," *NeuroImage*, vol. 47, pp. 98–106, 2009.

[110] D. K. Jones, T. R. Knösche, and R. Turner, "White matter integrity, fiber

count, and other fallacies: the do's and don'ts of diffusion MRI," *NeuroImage*, vol. 73, pp. 239–254, 2013.

[111] R. S. Desikan, F. Ségonne, B. Fischl, B. T. Quinn, B. C. Dickerson, D. Blacker, R. L. Buckner, A. M. Dale, R. P. Maguire, B. T. Hyman, M. S. Albert, and R. J. Killiany, "An automated labeling system for subdividing the human cerebral cortex on MRI scans into gyral based regions of interest," *NeuroImage*, vol. 31, no. 3, pp. 968–980, 2006.

[112] B. Fischl, "FreeSurfer," *NeuroImage*, vol. 62, no. 2, pp. 774–781, 2012.

[113] E. Z. Murano, H. Shinagawa, J. Zhuo, R. P. Gullapalli, R. A. Ord, J. L. Prince, and M. Stone, "Application of diffusion tensor imaging after glossectomy," *Otolaryngology–Head and Neck Surgery*, vol. 143, no. 2, pp. 304–306, 2010.

[114] H. Shinagawa, E. Z. Murano, J. Zhuo, B. Landman, R. P. Gullapalli, J. L. Prince, and M. Stone, "Tongue muscle fiber tracking during rest and tongue protrusion with oral appliances: A preliminary study with diffusion tensor imaging," *Acoustical Science and Technology*, vol. 29, no. 4, pp. 291–294, 2008.

[115] D. Weinstein, G. Kindlmann, and E. Lundberg, "Tensorlines: Advection-diffusion based propagation through diffusion tensor fields," in *Proceedings of the conference on Visualization'99: celebrating ten years*. IEEE Computer Society Press, 1999, pp. 249–253.

[116] M. R. Wiegell, H. B. Larsson, and V. J. Wedeen, "Fiber crossing in human brain depicted with diffusion tensor MR imaging," *Radiology*, vol. 217, no. 3, pp. 897–903, 2000.

[117] S. Merlet, E. Caruyer, and R. Deriche, "Parametric dictionary learning for modeling EAP and ODF in diffusion MRI," in *Medical Image Computing and Computer-Assisted Intervention–MICCAI 2012*. Springer, 2012, pp. 10–17.

[118] A. Gramfort, C. Poupon, and M. Descoteaux, "Sparse DSI: Learning DSI structure for denoising and fast imaging," in *Medical Image Computing and Computer-Assisted Intervention–MICCAI 2012*. Springer, 2012, pp. 288–296.

[119] B. Bilgic, K. Setsompop, J. Cohen-Adad, A. Yendiki, L. L. Wald, and E. Adalsteinsson, "Accelerated diffusion spectrum imaging with compressed sensing using adaptive dictionaries," *Magnetic Resonance in Medicine*, vol. 68, no. 6, pp. 1747–1754, 2012.

[120] E. J. Candes, M. B. Wakin, and S. P. Boyd, "Enhancing sparsity by reweighted ℓ_1 minimization," *Journal of Fourier Analysis and Applications*, vol. 14, no. 5-6, pp. 877–905, 2008.

[121] A. Daducci, D. Van De Ville, J.-P. Thiran, and Y. Wiaux, "Sparse regularization for fiber ODF reconstruction: From the suboptimality of ℓ_2 and ℓ_1 priors to ℓ_0," *Medical Image Analysis*, vol. 18, no. 6, pp. 820–833, 2014.

[122] H. Gudbjartsson and S. Patz, "The Rician distribution of noisy MRI data," *Magnetic Resonance in Medicine*, vol. 34, no. 6, pp. 910–914, 1995.

[123] S.-J. Kim, K. Koh, M. Lustig, and S. Boyd, "An efficient method for compressed sensing," in *IEEE International Conference on Image Processing*, vol. 3, 2007, pp. 117–120.

[124] B. B. Avants, C. L. Epstein, M. Grossman, and J. C. Gee, "Symmetric diffeomorphic image registration with cross-correlation: evaluating automated labeling of elderly and neurodegenerative brain," *Medical Image Analysis*, vol. 12, no. 1, pp. 26–41, 2008.

[125] J. Sijbers, A. den Dekker, J. V. Audekerke, M. Verhoye, and D. V. Dyck, "Estimation of the noise in magnitude MR images," *Magnetic Resonance Imaging*, vol. 16, no. 1, pp. 87–90, 1998. [Online]. Available: http://www.sciencedirect.com/science/article/pii/S0730725X97001999

[126] R. Wang, T. Benner, A. G. Sorensen, and V. J. Wedeen, "Diffusion toolkit: a software package for diffusion imaging data processing and tractography," in *Proc Intl Soc Mag Reson Med*, vol. 15, 2007, p. 3720.

[127] C. Ye, P.-L. Bazin, J. A. Bogovic, S. H. Ying, and J. L. Prince, "Labeling of the cerebellar peduncles using a supervised Gaussian classifier with volumetric tract segmentation," in *Proceedings of SPIE Medical Imaging*, vol. 8314, 2012, p. 143.

[128] C. F. Westin, S. Peled, H. Gudbjartsson, R. Kikinis, and F. A. Jolesz, "Geometrical diffusion measures for MRI from tensor basis analysis," in *Proceedings of ISMRM*, vol. 97, 1997, p. 1742.

[129] L. Breiman, "Random forests," *Machine Learning*, vol. 45, no. 1, pp. 5–32, 2001.

[130] J. A. Bogovic, J. L. Prince, and P.-L. Bazin, "A multiple object geometric deformable model for image segmentation," *Computer Vision and Image Understanding*, vol. 117, no. 2, pp. 145–157, 2013. [Online]. Available: http://www.sciencedirect.com/science/article/pii/S1077314212001440?v=s5

[131] R. J. Sinke, E. F. Ippel, C. M. Diepstraten, F. A. Beemer, J. H. Wokke, B. J. van Hilten, N. V. Knoers, H. K. P. van Amstel, and H. Kremer, "Clinical and molecular correlations in spinocerebellar ataxia type 6: a study of 24 Dutch families," *Archives of Neurology*, vol. 58, no. 11, p. 1839, 2001.

[132] H. Knutsson, "Producing a continuous and distance preserving 5-D vector representation of 3-D orientation," in *IEEE Computer Society Workshop on Computer Architecture for Pattern Analysis and Image Database Management*, 1985, pp. 175–182.

[133] X. Fan, M. Thompson, J. A. Bogovic, P.-L. Bazin, and J. L. Prince, "A novel contrast for DTI visualization for thalamus delineation," in *Proceedings of SPIE Medical Imaging*, vol. 7625, 2010.

[134] V. Caselles, R. Kimmel, and G. Sapiro, "Geodesic active contours," *International Journal of Computer Vision*, vol. 22, no. 1, pp. 61–79, 1997.

[135] C. Xu, A. Yezzi Jr, and J. L. Prince, "On the relationship between parametric and geometric active contours," in *IEEE Conference Record of the Thirty-Fourth Asilomar Conference on Signals, Systems and Computers, 2000*, vol. 1, 2000, pp. 483–489.

[136] L. R. Dice, "Measures of the amount of ecologic association between species," *Ecology*, vol. 26, no. 3, pp. 297–302, 1945.

[137] A. J. Asman and B. A. Landman, "Formulating spatially varying performance in the statistical fusion framework," *IEEE Transactions on Medical Imaging*, vol. 31, no. 6, pp. 1326–1336, 2012.

[138] S. K. Warfield, K. H. Zou, and W. M. Wells, "Simultaneous truth and performance level estimation (STAPLE): an algorithm for the validation of image segmentation," *IEEE Transactions on Medical Imaging*, vol. 23, no. 7, pp. 903–921, 2004.

[139] H. Zhang, B. B. Avants, P. A. Yushkevich, J. H. Woo, S. Wang, L. F. McCluskey, L. B. Elman, E. R. Melhem, and J. C. Gee, "High-dimensional spatial normalization of diffusion tensor images improves the detection of white matter differences: an example study using amyotrophic lateral sclerosis," *IEEE Transactions on Medical Imaging*, vol. 26, no. 11, pp. 1585–1597, 2007.

[140] K. Oishi, S. Mori, P. K. Donohue, T. Ernst, L. Anderson, S. Buchthal, A. Faria, H. Jiang, X. Li, M. I. Miller, P. C. van Zijl, and L. Chang, "Multi-contrast human neonatal brain atlas: application to normal neonate development analysis," *NeuroImage*, vol. 56, no. 1, pp. 8–20, 2011.

[141] K. J. Friston, A. P. Holmes, K. J. Worsley, J.-P. Poline, C. D. Frith, and R. S. Frackowiak, "Statistical parametric maps in functional imaging: a general linear approach," *Human Brain Mapping*, vol. 2, no. 4, pp. 189–210, 1994.

[142] J.-D. Tournier, F. Calamante, and A. Connelly, "Robust determination of the fibre orientation distribution in diffusion MRI: Non-negativity constrained super-resolved spherical deconvolution," *NeuroImage*, vol. 35, no. 4, pp. 1459–1472, 2007.

[143] P. Hagmann, M. Kurant, X. Gigandet, P. Thiran, V. J. Wedeen, R. Meuli, and J.-P. Thiran, "Mapping human whole-brain structural networks with diffusion MRI," *PloS one*, vol. 2, no. 7, p. e597, 2007.

[144] O. Dietrich, J. G. Raya, S. B. Reeder, M. Ingrisch, M. F. Reiser, and S. O. Schoenberg, "Influence of multichannel combination, parallel imaging and other reconstruction techniques on MRI noise characteristics," *Magnetic Resonance Imaging*, vol. 26, no. 6, pp. 754–762, 2008.

[145] C. P. Hess, P. Mukherjee, E. T. Han, D. Xu, and D. B. Vigneron, "Q-ball reconstruction of multimodal fiber orientations using the spherical harmonic

basis," *Magnetic Resonance in Medicine*, vol. 56, no. 1, pp. 104–117, 2006. [Online]. Available: http://dx.doi.org/10.1002/mrm.20931

[146] P. A. Yushkevich, H. Zhang, T. J. Simon, and J. C. Gee, "Structure-specific statistical mapping of white matter tracts," *NeuroImage*, vol. 41, no. 2, pp. 448–461, 2008.

Vita

Chuyang Ye was born on March 24th, 1985 in Harbin, China. He received the B.S. degree in Electrical Engineering from Peking University in 2009. Starting from 2009, he was a graduate student at Johns Hopkins University and he joined the Image Analysis and Communications Laboratory (IACL) supervised by Dr. Jerry L. Prince. In 2011 and 2014, he completed M.S.E. and Ph.D. degrees in the department of Electrical and Computer Engineering, respectively. He also did his internship at GE Global Research in Niskayuna in 2013, where he received a GE Early Identification Award. His research interest is mainly fiber tracking and tract segmentation using diffusion magnetic resonance imaging.